Resorption rate tunable bioceramic: Si,Zn-modified tricalcium phosphate

by

Xiang Wei

A dissertation submitted to the graduate faculty

in partial fulfillment of the requirements for the degree of

DOCTOR OF PHILOSOPHY

Major: Materials Science and Engineering

Program of Study Committee:
Mufit Akinc, Major Professor
Matthew Kramer
Thomas McGee
Surya K. Mallapragada
Michael Conzemius

Iowa State University

Ames, Iowa

2006

Graduate College
Iowa State University

This is to certify that the doctoral dissertation of

Xiang Wei

has met the dissertation requirements of Iowa State University

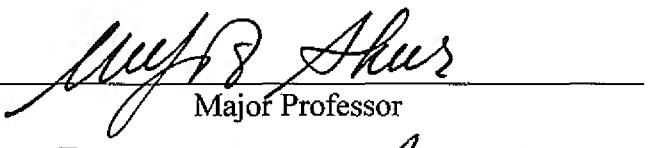

Major Professor

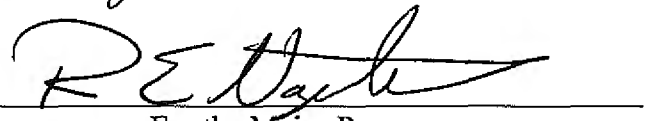

For the Major Program

TABLE OF CONTENTS

CHAPTER 1: GENERAL INTRODUCTION

This chapter consists of three sections. The first section is the organization of this dissertation. The second section gives an overview of the bone structure and formation, and the role of trace element on the biomineralization process. The third section introduces ceramic materials as synthetic bone substitutes focusing on the resorbable calcium phosphate bioceramics and their crystal structure.

I. Dissertation Organization

This dissertation is organized in an alternate format. Several manuscripts which have already been published or are to be submitted for publication have been included as separate chapters. Chapter 1 is a general introduction which describes the dissertation organization and introduces the human bone and ceramic materials as bone substitute. Chapter 2 is the background and literature review on dissolution behavior of calcium phosphate, and discussion of motivation for this research. Chapter 3 is a manuscript entitled "Si,Zn-modified tricalcium phosphate: a phase composition and crystal structure study", which was published in *Key Engineering Materials* [1]. Chapter 4 gives more crystal structure details by neutron powder diffraction, which identifies the position for Si and Zn substitution and explains the stabilization mechanism of the structure. A manuscript entitled "Crystal structure analysis of Si, Zn-modified Tricalcium phosphate by Neutron Powder Diffraction" will be submitted to *Biomaterials* [2].

Chapter 5 is a manuscript, entitled "Dissolution behavior and cytotoxicity test of Si, Zn-modified tricalcium phosphate", which is to be submitted to *Biomaterials* [3]. This paper discusses the additives' effect on the dissolution behavior of TCP, and cytotoxicity test result is also included. Chapter 6 is the study of hydrolysis process of α-tricalcium phosphate in the simulated body fluid, and the phase development during drying process is discussed. A manuscript entitled "Hydrolysis of α-tricalcium phosphate in simulated body fluid and phase transformation during drying process" is to be submitted to *Biomaterials* [4]. Ozan Ugurlu is included as co-authors in these two papers due to his TEM contributions.

Appendix A is the general introduction of the materials synthesis, crystal structure and preliminary dissolution result. A manuscript entitled "Resorption rate tunable bioceramic: Si&Zn-modified tricalcium phosphate" was published in Ceramic Engineering and Science Proceedings (the 29th International Conference on Advanced Ceramics and Composites - Advances in Bioceramics and Biocomposites) [5].

Dr. Mufit Akinc as major professor has been included as co-author on all of the manuscripts included in this dissertation.

II. Bone

2. Properties and structure

Bone is highly specialized tissue and makes up the skeletal system along with cartilage. The two basic functions of bone are: (1) to provide structural support for the body and sites for muscle attachment, and (2) to serve as a reservoir for ions, particularly calcium and phosphate and other trace elements such as magnesium and iron, which are employed in various metabolic reactions in the body.

Bone can be classified according to its anatomic function (weight bearing and protective), shape (long, short, flat), mechanism of formation and/or micro architectural structure (cortical (compact), trabecular (spongy)) [6,7]. Similar to most other living tissues, bone is composed of various types of cells with a distinct extracellular matrix. The characteristic cells in bone are osteoblasts, osteocytes, osteoclasts and bone lining cells [7], which play the important role in the bone resorption and formation. Osteoblasts, which are responsible for bone matrix synthesis, appear on the surfaces of bone undergoing growth and development. They have the characteristic microscopic features of cells, which are actively involved in the synthesis of proteins and the organic component of bone (collagen) as well as several bone-associated noncollegenous proteins in vitro. Osteocytes (presumably derived from osteoblasts) are found buried deep within matrix of mineralized bone, connected to one another or to the osteoblasts and are responsible for nutrition of bone. Osteoclasts are found where the bone is being resorbed and they carry out resorption processes. The last type of cell, bone lining cells, are flat, elongated and line the bone surface and can be considered as

inactive osteoblasts. Bone-lining cells are thought to regulate the movement of calcium and phosphate into and out of the bone [8].

The extracellular matrix of bone, in order of decreasing proportion, consists of mineral, collagen, water, noncollagenous proteins and other organic moieties. Although the proportions vary from one part of the skeleton to another, on a dry weight basis, bone contains 60-70% inorganic and 30-40% organic materials and are in dynamic equilibrium with the body fluid [6].

The mineral of bone is a calcium-deficient, carbonate-containing, poorly-crystalline analogue of the naturally occurring mineral hydroxyapatite ($Ca_{10}(PO_4)_6(OH)_2$ or HAp). Bone apatite is distinct from the geological apatites. It has smaller size with tubular to needle-like morphology measuring 20-80 nm in length and 2-5 nm in diameter [9]. The small crystalline size of bone mineral is coupled with its high surface area (~180 m^2/g) [6]. Bone apatite is also less perfect in atomic arrangement and stoichiometry, resulting in a more reactive and soluble phase compared to the stoichiometric mineral hydroxyapatite. The composition of the bone mineral is heterogeneous with a Ca/P=1.54-1.73 [10,11] and contains surface and structural impurities/substitutions. A large number of research work refers to bone apatite as carbonate-apatite, given carbonate is the most prevalent bone mineral constituent not found in hydroxyapatite. Because of its small crystalline size and correspondingly large surface area, a high proportion of bone mineral particles is available for exchange and reaction with ions in the body fluids. Ions with the similar size and charge readily substitute for Ca^{2+}, PO_4^{3-} and OH^- on the surface and within the growing crystal. In general, incorporation of such ions makes mineral crystals less perfect and more soluble, while some of these ions including Na^+, Cl^- and F^- are reported to stabilize HAp structure and decrease its solubility [12]. Other ions capable of incorporating into the bone mineral are K^+, Mg^{2+}, $CO_3^{2-}, HCO_3^-, HPO_4^{2-}$.

The organic portion of bone consists of collagen, organic cement and cells. As much as 90 to 95 percent of the total organic weight is in the form of collagen fibers. Collagen is a gelatin-like protein, being the chief constituent of organic fibrils of bones, but also of skin and connective tissues. It is characterized by high praline and glycine and low aromatic

amino acid content [13]. The collagen fibrils in bone tissue are surrounded by an organic substance often referred to as cement. This organic cement, along with the bone mineral fills inter-fibrillar spaces. Although the chemical composition of the cement is not definitely known, its nature suggests it is a protein-polysaccharide complex.

3. Bone formation

In general, bone formation and/or mineralization of hard tissues takes place in four distinct stages. The cellular activities of osteoblasts, osteocytes and osteoclasts are essential to the process [9].

The first step in bone mineralization is the production of extracellular organic matrix known as osteoid (mostly collagen) simultaneously by osteoblasts and chondrocytes, which provide an environment favorable for mineralization. The collagenous precursors are typically synthesized and laid down by osteoblasts in concentric layers. Once the organic framework is initially formed, the earliest detectable event is an increase in extracellular calcium and phosphate concentrations associated partially with the loss of these ions from the chondrocytes or osteoblast cells [14]. In addition, proteins as well as activities of certain enzymes associated with the mineralization process increase, preparing the matrix for calcification [15-17].

The formation of initial mineral crystals (nucleation) is the second stage. The transient nature of the first phase makes it very difficult to detect, and verify its mineralogical identity. Some in vitro studies suggested that several calcium-phosphate minerals besides HAp might be the first nucleated mineral during the bone mineralization [18,19]. These studies propose that HAp does not precipitate directly from serum, but a less basic calcium phosphate salt is initially formed, such as brushite ($CaHPO_4 \cdot 2H_2O$) and octacalcium phosphate [20-22], which subsequently hydrolyzes to HAp. The experimental support for a precursor to HAp comes from the above studies on the solubility of calcium-phosphate salts in aqueous solutions. Other investigators noted that amorphous calcium phosphate (ACP) may be the intermediate to HAp [23]. The earliest evidence for the presence of an amorphous, or noncrystalline mineral-phase in bone came from electron-microscopy studies [24]. The subsequent X-ray diffraction studies suggested that this amorphous phase is a major

component of bone mineral [25,26]. Fleisch's result showed that the non-reversible transformation of ACP to HAp could occur in a media at physiological pH values [27].

Bone cells are assumed to play a direct role in formation of the first bone mineral because they generally surround and cover the areas being mineralized. In addition, both the deposition of the calcium-phosphate minerals as well as the initial formation of HAp occurs due to the elevation of local calcium and phosphate concentration coordinated by the cells. Similarly, the formation of specific molecules that can serve as epitaxial nucleators, and the enzymatic removal or modification of macromolecules that inhibit mineral formation are regulated by the cells [28]. Various theories of mineral formation differ as to whether the nucleation can be considered homogenous or heterogeneous. The theories also differ as to how and to what extent the organic tissue is involved in nucleation of bone mineral. In the past, collagen was thought to be a promoter of HAp deposition in bone. Glimcher et al., has demonstrated that only native collagen, showing a periodic arrangement, will calcify in vitro and suggested that initial precipitation is associated with the periodic sites and the gaps created due to the specific organization of collagen macromolecules [29]. Robinson and Watson suggested that amino acids arranged on the surface of collagen molecules to mimic the apatite structure, providing a site for the heterogeneous bone crystal nucleation [24]. Collagen is now considered a passive template for the oriented deposition of the mineral. Platelet-shaped nano-crystals of apatite are incorporated in a parallel way between collagen molecules, with the crystallographic *c* axis parallel to the fiber axis (Figure 1).

Although there is some uncertainty about the chemical and crystallographic nature of the first mineral formed, the mineral deposited over this mineral is hydroxyapatite [7]. This third step, the growth of bone apatite crystals, is biologically regulated, as evidenced by regular orientation and size of bone mineral crystals. It should be noted that blood plasma is considered supersaturated in calcium and phosphate ions with respect to the apatite growth [30], but apparently undersaturated with respect to its nucleation [27].

The initially deposited mineralized matrix does not persist, but rather, in the fourth phase of bone formation, it is resorbed and reformed. Hence, the cycle starts again to meet the mechanical function; bone undergoes dynamic remodeling by a coupled process of bone resorption by osteoclasts and reformation by osteoblasts. Hormones and vitamins together

with the local factors have been implicated in initiating resorption and regulating the remodeling process [31].

4. Role of Trace Elements in Bone

Bone mineral contains 36.6% calcium and 17.1% phosphorus, with various and significant amounts of carbonate, sodium, magnesium, potassium, chloride, fluoride, citrate ions and many other trace elements. The role of these elements in bone maintenance and metabolism and the effect of dietary restrictions has been extensively investigated [32-39]. Table 1 gives the composition of the human bone [40].

Magnesium (Mg) easily replaces calcium in the lattice due to the similar ionic radius (r(CN=6) = 0.65 for Mg^{2+}; r(CN=6) = 0.99 for Ca^{2+} [41]). It is always associated with the mineralization of calcified tissues, mainly in bones and teeth[32]. As reported by Althoff and Bigi [33,34], Mg influences mineral metabolism through activation of alkaline phosphatase and the crystallization process of mineral substances as well as the pattern of mineral formation. It inhibits HAp formation, but prefers to form poorly crystalline or amorphous phase. Although the relative content of zinc (Zn, r(CN=6) = 0.74) is much smaller than that of magnesium, it has been found in all human tissues and the concentration of Zn in bone is higher than in most other tissues [42]. The important role of zinc in many biological functions is well known, such as enzyme activity, nucleic acid metabolism, protein synthesis, maintenance of membrane structure and function, as well as hormonal activity [38,43,44]. Zn was reported to be essential in bone metabolism as cofactors for specific enzymes [45]. In addition, a possible zinc involvement has been suggested in the modulation of the morphology and crystallinity of biological apatite crystals under in vivo conditions [39]. In clinical studies, Walsh et al. have demonstrated the efficacy of Ca, Cu, Mn and Zn supplementation on spinal bone mineral density in postmenopausal women [45]. These trace elements were proposed to promote the formation of strong bones and connective tissue [46]. Each of these studies demonstrated the necessity of trace elements for optimal bone matrix development and bone density sustenance.

In addition to these essential trace elements, vanadium (V), silicon (Si) and boron (B) may emerge as being important in bone health. Silicon is known to be essential for the

growth and development of vertebrates, being involved in cell wall formation, cross-linking in connective tissues, nucleic acid synthesis, photosynthesis, and other biological processes, particularly with regard to aging [35,36]. It has also been found to perform a vital role in skeletal development. Being a constituent of collagen [37], silicon deficiency has been found to retard bone development in chicks [47]. Dietary silicon has been found to increase the rate of bone calcification, and nodular ill-formed bone results from silicon deficiency [35,36]. An increase in dietary silicon has been directly linked to an increase in bone mineralization; particularly when associated with a calcium-deficient diet.

III. Ceramics as synthetic bone substitute

An ideal bone substitute should mimic the tissue which it replaces in size, shape, consistency and function. It should not induce an infection and/or a healing response. As it degrades, it must not alter the function of the adjacent tissues. If it does not degrade, it must be tolerated by the body permanently. From the orthopedic point of view, mechanical integrity, time controlled degradation and simultaneous replacement by newly formed bone define the function of ideal bone substitute material. Within the scope of these constraints, there is a continuing search for an ideal material for bone repair combining the total biological function with adequate material properties.

1. Classification

Ceramics began to be utilized for the repair, reconstruction, and replacement of diseased or damaged parts of the body as early as nineteen century. According to the bioceramic-tissue interface, they are classified as inert, microporous and macroporous, bioactive and resorbable ceramics [48].

For inert implants, the interface is not chemically or biologically bonded. They develop a non-adherent fibrous capsule which isolates the implant to protect the surrounding tissues [49]. The thicker the capsule is, the faster the implant loosens which results in clinical failure. Stress shielding is also a problem with these types of implants and will occur if the implant is stronger than the surrounding bone tissue. The typical examples of inert implant

are high-density alumina (Al_2O_3) and zirconia (ZrO_2), which are used as bone screws, dental implants, and bone substitutes for jaw bone and middle ear reconstruction [50].

For microporous (pore size ~1 μm) and macroporous (pore size >100 μm) implantable materials, the increased interfacial area between the implant and the tissues results in an increased resistance to movement of the device in the tissue [51]. However, the limitation of porous ceramics is that the requirement of the pore size which should be greater than 100 μm to maintain a blood supply to the ingrown tissues. The tissue and blood supply could be damaged by micromovement at the interface of a porous implant and tissue, leading to inflammation and the interfacial instability. The increased surface area can be also detrimental as it increases the dissolution of the implants, especially the rates of corrosion and ion leaching for metal materials. The best and most common examples are porous hydroxyapatite and hydroxyapatite-coated porous metals.

Bioactive material is one that "elicit a specific biological response at the interface of the materials which results in the formation of a bond between the tissue and the materials" [51]. The bioactive materials available commercially for clinical use are 45S5 bioactive glass, A/W bioactive glassceramic, dense synthetic HA, or bioactive composites, such as a polyethylene–HA mixture. In the case of bioactive glasses or glass-ceramics, Si-OH bonds induce a calcium phosphate layer forming on top of the SiO_2-rich layer [48,51,52], leading to the formation of an interfacial bonding zone between tissue and the implanted bioactive glass in vivo. However, the time dependence of bonding, the strength of the bond, the mechanism of bonding, and the thickness of the bonding zone differ for various materials.

Resorbable materials are designed to degrade gradually over a period of time and be replaced by the natural host tissue, which are based on the same principles of natural tissue repair. These materials degrade because they are soluble in the fluid environment and occur in vivo in three ways [48]: (1) physical disintegration due to the inherent weakness for chemical attack at the grain boundaries, (2) chemical dissolution due to the solubility of the material in the surrounding fluid and (3) biological factors, i.e. stimulating osteogenic activity and being resorbed by osteoclasts. The advantages of using resorbable bioceramics are a ready ions supply, the elimination of a second surgical procedure, and the elimination any long-term function or biocompatibility problems due to the replacement of normal and

functional bone. However, there are some complications in the development of resorbable bioceramics also: (1) Maintenance of strength and stability of the interface during the degradation period and replacement by the natural host tissue; (2) Matching resorption rates to the repair rates of body tissues, which themselves vary enormously, depending upon type of tissue and its age and health [48]. The biodegradation ability of the material depends on many factors, which are listed in Table 2[49]. Successful examples of resorbable bone replacement are particulate calcium phosphate ceramic materials, such as tricalcium phosphate (TCP), for hard tissue replacements when only low mechanical strength is required, such as in some repairs of the jaw or head [53,54].

2. Resorbable calcium phosphates

In nature and biological system, there are a variety of stoichiometric calcium phosphates. Figure 2 is the phase diagram for the system $CaO\text{-}P_2O_5$ [55]. The compound name, abbreviations, formula and solubility are listed in Table 3 [50]. A brief description of some calcium phosphates is given below, focusing on tricalcium phosphate and hydroxyapatite which are used as resorbable bioceramics for bone substitutes.

Tricalcium phosphate (TCP) was shown as early as 1920 to accelerate bone defect healing. It has been found in several pathological calcifications as a single phase or associated with other phosphates [11]. In Driskell's study [56], the beta-tricalcium phosphate (β-$Ca_3(PO_4)_2$, β-TCP) showed good bioresorbability and the resorption process continued for approximately six to 18 months [57]. The implant has a shelf life of at least eight years. TCP was also reported to have better bioresorbability than hydroxyapatite [58,59]. In combination with HA, β-TCP is also used as a "biphasic calcium phosphate (BCP)" as a bone-substitution ceramic [60-63]. Whitelockite is a term for the mineral or synthetic materials in which Mg^{2+} and HPO_4^{2-} ions substitute in β-TCP structure. It occurs in various pathological calcifications [64] and as a major constituent of human dental calculus [65]. Its solubility is remarkably lower than the pure β-TCP [66], which is a reflection of the increased stability of the lattice [67].

Alpha-tricalcium phosphate (α-$Ca_3(PO_4)_2$, α-TCP) is a metastable phase at room temperature, prepared by heating β phase up to 1125°C. α-TCP is more reactive in aqueous

systems than β-TCP and is considered to be a biological precursor of the apatitic phase since it can be hydrolyzed to various reaction products [68-71]. Dicalcium phosphate dihydrate ($CaHPO_4 \cdot 2H_2O$, DCPD) forms below pH 5.5, octacalcium phosphate ($Ca_8H_2(PO_4)_6 \cdot 5H_2O$, OCP) forms at pH 5.5–7.5, and HAp above pH 7.5 [68]. The HAp produced by this cement-type reaction exists over a compositional range and Ca/P ratio varies from 1.5 to 1.67 [72]. These "nonstoichiometric" HAp compositions are more soluble than stoichiometric HAp, and are assumed to incorporate into bone more readily by osteocytes. Hence, α-TCP is used as a cement-type material, which was moldable and could adapt to the bone cavity. Bonding with bone will finally be realized through the converted apatite phase.

Hydroxyapatite ($Ca_{10}(PO_4)_6(OH)_2$ or HAp) is most stable and least soluble of all calcium phosphates in physiological environment. Due to the chemical similarities to bone and teeth mineral, HAp is widely used as a coating for orthopedic (e.g. hip-joint prosthesis) and dental implants [48]. Some investigators suggested that there might be a bonding of HAp with host bone [73,74]. However, pure HAp does not exist in biological systems. It occurs only with nonstoichiometric and ionic substitutions: $Na^+, K^+, Mg^{2+}, Sr^{2+}$ for Ca^{2+}; CO_3^{2-} for PO_4^{3-}; Cl^-, F^- and CO_3^{2-} for OH^-, and some water. It forms the so-called "biological apatite" or dahllite, the main inorganic component of animal and human normal and pathological calcifications [11]. These differences between synthetic HAp and biological bone result in the inability of the body's bone cells to remodel. That is, synthetic HAp has low biodegradability [23]. Moreover, HAp fabrication method, usually sintering at high temperature, represents a significant drawback for these materials, since it limits their shape and size. This often causes problems of adaptation and fixation to the bone cavities where they have to be placed.

Although amorphous calcium phosphate (ACP) is not used as resorbable material, it brings a great attention since it is a transient phase during the formation of calcium phosphates in aqueous systems. Usually, ACP is the first phase that is precipitated from a supersaturated solution prepared by rapid mixing of solutions containing of calcium and phosphate ions [75-78]. The chemical composition of ACP strongly depends on the solution pH value and the concentrations of calcium and phosphate ions in the solution. For example, ACP phases with Ca/P ratios in the range of 1.18:1 (at pH 6.6) to 1.53:1 (at pH 11.7), and

even up to 2.5:1 have been reported [11,79]. The structure of ACP is still uncertain. According to X-ray diffraction experiments, the compounds are amorphous. Electron microscopy of ACP usually reveals spherical particles with typical diameter ranging between 20 and 200 nm. However, it is likely that ACP has an apatitic short-range order based on EXAFS (extended X-ray absorption fine structure) data for the natural bone and synthetic materials [80,81]. On the other hand, ACP was proposed to consist of roughly spherical $Ca_9(PO_4)_6$ clusters with a diameter of 9.5 nm, so-called Posner's clusters (PC), closely packed to form larger spherical particles with water in the interstices [82,83]. These clusters were found experimentally as seed nuclei during the crystallization of HAp, and a model was developed to describe the crystallization of HAp as a stepwise assembly of these units [84]. Biologically, ACP (often containing magnesium, carbonate, and pyrophosphate) is found in soft-tissue pathological calcifications (e.g. heart-valve calcifications of uremic patients) [10,12].

3. Crystal structure of tricalcium phosphate and hydroxyapatite

α-TCP crystallizes in the monoclinic space group $P2_1/a$ with lattice parameters a = 12.887(2), b = 27.280(4), c = 15.219(2) Å, β = 126.20(1)° with 24 formula units per unit cell [85]. The structure is comprised of columns of Ca^{2+} and PO_4^{3-} ions parallel to the c-axis arranged as shown in Figure 3. There are cation columns, ···Ca Ca Ca Ca···, and cation-anion columns, ···PO_4 Ca PO_4 □ PO_4 Ca PO_4 □ PO_4 Ca PO_4···, where □ indicates a vacant site. These columns are arranged to form a pseudohexagonal pattern: each cation column is surrounded by six cation-cation and cation-anion columns. There is a prominent approximate subcell with b-axis parameter of $b/3$ (9.09Å). This corresponds to the hexagonal HAp a-axis parameter, while half the c-axis parameter of α-TCP corresponds to the c-axis parameter of HAp. The hexagonal HAp structure can thus be derived from α-TCP by replacing the cation-cation columns at the corners of the HAp cell by anion columns. The remaining cation columns in α-TCP become the columnar Ca(1) ions in HAp, whilst the PO_4^{3-} and Ca^{2+} ions that form the cation-anion columns in α-TCP have approximately the same positions as

the PO_4^{3-} and Ca(2) ions in HAp. The hexagonal HAp unit cell is marked as dashed-dotted lines in the Figure 3.

β-TCP possesses the rhombohedral space group R3C with unit cell a = 10.439(1), c = 37.375(6) Å (hexagonal setting) with 21 formula units per hexagonal unit cell [79]. Similar to α-TCP, the structure can be described as two types of columns (A & B), arranging in the hexagonal unit cell along the c-axis [79]. The A column has the form of ···P(1)O_4 Ca(4) Ca(5) P(1)O_4···, while the B column ···P(3)O_4 Ca(1) Ca(3) Ca(2) P(2)O_4 P(3)O_4···. Each column is surrounded by six others, but with alternating displacements from each other in the c-axis direction to provide the oxygen coordination of the Ca^{2+} ions [67,79,86]. The coordination number for Ca sites are: Ca(1) = 7, Ca(2) = 6 or 8, Ca(3) = 8, Ca(4) = 3, and Ca(5) = 6. The Ca(4) cation site is on the three-fold axis and has an unusual coordination to the O(9), O(9'), O(9") face of the P(1)O_4 group. The Ca···O(9) bonds are long (3.041(1) Å) in accord with Pauling's rule. There was only one Ca^{2+} ion per pair of Ca(4) sites in a column to maintain the charge balance. For the Ca(5) site, the coordination is essentially octahedral with no shared PO_4 edges, and all six Ca···O distances are relatively short, falling into the range 2.238-2.287 Å. These two sites are very suitable for the smaller cation ions, but are highly constrained for a Ca^{2+} ion [67,86]. Sheroeder et al reported that, in the Mg-containing β-TCP, Mg^{2+} ions with ionic radius 0.57Å could substitute Ca(4) and Ca(5) positions up to 15% [67]. The Mg(4)···O(9) bonds were 2.907Å, about 0.134Å shorter than that of Ca(4)···O(9) bonds. The approach of O···Mg(5)···O angles toward 90° with increasing Mg content provides further confirmation of the trend toward a more ideal octahedral configuration.

According to the structure, each formula unit occupies 180 $Å^3$ in α-TCP compared with 168 $Å^3$ in the β form. α-TCP is therefore a less compact structure than β-TCP and has a higher internal energy; this is consistent with the α modification being the high temperature form and having a higher reactivity in water than β-TCP.

Pure HAp crystallizes in the monoclinic space group $P2_1/b$ and lattice parameters a = 9.4214(8), b = 2a, c = 6.8814(7) Å, and γ= 120° [87]. At temperatures above 250°C, there is a monoclinic to hexagonal phase transition in HAp (space group $P6_3/m$) [79,88,89]. During

biomineralization and chemical precipitation from aqueous solution, the partial substitution of hydroxide by some impurities, such as fluoride or chloride ions, and nonstoichiometry may stabilize the hexagonal structure of HAp at ambient temperature. The approximate lattice parameters are a = 9.4 Å and c = 6.9 Å with two formula units per unit cell in the hexagonal structure [79]. The OH^- ions are at z = ¼ (Figure 5). In the monoclinic system, there is a short range ordering of the OH^- ion columns along the same direction of displacement from z = ¼. This ordered arrangement of OH^- ions changes the mirror planes in $P6_3/m$ into b glide planes in $P2_1/b$, and doubled the b-axis parameter.

The structural details of the carbonate apatite have been controversial, and remain subject to uncertainty. Its crystal structure is still based on the hexagonal symmetry. According to IR absorption spectra and the a-axis parameters relative to those of HAp, the carbonate apatites were classified to two types, A-type and B-type. A-type carbonate apatite has an larger a-axis parameter with the CO_3^{2-} ions on the six-fold screw axis to replace OH^-, and the B-type has a smaller a-axis parameter and CO_3^{2-} ion position corresponding to PO_4^{3-} ion sites. In biological apatites, a small fraction of the CO_3^{2-} ions replace OH^- ions and most of them adsorbed on the crystal surfaces [90,91].

New approach of biomaterials design emphasizes a more biologically based method of repair/regeneration of tissues. The resorbable calcium phosphates are a promising synthetic substitute to fulfill requirements for the reconstruction of bone defects. It can be made more bioactive by doping the trace elements which may stimulate specific cellular responses at the level of molecular biology. Even though the basic questions concerning crystallography, thermodynamics, and phase relationships have been answered, there are still many open questions within the area of calcium phosphate chemistry. Related to the biological formation of calcium phosphates, issues including rate of crystallization, control of morphology, incorporation of foreign ions, and interaction with biomolecules remain hot topics and are not well understood even today. A better understanding of structure, formation, dissolution and mineralization of these materials will lead to improve their properties for bone and teeth substitutes.

References

1. Wei X, Akinc M. Si,Zn-modified tricalcium phosphates: A phase composition and crystal structure study. Key Engineering Materials 2005;284-286:83-86.

2. Wei X, Akinc M. Crystal structure analysis of Si, Zn-modified Tricalcium phosphate by Neutron Powder Diffraction. to be submitted.

3. Wei X, Ugurlu O, Akinc M. Dissolution behavior and cytotoxicity test of Si, Zn-modified tricalcium phosphate. to be submitted.

4. Wei X, Ugurlu O, Akinc M. Hydrolysis of α-Tricalcium Phosphate in Simulated Body Fluid at 37°C. to be submitted.

5. Wei X, Akinc M. Resorption Rate Tunable Bioceramic: Si&Zn-Modified Tricacium Phosphate. In: Mizuno M, editor. Ceramic Engineering and Science Proceedings (the 29th International Conference on Advanced Ceramics and Composites - Advances in Bioceramics and Biocomposites). Cocoa Beach, FL: The American Ceramic Society, 2005. p. 129 - 136.

6. Bills PM, Wheeler EJ. Bone-a composite material. J Ed Mod Mater Sci Eng 1982;4:395-455.

7. Mullem PJv, Maltha JC. Histology of Bone: A Synopsis. Boca Raton, Florida: CRC Press, 1983.

8. LeGeros RZ, LeGeros JP, Daculsi G, Kijkowaka R. Encyclopedic Handbook of Biomaterials and Bioengineering. New York: Marcel Deker, 1995.

9. Hollinger J, McAllister B. Bone and its repair. In: Wilson J, Hench L, Greenspan D, editors. Bioceramics, Proceedings of the International Symposium on Ceramics in Medicine 1995; Ponte Vedra: Elsevier; 1995. p. 3-10.

10. LeGeros R. Apatites in biological systems. Progress in Crystal Growth and Characterization 1981;4(1-2):1-45.

11. LeGeros RZ. Calcium phosphates in oral biology and medicine. Basel, Switzerland: S Karger, 1991.

12. LeGeros RZ, LeGeros JP. Phosphate Minerals in Human Tissue. New York: Springer-Verlag, 1984.

13. Herring G. The organic matrix of bone. New York: Academic Press, 1972.

14. Wuthier RE. A review of the primary mechanism of endochondral calcification with special emphasis on the role of cells, mitochondria and matrix vesicles. Clinical Orthopaedics and Related Research 1982;169( ):219-242.

15. Veis A, Sharkey M, Dickens L. Non-collagenous proteins of bone and dentin extracellular matrix and their role in organized mineral deposition. New York: Elsevier, 1977.

16. Ennever J, Boyan-Salyers B, Riggan LJ. Proteolipid and bone matrix calcification in vitro. Journal of Dental Research 1977;56(8): 967-970.

17. Termine JD, Belcourt A, Conn K, Kleinman H. Mineral and collagen-binding proteins of fetal calf bone. J Biol Chem 1981;256:10403-10408.

18. Boskey AL. Current concepts in physiology and biochemistry of calcification. Clinical Orthopaedics and Related Research 1981;157:225-257.

19. Boskey A. Overview of cellular elements and macromolecules implicated in the initiation of mineralization. Birmingham: BSCO Media, 1985.

20. Brown WE. A mechanism for growth of apatitic crystals. Bristol: John Wright, 1969.

21. Glimcher M. Recent studies of the early mineral deposits in bone and enamel, and of the organic matrix of enamel. Calc Tiss Res 1968;Suppl.:1.

22. Brown WE, Chow LC. Chemical properties of bone mineral. Annual review of materials science 1976;6:213-236.

23. Yaszem MJ, Payne RG, Hayes WC, Langer R, Mikos AG. Evolution of bone transplantation: molecular, cellular and tissue strategies to engineer human bone. Biomaterials 1996;17:175-165.

24. Robinson RA, Watson ML. Crystal-collagen relationship in bone as observed in the electron microscope. Ann NY Acad Sci 1955;60:596.

25. Harper RA, Posner AS. Measurement of non-crystalline calcium phosphate in bone mineral. Proc Soc Exp Biol Med 1966;122:137.

26. Termine JD, Posner AS. Amorphous/crystalline interrelationships in bone mineral. Calc Tiss Res 1967;1:8-23.

27. Fleisch H. Role of nucleation and inhibition in calcification. Clin Orthoped 1964;32:170-180.

28. Boskey A. Current concepts of the biochemistry and physiology of calcification. Clin Orthoped 1980;157:165-174.

29. Glimcher M. Molecular biology of mineralized tissues with reference to bone. Rev Mod Phys 1959;31:359-393.

30. Strates B, Neuman W. On the mechanism of calcification. Proc Soc Exp Biol Med 1958;97:688-691.

31. Raisz LG. Pathogenesis of osteoporosis: Concepts, conflicts, and prospects. Journal of Clinical Investigation 2005;115(12):3318-3325.

32. Wiesmann H-P, Tkotz T, Joos U, Zierold K, Stratmann U, Szuwart T, et al. Magnesium in newly formed dentin mineral of rat incisor. Journal of Bone and Mineral Research 1997;12(3):380-383.

33. Althoff J, Quint P, Krefting ER, Hoehling HJ. Morphological studies on the epiphyseal growth plate combined with biochemical and x-ray microprobe analyses. Histochemistry 1982;74(4):541-552.

34. Bigi A, Foresti E, Gregorini R, Ripamonti A, Roveri N, Shah JS. The role of magnesium on the structure of biological apatites. Calcified Tissue International 1992;50(5):439-444.

35. Nielsen FH. Ultratrace elements in nutrition. Annual Review of Nutrition 1984; 4:21-41.

36. Carlisle EM. Silicon: a requirement in bone formation independent of vitamin D. Calcif Tissue Int 1981;33(1):27-34.

37. Olson RE, Doisy AA. Clinical nutrition, an interface between human ecology and internal medicine. Nutrition Reviews 1978;6:161-178.

38. Ohnesorge FK, Wilhelm M. Weinheim: Verlag Chemie, 1991.

39. Barrea RA, Perez CA, Ramos AY. Zinc incorporation in human dental calculus. J Synchrotron Rad 2001;8:990-992.

40. Driessens F, Verbeeck. R. Biominerals. Boston: CRC Press, 1990.

41. Shannon RD. Revised effective ionic radii and systematic studies of interatomic distances in halides and chalcogenides. Acta Crystallographica, Section A: Crystal Physics, Diffraction, Theoretical and General Crystallography A 1976;32(5):751-767.

42. Calhoun NR, Smith JC, Jr., Becker KL. The role of zinc in bone metabolism. Clinical orthopaedics and related research 1974(103):212-234.

43. Yamaguchi M, Oishi. H. Stimulatory effect of zinc on bone formation in tissue culture. Biochem Pharmacol 1987;36:4007-4012.

44. Yamaguchi M, Oishi H. Zinc stimulation of bone protein synthesis in tissue culture. Biochem Pharmacol 1988;37:4075-4080.

45. Walsh PM, O'Connor JM, Strain JJ. The role of trace elements in bone health. Nutritional Aspects of Bone Health 2003:351-368.

46. Rico H. Minerals and Osteoporosis. Osteoporosis Int 1991;2:20-25.

47. Carlisle EM. A silicon requirement for normal skull formation in chicks. The Journal of nutrition 1980;110(2):352-359.

48. Hench LL. Bioceramics. Journal of American Ceramic Society 1998;81(7):1705-1728.

49. Ratner BD. Biomaterials Science: an introduction to materials in medicine. San Diego: Academic Press, 1996.

50. Dorozhkin SV, Epple M. Biological and Medical Significance of Calcium Phosphates. Angewandte Chemie, International Edition 2002;41(17):3130- 3146.

51. Hench L. From Concept to Clinic. J Am Ceram Soc 1991;74(7):1487-1510.

52. Hench LL. Biomaterials: a forecast for the future. Biomaterials 1998;19(16):1419-1423.

53. de Groot K. Bioceramics of calcium phosphate. Boca Raton, Florida: CRC Press, 1983.

54. de Groot K, Klein CPAT, Wolke JGC, de Blieck-Hogervorst JMA. Chemistry of calcium phosphate bioceramics. Boca Raton, FL: CRC Press, 1990.

55. Kreidler E, Hummel F. Phase relationships in the system SrO- P2O5 and the influence of water vapor on the formation of Sr4P2O9. Inorg Chem 1967;6:884-891.

56. Driskell TD, Hassler CR, McCoy LR. Significance of resorbable bioceramics in the repair of bone defects. Proceedings of the Annual Conference on Engineering in Medicine and Biology; 1973; 1973. p. 199.

57. Metsger DS, Driskell TD, Paulsrud JR. Tricalcium phosphate ceramic-a resorbable bone implant: review and current status. J Am Dent Assoc 1982;105:1035-1038.

58. Klein C, Driessen AA, de Groot K, A. VDH. Biodegradation behavior of various calcium phosphate materials in bone tissue. J Biomed Mater Res 1983;17:769-784.

59. Whittaker JM, James RA, Lozada J, Cordova C, GaRey DJ. Histological response and clinical evaluation of heterograft and allograft materials in the elevation of the maxillary sinus for the preparation of endosteal dental implant sites. Simultaneous sinus elevation and root form implantation: an eight-month autopsy report. J Oral Implant 1989;15:141-144.

60. Daculsi G. Biphasic calcium phosphate concept applied to artificial bone, implant coating and injectable bone substitute. Biomaterials 1998;19(16):1473-1478.

61. Daculsi G, Bagot d'Arc M, Corlieu P, Gersdorff M. Macroporous biphasic calcium phosphate efficiency in mastoid cavity obliteration: experimental and clinical findings. The Annals of otology, rhinology, and laryngology 1992;101(8):669-674.

62. Daculsi G, Gauthier O, Guicheux J, Bouler JM, Aguado E. Macroporous biphasic calcium phosphate ceramic, a carrier for human growth hormone. Bioceramics, Proceedings of the International Symposium on Ceramics in Medicine 1998;11:525-528.

63. Daculsi G, LeGeros RZ, Nery E, Lynch K, Kerebel B. Transformation of biphasic calcium phosphate ceramics in vivo: ultrastructural and physicochemical characterization. Journal of Biomedical Materials Research 1989;23(8):883-894.

64. Rowles SL. Precipitation of whitlockite from aqueous solutions. Bulletin de la Societe Chimique de France 1968(Spec. No.):1797-1802.

65. Jensen AT, Rowles SL. Magnesian whitlockite, a major constituent of dental calculus. Acta Odontologica Scandinavica 1957;15:121-139.

66. Chickerur NS, Lenka RC, Sabat BB, Nayak GH. Solubility behavior of synthetic whitlockite containing magnesium in aqueous medium. Indian Journal of Chemistry, Section A: Inorganic, Physical, Theoretical & Analytical 1986;25A(2):181-182.

67. Schroeder LW, Dickensand B, Brown. WE. Crystallographic Studies of the Role of Mg as a Stabilizing Impurity in β-tricalcium phosphate: II. Refinement of Mg-containing β-tricalcium phosphate. J Solid state Chemistry 1977;22:253-262.

68. Durucan C, Brown PW. α-Tricalcium phosphate hydrolysis to hydroxyapatite at the near physiological temperature. Journal of Materials Science: Materials in Medicine 2000;11:365-371.

69. Monma H, Ueno S, Kanazawa T. Properties of hydroxyapatite prepared by the hydrolysis of tricalcium phosphate. J Chem Tech Biotechnol 1981;31:15-24.

70. Li Y, Zhang X, de Groot K. Hydrolysis and phase transition of alpha-tricalcium phosphate. Biomaterials 1997;18:737-741.

71. Durucan C. Formation of hydroxyapatite by hydrolysis of alpha-tricalcium phosphate: The Pennsylvania State University; 2003.

72. Monma H, Kanazawa. T. The hydration of α-tricalcium phosphate. Yogio-Kyoki Shi 1976;84:209.

73. Jarcho M, Kay JF, Gumaer KI, Doremus RH, Drobeck HP. Tissue, cellular and subcellular events at a bone-ceramic hydroxylapatite interface. Journal of Bioengineering 1977;1(2):79-92.

74. Denissen HW, de Groot K, Makkes PC, van den Hooff A, Klopper PJ. Tissue response to dense apatite implants in rats. Journal of biomedical materials research 1980;14(6):713-721.

75. Termine JD, Eanes ED. Comparative chemistry of amorphous and apatite calcium phosphate preparations. Calcif Tissue Res 1972;10:171.

76. Eanes ED, Termine JD, Nylen MU. Electron microscopic study of the formation of amorphous calcium phosphate and its transformation to crystalline apatite. Calcified Tissue Research 1973;12(2):143-158.

77. Meyer JL, Eanes ED. A thermodynamic analysis of the secondary transition in the spontaneous precipitation of calcium phosphate. Calcified Tissue Research 1978;25(3):209-216.

78. Meyer JL, Eanes ED. A thermodynamic analysis of the amorphous to crystalline calcium phosphate transformation. Calcified Tissue Research 1978;25(1):59-68.

79. Elliott JC. Structure and Chemistry of the Apatites and other Calcium Orthophosphates. London: Elsevier, 1994.

80. Harries JE, Hukins DWL, Hasnain SS. Analysis of the EXAFS spectrum of hydroxyapatite. Journal of Physics C: Solid State Physics 1986;19(34):6859-6872.

81. Harries JE, Hukins DWL, Holt C, Hasnain SS. Conversion of amorphous calcium phosphate into hydroxyapatite investigated by EXAFS spectroscopy. Journal of Crystal Growth 1987;84(4):563-570.

82. Posner AS, Betts F. Synthetic amorphous calcium phosphate and its relation to bone mineral structure. Acc Chem Res 1975;8:273-281.

83. Betts F, Posner AS. X-ray radial distribution study of amorphous calcium phosphate. Materials Research Bulletin 1974;9(3):353-360.

84. Onuma K, Ito A. Cluster Growth Model for Hydroxyapatite. Chem Mater 1998;10:3346-3351.

85. Mathew M, Schroeder L, Dickens B, Brown W. The crystal structure of α-Ca3(PO4)2. Acta Cryst 1977;B33:1325-1333.

86. Dickens B, Schroeder LW, Brown WE. Crystallographic Studies of the Role of Mg as a Stabilizing Impurity in β-tricalcium phosphate: I. The Crystal Structure of Pure β-tricalcium phosphate. J Solid state Chemistry 1974;10:232-248.

87. Suetsugu Y. Single crystal growth and structure analysis of monoclinic hydroxyapatite. Key Engineering Materials 2001;192-195:287-290.

88. Rangavittal N, Landa-Canovas AR, Gonzalez-Calbet JM, Vallet-Regi M. Structural study and stability of hydroxyapatite and β-tricalcium phosphate: two important bioceramics. Journal of Biomedical Materials Research 2000;51(4):660-668.

89. Kim JY, Fenton RR, Hunter BA, Kennedy BJ. Powder diffraction studies of synthetic calcium and lead apatites. Australian Journal of Chemistry 2000;53(8):679-686.

90. Daculsi G, LeGeros RZ, Heughebaert M, Barbieux I. Formation of carbonate-apatite crystals after implantation of calcium phosphate ceramics. Calcif Tissue Int 1990;46:20-27.

91. Elliott JC, Holcomband DW. Infrared determination of the degree of substitution of hydroxyl by carbonate ions in human dental enamel. Calcif Tissue Int 1985; 37:372-375.

Table 1 The Composition of Human Bone (Dry Weight) [40]

Major Composition		Trace Elements Concentration (ug g^{-1} Dry Weight)			
Component	Concentration (wt%)	Element	Range	Element	Range
Ca	36.6	Li	1-26	As	0.011
P	17.1	Be	0-4	Se	0.1-21
CO_2	4.8	B	2-4	Br	1-5
Na	1.0	Al	3-241	Rb	0.3-0.7
K	0.07	Si	3-40	Sr	75-150
Mg	0.6	S	0.69-1.83%[a]	Zr	0.3-6
Sr	0.05	Ti	0.1-2	Mo	0-0.1
Cl	0.1	V	0.04-8	Ag	1-19
F	0.1	Cr	0.1-6	Cd	1-8
		Mn	0.2-26	Sn	3-13
		Fe	3-120	Sb	0-3
		Co	0-0.4	Ba	20-5940
		Ni	2-18	Hg	0.012
		Cu	1-3860	Pb	10-50
		Zn	50-280	Rare earths	0.001-2.2

[a] Weight percent.

Table 2 Factors Affecting Implant-Tissue Interfacial Response [48]

Tissue Side	Implant Side
Type of Tissue	Composition of Implant
Health of Tissue	Phases in Implant
Age of Tissue	Phase Boundaries
Blood Circulation in Tissue	Surface Morphology
Blood Circulation at Interface	Surface Porosity
Motion at Interface	Chemical Reactions
Closeness of Fig	Closeness of Fit
Mechanical load	Mechanical load

Table 3 Solubility product constants of calcium phosphates compounds at 37° [49]

Compound	Formula	pK_{sp}
Dicalcium phosphate dihydrate (DCPD)	$CaHPO_4 \cdot 2H_2O$	6.63
Dicalcium phosphate anhydrous (DCPA)	$CaHPO_4$	7.02
Octacalcium phosphate (OCP)	$Ca_8H_2(PO_4)_6 \cdot 5H_2O$	95.9
α-Tricalcium phosphate (α-TCP)	$\alpha - Ca_3(PO_4)_2$	25.5
β-Tricalcium phosphate (β-TCP)	$\beta - Ca_3(PO_4)_2$	29.5
Hydroxyapatite (HAp)	$Ca_{10}(PO_4)_6(OH)_2$	117.2
Calcium-deficient hydroxyapatite (CDHA)	$Ca_{10-x}(HPO_4)_x(PO_4)_{6-x}(OH)_{2-x}$ $(0<x<1)$	~85.1
Amorphous calcium phosphate (ACP)	$Ca_x(PO_4)_y \cdot nH_2O$	25-33
Tetraclacium phosphate (TTCP)	$Ca_4(PO_4)_2O$	37-42
Fluorapaatite (FAp)	$Ca_{10}(PO_4)_6F_2$	137

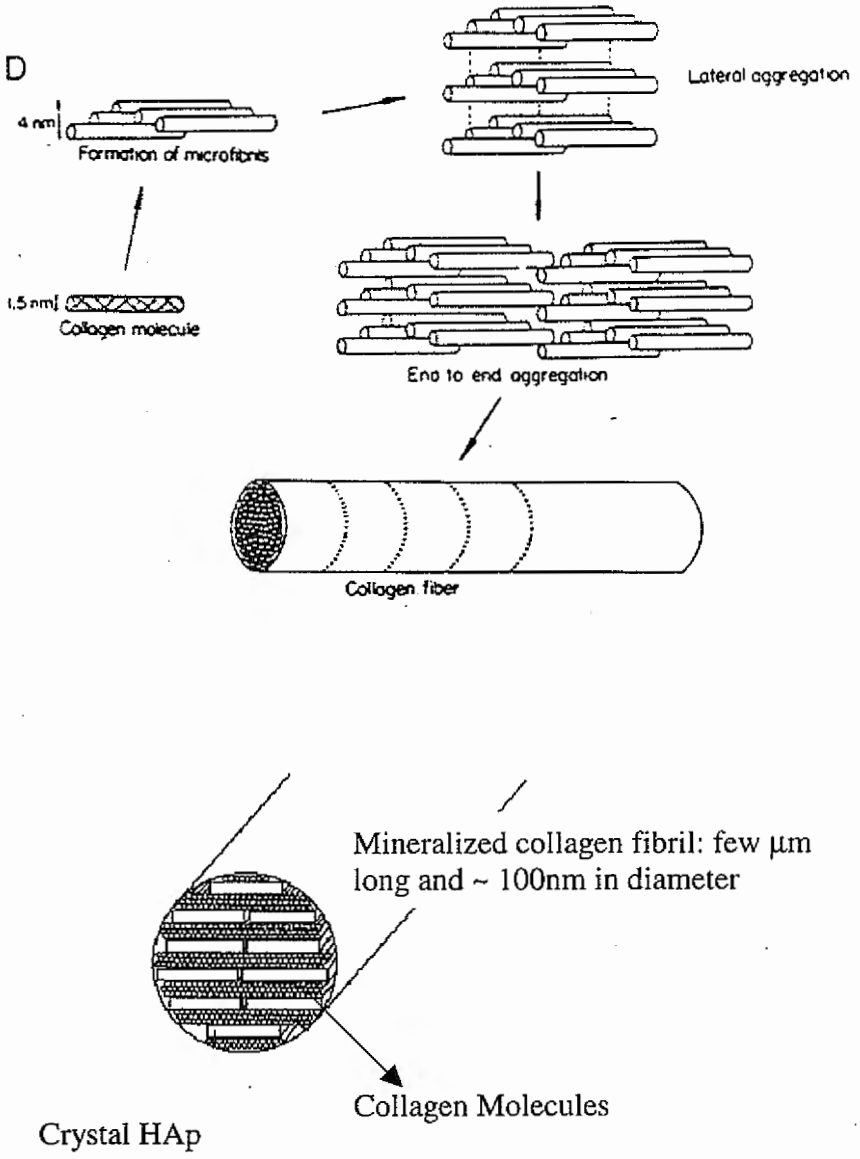

Figure 1. The organization of collagen framework and the mineralized collagen fibril [50].

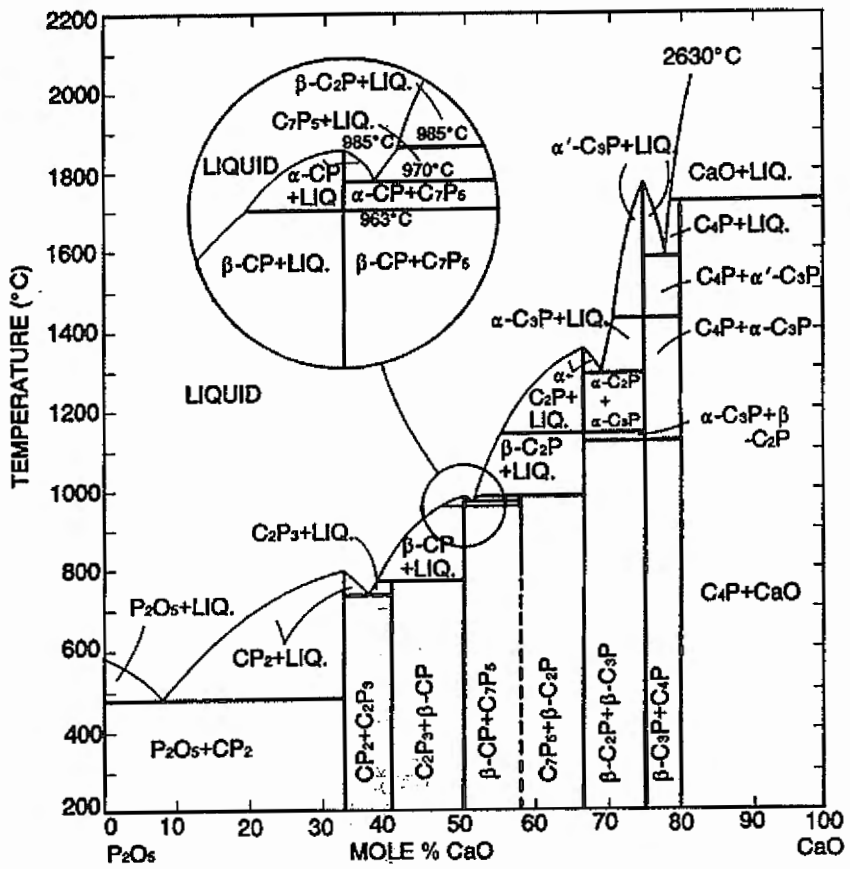

Fig. 2 Phase diagram for the system CaO-P_2O_5 (C=CaO, P= P_2O_5) [55], in which

$CP_2 \Rightarrow CaO{\cdot}2P_2O_5 \Rightarrow CaP_4O_{11}$

$C_2P_3 \Rightarrow 2CaO{\cdot}3P_2O_5 \Rightarrow Ca_2P_6O_{17}$

$CP \Rightarrow CaO{\cdot}P_2O_5 \Rightarrow CaP_2O_6$

$C_7P_5 \Rightarrow 7CaO{\cdot}5P_2O_5 \Rightarrow Ca_7P_{10}O_{32}$

$C_2P \Rightarrow 2CaO{\cdot}P_2O_5 \Rightarrow Ca_2P_2O_7$

$C_3P \Rightarrow 3CaO{\cdot}P_2O_5 \Rightarrow Ca_3(PO_4)_2$

$C_4P \Rightarrow 4CaO{\cdot}P_2O_5 \Rightarrow Ca_4(PO_4)_2O$

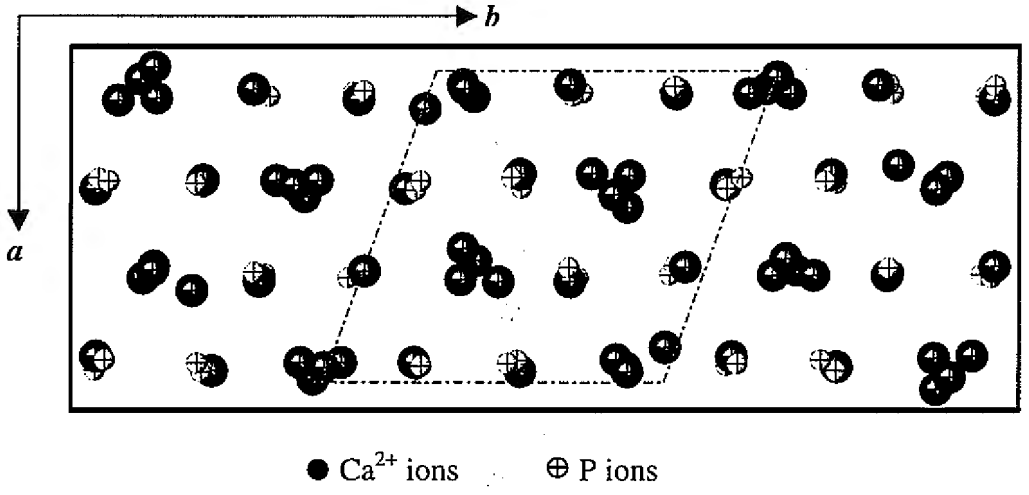

(a)

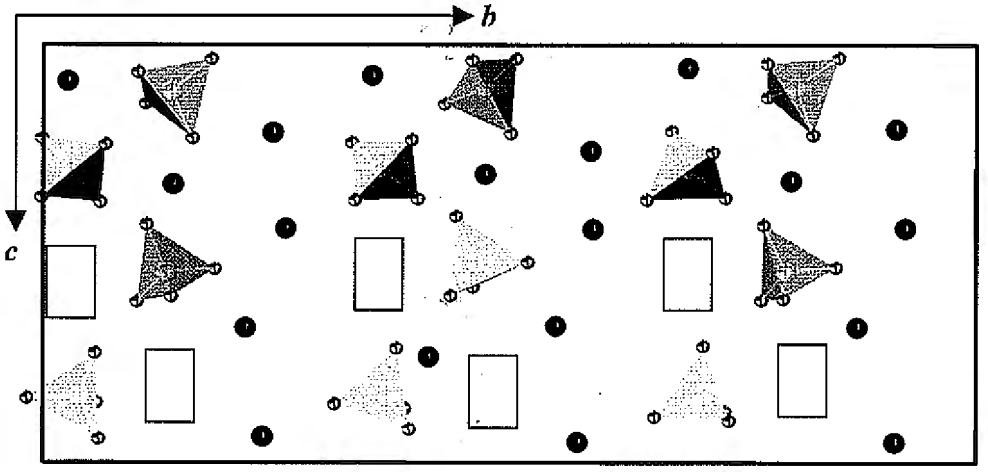

(b)

Figure 3 Projection of the α-TCP structure (a) along the [001] direction. Only the calcium and phosphorus atoms are shown. Two-column structure: Cations column and Cation-anion column. The dashed-dotted lines outline the hexagonal HAp unit cell. (b) along the [100] direction. shows the Ca vacancies.

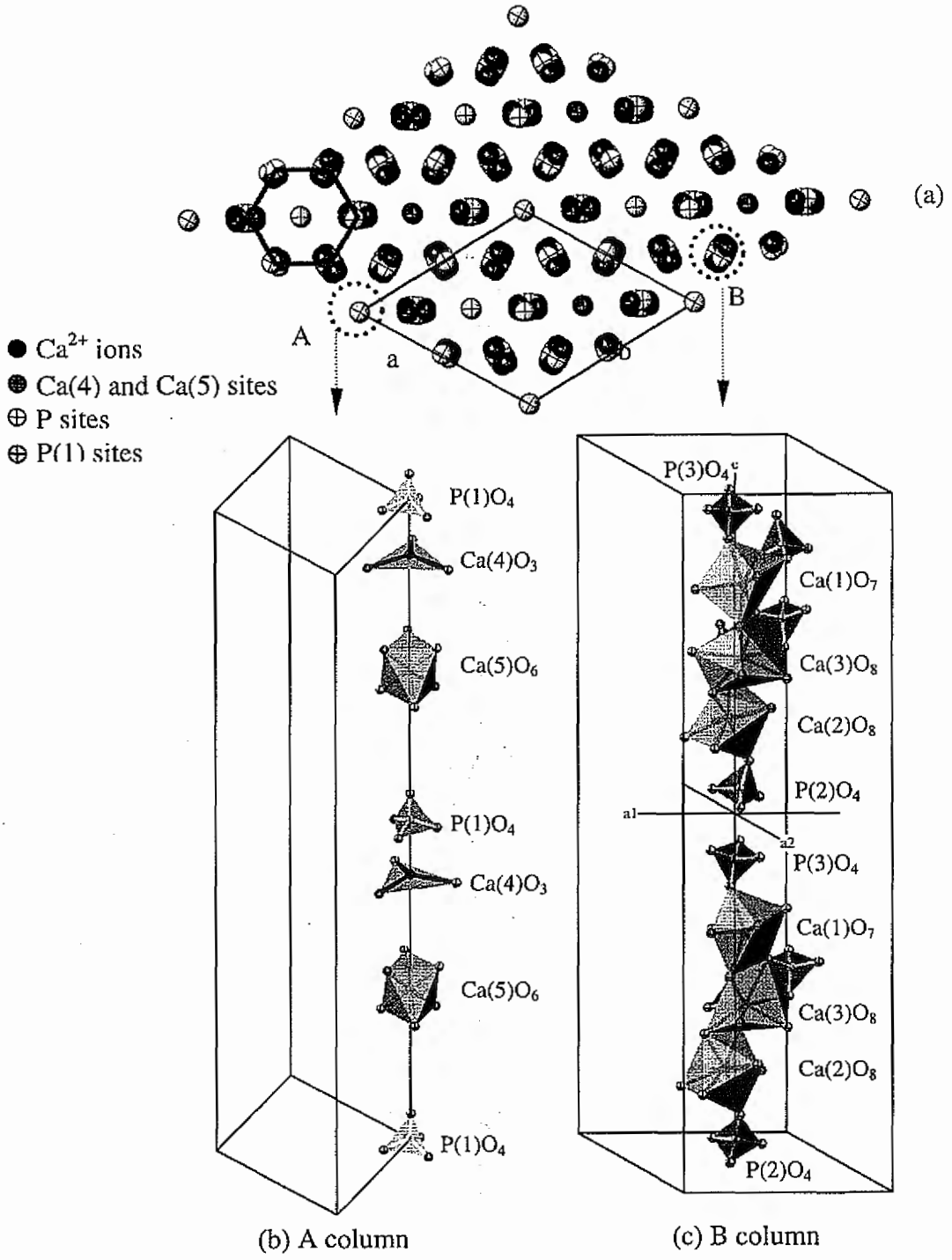

Figure 4 (a) Projection of the crystal structure of β-TCP along the [001] direction, showing the hexagonal unit cell with A and B columns. Oxygen atoms were deleted for the clearer structure image. (b) and (c) are the configuration of CaOn and PO_4 groups in the A and B columns, respectively, along the *c*-axis of the hexagonal cell.

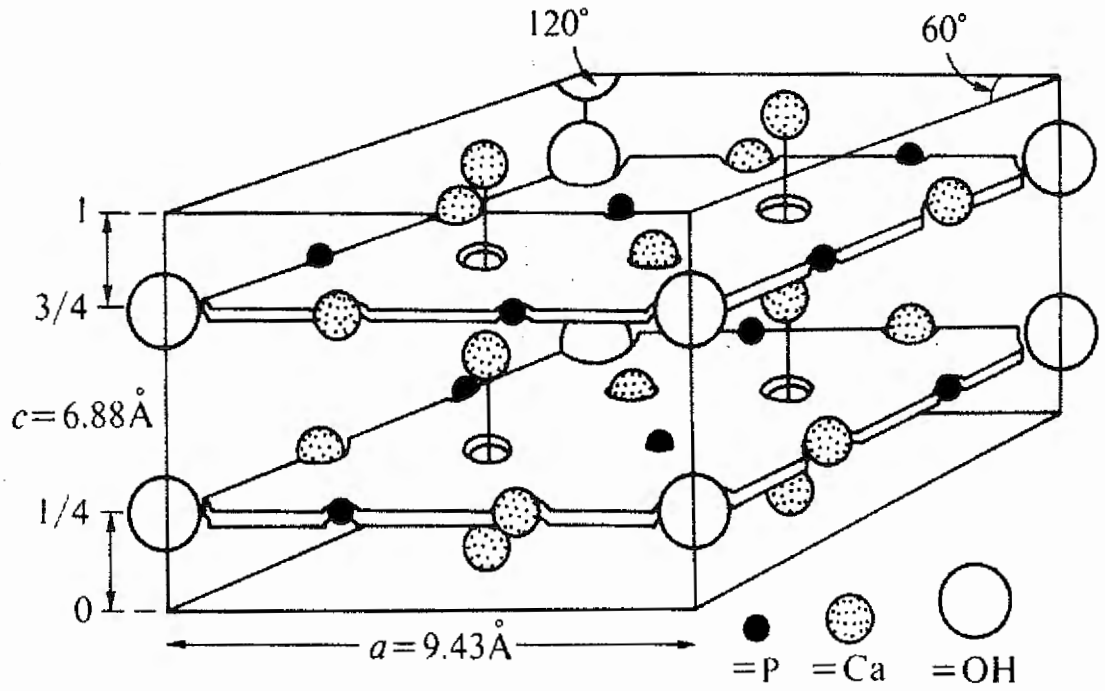

Figure 5 Simple apatite hexagonal system (PO_4 tetrahedrons are represented by a phosphorus atom) [77]

CHAPTER 2: BACKGROUND AND LITERATURE REVIEW ON THE DISSOLUTION BEHAVIOR OF CALCIUM PHOSPHATES

This section presents the basic thermodynamic and kinetic theories on the stability of solid salts in the aqueous solution, and then focuses on the solubility and dissolution of calcium phosphates. Review of the literature on the role of additives on the dissolution behavior is also presented.

2.1 Stability of solid salts in aqueous solution

Solubility is defined as the maximum concentration of solute in the solution under the equilibrium conditions. This concept of solubility is a very convenient way to know how much of the material has actually dissolved into the solution. However, it is not convenient for showing general solubility of the material since its value depends on the pH of the solution. Therefore, a thermodynamic equilibrium constant known as the solubility product constant K_{sp} is used for sparingly soluble salts. It describes the equilibrium state between a mineral compound and an aqueous phase. The reaction that controls this equilibrium for a single compound AX can be represented by

$$AX(s) \leftrightarrow A^{n+}(aq) + X^{n-}(aq) \tag{2.1}$$

where (s) indicates solid and (aq) aqueous states, respectively. Change in Gibbs free energy in above equation is represented by [1]:

$$\frac{\Delta G}{RT} = \frac{\mu^0_{A,aq} + \mu^0_{X,aq} - \mu_{AX,s}}{RT} + \ln IP^{AX} \tag{2.2}$$

where μ^0 is the molar Gibbs free energy under normal conditions of ionic species in solution; $\mu_{AX,s}$ is the Gibbs free energy of the solid compound; and IP^{AX} is the ionic activity product of compound AX. The ionic activity product of compound AX in solution is defined as

$$IP^{AX} = (A^{n+})(X^{n-}) \tag{2.3}$$

where (A^{n+}) *and* (X^{n-}) are the molar activity of cation and anion, respectively. In a state of equilibrium $\Delta G = 0$, so that Equation 2.4 can be expressed by

$$\frac{\mu^0_{A,ac} + \mu^0_{X,ac} - \mu_{AX,s}}{RT} = -\ln IP^{AX} \equiv -\ln K^{AX}_{sp} \qquad (2.4)$$

$\mu_{AX,s}$ is a constant for a pure solid of fixed composition and μ^0_i are fixed at a determined temperature and pressure. Therefore, the equation shows the ionic activity product for compound *AX* in a saturated aqueous solution must also be constant. This constant is called the thermodynamic solubility product, or solubility product.

When $\Delta G \neq 0$, the dissolution or precipitation will proceed in the aqueous solution. The driving force controlling dissolution and precipitation reactions are based on super-/under-saturation levels or the Gibbs free energy of transfer from supersaturated to an assumed saturated solution at surface or inverse. Derived from Equation 2.2, the driving force can be expressed as [2]:

$$\Delta G = (RT/\nu)\ln(IP/K_{SO}) = (RT/\nu)\ln S \qquad (2.5)$$

where K_{SO} is the equilibrium constant or the ionic activity product at equilibrium ($K_{SO} = K_{SP}/[AX]$, [*AX*]~1 for the slightly soluble solid), ν is the number of ions in the molecule, and *S* is defined as the thermodynamic saturation level. Hence, the direction of the dissolution/precipitation is determined by the difference between the *IP* and the equilibrium constant K_{SO}. When *S*=1, the aqueous solution is saturated with respect to the compound AX. When *S*<1, the aqueous solution is undersaturated and $\Delta G < 0$, which provokes dissolution until saturation is achieved. The dissolution rate will decrease with increasing of *IP*. The reaction of the surface will reverse to precipitation when $S > 1$.

Generally, the dissolution and precipitation rate of calcium phosphates may be interpreted in terms of an empirical kinetic equation [3]:

$$R = km_0 F(\frac{m}{m_0})\sigma^n \qquad (2.6)$$

in which k is the corresponding rate constant, m and m_0 are the masses of solid phase initially and at time t, σ is the relative super- or undersaturations, and n is the kinetic rate order of reaction. The relative super- and understaturation may be expressed in terms of equation 2.7.

$$\sigma = \pm\left[(\frac{IP}{K_{so}})^{1/\nu} - 1 \right] = \pm(S-1) \tag{2.7}$$

The values of *IP* for some calcium phosphates are given by equations 2.8-2.9:

For tricalcium phosphate (TCP),

$$IP = [Ca^{2+}]^3[PO_4^{3-}]^2 y_2^3 y_3^2 \tag{2.8}$$

and stoichiometric hydroxyapatite (HAP),

$$IP = [Ca^{2+}]^{10}[PO_4^{3-}]^6[OH^-]^2 y_1^2 y_2^{10} y_3^6 \tag{2.9}$$

where y_i is the ionic activity coefficient decided by the ionic strength. Since *IP* is tightly related to the concentration, the dissolution and precipitation reaction could be simply implied by the concentration change in the solution. If the ionic concentration C is smaller than the equilibrium concentration C_∞ in the solution, the dissolution happens and the precipitation begins under the opposite condition.

The solubility of a mineral compound AX in aqueous solution can be described with the concentration of the A^{n+} and X^{n-} ions. However, in the case of acidic (e.g. H_nX) or basic compounds (e.g. $A(OH)_n$) it is necessary to use pH as a variable for complete description of solubility. A graph describing the relationship between these variables is called as a solubility diagram. Figure 2.1 is a solubility diagram for a mineral compound *AX* in a hypothetical ternary system of $A(OH)_n$-H_nX-H_2O, which shows the stability regions as function of concentration of A (log[A]) and solution pH. The geometric figure (in the form of a line) in the solubility diagram defines the equilibrium conditions is called a *solubility isotherm*. As shown in Figure 2.1, the solution can be either undersaturated (U) or supersaturated (S). In the first case, the solids tend to dissolve. In the second case, the solids tend to precipitate until equilibrium is reached once again.

More complex aqueous systems comprise compositions that produce more than one solid compound. The singular points of this diagram predict solution-derived precipitation. For example, a singular point (or invariant point) as shown in Figure 2.2, is the intersection of two isotherms, where both salts are equally stable. If these compounds are in a solution more acidic than the singular point (e.g. P_1), the compound *AX* will dissolve. Since the solution at this point is supersaturated with respect to AX_2, the AX_2 will precipitate. In general,

for a given pH value, any salt whose isotherm lies below another, will be relatively more stable than the other. This dissolution and precipitation process continues until pH and composition reaches a singular point. The conclusion would be similar if the initial solution composition is located in a more basic solution relative to the singular point such as P_2. In that case AX_2 will dissolve and AX will precipitate until the singular point is reached [4].

2.2 Calcium phosphate system

According to the solubility product constants (Table 3 in chapter 1), Brown and Chow calculated the solubility isotherms at 37°C over a wide pH range (Figure 2.3) [5]. The solubility of each calcium phosphate was plotted with the concentration of calcium and phosphorus as the function of pH. A common characteristic of the isotherms in Figure 2.3 is that they have a negative slope in the neutral and acid regions (pH ≤ 7). This suggests that these compounds became more soluble when pH decreases as most other basic oxides do. The gradient of the slope shows that the solubility increases as the pH decreases. In general, at a given pH, a salt with its isotherm lying below that of other salts is less soluble and more stable in the solution. There are only two calcium phosphate materials that are stable at room temperature when in contact with aqueous solution. At a pH lower than 4.2, the component DCPD is the most insoluble phase, while at higher pH (>4.2) HAp is the one. HAp and DCPD have equivalent stabilities at pH 4.2, indicating that these two will be the equilibrium assemblages of phases at this pH. This occurs when the solution is mutually and simultaneously saturated with respect to these two solids. Therefore, during the dissolution of other calcium phosphates, HAp or DCPD or both will precipitate when the solution is supersaturated with respect to them, as introduced in the previous section. The gradual transition from these salts to HAp/DCPD surface leads to the change in solubility of other calcium phosphates to a value approaching the solubility of HAp/DCPD. This dissolution and precipitation process continues until pH and composition reaches the singular point.

Ducheyne et al. compared the dissolution rates of six calcium phosphates in calcium and phosphate free solution at pH 7.3. In terms of the dissolution of calcium, the dissolution rate increased from the stoichiometric HAp (s-HAp) to TTCP in the following order [6]:

$$\text{TTCP} > \alpha\text{-TCP} >> \text{OCP} > \beta\text{-TCP} > \text{CDHA} > \text{s-HA}$$

where CDHAp is calcium-deficient hydroxyapatite. Klein et al. [7] proposed the degradation rates of calcium phosphates were determined by neck dissolution rate and neck geometry. The latter factor is dependent on the crystallography, the stoichiometry of the material, and the sintering conditions. It is also worth to note that, contrary to general salts, the solubility of calcium phosphates decrease with the increase of temperature (Figure 2.4), which may be taken into consideration for HAp biomimetic or coating process strategy [8].

2.3 Additives Effect on the Calcium Phosphates

As introduced in Chapter 1, ions with the similar size and charge to the component ions are capable to incorporate into the bone mineral and to substitute Ca^{2+}, PO_4^{3-} or OH^- sites. This leads to the change of the crystal structure, composition, morphology, and even the porosity, which are the principal factors determining the stability and solubility of calcium phosphates. The important influence of impurities on crystallization and dissolution has been the subject of numerous studies [9-19].

As reported, the addition of magnesium to TCP produced β-whitlockite ceramic and reduced the dissolution rate of the TCP [9,16,17,20]. Further investigation suggested that Mg might substitute Ca sites and stabilize TCP structure [21,22], which also effectively suppresses the phase transition from β- to α-TCP. Okazaki presented that Mg-containing HAp dissolve to a greater extent than Mg-free apatites with the subsequent reprecipitation of Mg-poor apatites [23]. The high Mg/Ca in solution favored the reprecipitation of Mg-containing β-TCP rather than HAp. Termine and Posner reported that the presence of Mg^{2+} ions enhanced amorphous apatite (ACP) formation and retard the transformation of ACP into HAp at a given degree of supersaturation [24,25]. Similar to Mg effect, it was found that the solubility of sintered Zn-TCP decreased steeply with an increase in zinc content beyond 0.126 wt%[12,13,26,27]. It decreased to a level of the equilibrium solubility of pure HAp when the zinc content was raised to 3.70wt%. The decrease in solubility was attributed to the increased stability of the TCP structure caused by the addition of zinc ions. On the contrary, zinc addition could increase the solubility of HAp [28]. It was proposed that Zn might produce an increase in the activity of acid phosphatase or induce dissolution of the hydroxyapatite matrix in a biological environment. It was possible that the Zn may form

$Zn(OH)_{2-n}$ species in solution which may, in turn, lower the pH in the vicinity resulting in an increase in the dissolution/resorption of HAp. From the point view of crystallography, Bigi [29] explained that the addition of zinc decreased the crystal size and increased crystal strain of HAp, and so it cannot appreciably substitute for calcium in the HAp structure. Hence, zinc was assumed to be adsorbed on the surface of apatite crystallites and or in the or in the amorphous phase, and thus decrease the stability of HAp.

Due to its important role in biomineralization process, silicon has also been investigated extensively as additives for calcium phosphates. Ionic radii considerations suggested that the most likely substitution site for Si was that of phosphorus. Langstaff et al reported that the dissolution rate of silicon-doped HAp was higher than non-doped one and β-TCP, and it was resorbed when acted upon by osteoclasts [11]. Si substituted HAp was assumed to be more bioactive than pure HAp since it bonded faster to the bone after implantation, ensuring the osteointegration of the materials and reducing the risk of implant failure. Porter et al. confirmed that the in vivo dissolution of Si-HAp increased with the silicon content and it was found to be prevalent at grain boundary and triple junctions [30,31]. Botelho et al. [32] presented that, at physiological pH=7.4, zeta potential of HAp was -50±5 mV, whereas it significantly decreased to -71±5 mV by the presence of silicate groups (0.8 wt% Si) in the HAp lattice. These mechanisms were suggested to be the reason of the good bioactivity. The amount of silicon which can be incorporated into HAp was limited due to the increased distortion of the PO_4 tetrahedra [14,33]. At low silicon levels in HAp, β-TCP would form as the secondary phase, while high silicon levels favored α-TCP[15,34]. Some results revealed that Cl^-, F^- and CO_3^{2-} substitution for hydroxide and phosphates groups could decrease OH^- directional disorder and stabilize HAp structure [35-40], leading to decrease in the dissolution.

In spite of large body of research exists in this area, solid evidence to demonstrate the effect of additives on the solubility of tricalcium phosphate is still lacking. Careful and systematic analysis of structure of the ion-substituted phosphates is prerequisite for understanding the role played by these elements on the mechanisms of dissolution behavior. In the present research, Si and Zn were chosen as the additives under the consideration for

the dissolution and pharmaceutical effects. The final purpose of this research is to: (1) develop a resorbable and implantable ceramic structure that would act as a bone substitute initially and eventually be resorbebd by the body during the natural process of bone remodeling; (2) control the resorption rate to match the new bone growth rate and maintain the necessary strength by chemical modification of the material.

References

1. Fernandez E. Calcium phosphate bone cements for clinical applications, Part I: solution chemistry. J Mater Sci: Mater in Med 1999;10:169-176.

2. Nancollas GH. In vitro Studies of Calcium Phosphate Crystallization. Germany: VCH, 1982.

3. Christoffersen J. Kinetics of dissolution of calcium hydroxyapatite. Journal of Crystal Growth 1980;49:29-44.

4. Durucan C. Formation of hydroxyapatite by hydrolysis of alpha-tricalcium phosphate: The Pennsylvania State University; 2003.

5. Brown WE, Chow LC. Thermodynamics of apatite crystal growth and dissolution. Journal of Crystal Growth 1981;53(1):31-41.

6. Ducheyne P, Radin S, King L. The effect of calcium phosphate ceramic composition and structure on in vitro behavior. I. Dissolution. Journal of Biomedical Material Research 1993;27:25-34.

7. Klein CPAT, Driessen AA, de Groot K. Relationship between the degradation behaviour of calcium phosphate ceramics and their physical-chemical characteristics and ultrastructural geometry. Biomaterials 1984;5(3):157-160.

8. Vereecke G. Calculation of the solubility diagrams in the system $Ca(OH)_2$-H_3PO_4-KOH-HNO_3-CO_2-H_2O. Journal of Crystal Growth 1990;104:820-832.

9. Manjubala I. preparation of biphasic calcium phosphate doped with magnesium fluoride for osteoporotic applications. J Mater Sci letter 2001;20:1225-1227.

10. Koutsoukos PG. Influence of metal ions on the crystal growth of calcium phosphate. Boston: Kluwer academic publishers, 1998.

11. Langstaff S, Sayer M. Resorble bioceramics based on stabilized calcium phosphates. Part II: evaluation of biological response. Biomaterials 2001;22:135-150.

12. Ito A. Resorbability and solubility of zinc-containing tricalcium phosphate. J Biomed

Mater Res 2002;60:224-231.

13. Ito A. Preparation, solubility, and cytocompatibility of zinc-releasing calcium phosphate ceramics. J Biomed Mater Res. 2000;50:178-183.

14. Gibson IR, Best SM, Bonfield W. Chemical characterization of silicon-substituted hydroxyapatite. J Biomed Mater Res. 1999;44:422-428.

15. Ruys AJ. Silicon-doped hydroxyapatite. Journal of Australian Ceramic Society 1993;29:71-80.

16. Serre CM, Papillard M, Chavassieux P, Voegel JC, Boivin G. Influence of magnesium substitution on a collagen–apatite biomaterial on the production of a calcifying matrix by human osteoblasts. J Biomed Mater Res, 1998;42:626–633.

17. Bigi A, Foresti E, Gregorini R, Ripamonti A, Roveri N, Shah JS. The role of magnesium on the structure of biological apatites. Calcified Tissue International 1992;50(5):439-444.

18. Xie D, Feng D, Chung I-D, Eberhardt AW. A hybrid Zinc-calcium-silicate polyalkenoate bone cement. Biomaterials 2003;24:2794-2757.

19. Mayer I, Cuisinier FJG, Popov I, Schleich Y, Gdalya S, Burghaus O, et al. Phase Relations Between β-Tricalcium Phosphate and Hydroxyapatite with Manganese(II): Structural and Spectroscopic Properties. European Journal of Inorganic Chemistry 2006;7:1460-1465.

20. Ergun C, Webster TJ. Hydroxylapatite with substituted magnesium, zinc, cadmium, and yttrium. I. Structure and microstructure. J Biomed Mater Res 2002;59:305-311.

21. Schroeder LW, Dickensand B, Brown. WE. Crystallographic Studies of the Role of Mg as a Stabilizing Impurity in β-tricalcium phosphate: II. Refinement of Mg-containing β-tricalcium phosphate. J Solid State Chemistry 1977;22:253-262.

22. Bigi A, Falini g, Foresti E, Ripamonti A. Rietveld structure refinement of synthetic magnesium substituted β-tricalcium phosphate. Zeitschrift fur Kristallographie 1996;211:13-16.

23. Okazaki M, LeGeros RZ. Crystallographic and chemical properties of magnesium-containing apatites before and after suspension in solutions. Magnesium Research 1992;5(2):103-108.

24. Termine JD, Posner AS. Calcium phosphate formation in vitro. I. Factors affecting initial phase separation. Arch Biochem Biophys 1970;140:307.

25. Termine JD, Peckauskas RA, Posner AS. Calcium phosphate formation in vitro. II. Effects of environment on amorphous-crystalline transformation. Arch Biochem Biophys

1970;140:318.

26. Ito A. Zinc-releasing calcium phosphate for stimulating bone formation. Materials Science and Engineering C 2002; 22:21-25.

27. Bigi A, Foresti E, Gandolfi M, Gazzano M, Roveri N. Isomorphous substitutions in β-tricalcium phosphate: the different effects of zinc and strontium. Journal of Inorganic Biochemistry 1997;66(4):259-265.

28. Jallot E. Resorption kinetics of four hydroxyapatite-based ceramics by particle induced X-ray emission and neutron activation analysis. Eur Phys J AP 1999;6:205-215.

29. Bigi A. Inhibiting effect of zinc on hydroxylapaite crystallization. Journal of Inorganic Biochemistry 1995;58:49-58.

30. Porter AE, Botelho CM, Lopes MA, Santos JD, Best SM, Bonfield W. Ultrastructural comparison of dissolution and apatite precipitation on hydroxyapatite and silicon-substituted hydroxyapatite in vitro and in vivo. Journal of Biomedical Materials Research, Part A 2004;69A(4):670-679.

31. Porter AE, Patel N, Skepper JN, Best SM, Bonfield W. Comparison of in vivo dissolution processes in hydroxyapatite and silicon-substituted hydroxyapatite bioceramics. Biomaterials 2003;24(25):4609-4620.

32. Botelho CM, Lopes MA, Gibson IR, Best SM, Santos JD. Structural analysis of Si-substituted hydroxyapatite: zeta potential and X-ray photoelectron spectroscopy. Journal of Materials Science: Materials in Medicine 2002;13(12):1123-1127.

33. Thian ES, Huang J, Vickers ME, Best SM, Barber ZH, Bonfield W. Silicon-substituted hydroxyapatite (SiHA): A novel calcium phosphate coating for biomedical applications. Journal of Materials Science 2006;41(3):709-717.

34. Langstaff S, Sayer M. Resorble bioceramics based on stailized calcium phosphates. Part I: rational design, sample preparation and materials characterization. Biomaterials 1999;20:1727-1741.

35. Rehman I, Bonfield W. Characterization of hydroxyapatite and carbonated apatite by photo acoustic FTIR spectroscopy. Journal of Materials Science: Matererials in Medicine 1997;8:1-4.

36. Elliott JC, Holcomband DW. Infrared determination of the degree of substitution of hydroxyl by carbonate ions in human dental enamel. Calcif Tissue Int 1985; 37:372-375.

37. Gineste L. Degradation of Hydroxylapatite, Fluorapatite, and Fluorhydroxyapatite coatings of dental implants in dogs. J Biomed Mater Res 1999;48:224-234.

38. Jha LJ, Best S, Santos JD, Bonfield W. Synthesis and crystallographic

characterization of fluoride-substituted apatites. Bioceramics, Proceedings of the International Symposium on Ceramics in Medicine 1996;9:165-168.

39. Jha LJ, Best SM, Knowles JC, Rehman I, Santos JD, Bonfield W. Preparation and characterization of fluoride-substituted apatites. Journal of Materials Science: Materials in Medicine 1997;8(4):185-191.

40. Elliott JC. Structure and Chemistry of the Apatites and other Calcium Orthophosphates. London: Elsevier, 1994.

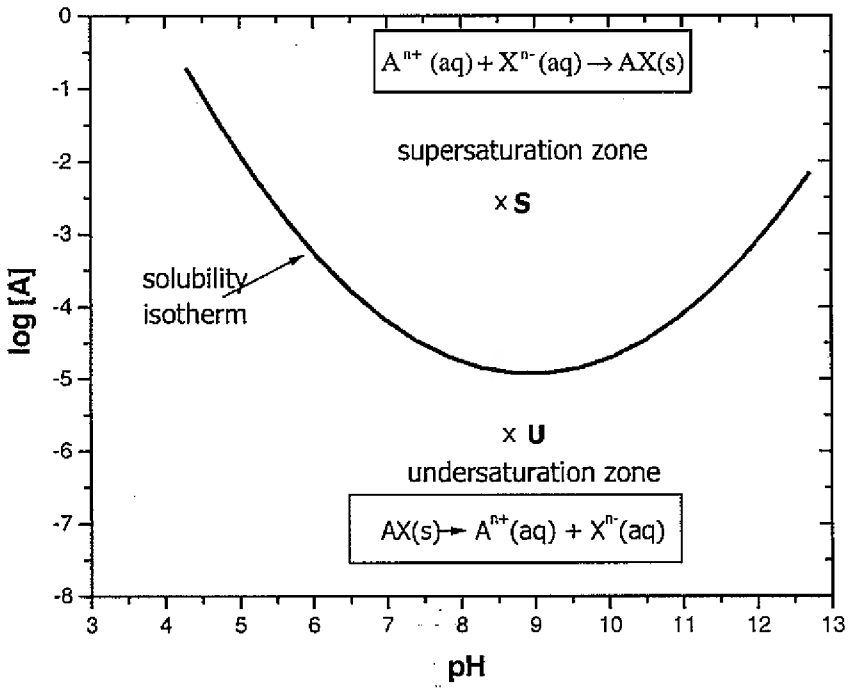

Figure 2.1 Solubility diagram for a general mineral compound AX, in the system of $A(OH)_n - H_nX - H_2O$ [1]

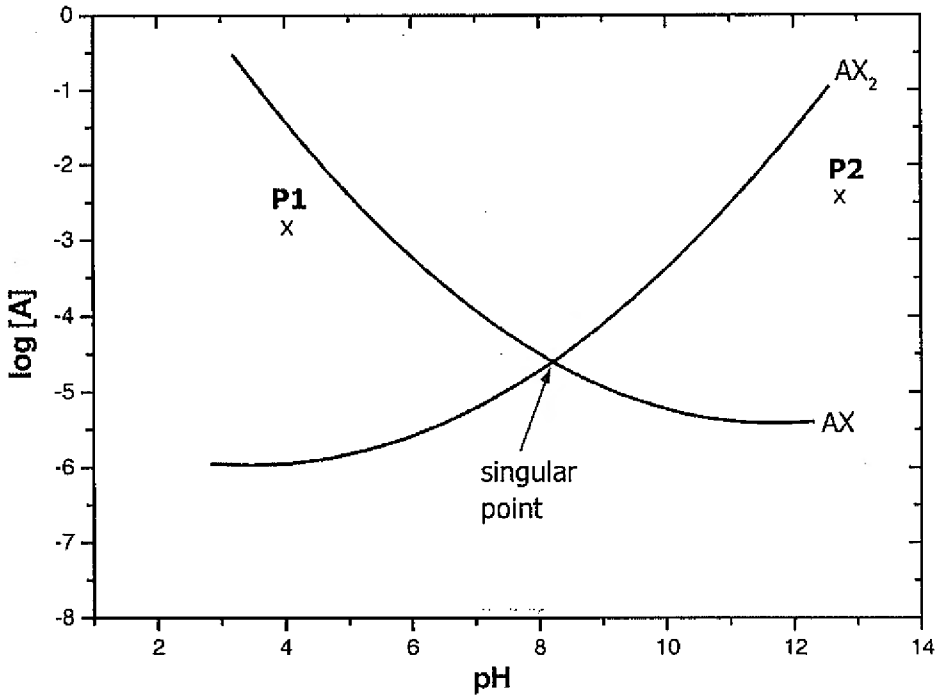

Figure 2.2 Relative positions of isotherms for two hypothetical compounds AX and AX_2 in the system $A(OH)_n - H_nX - H_2O$ [1]

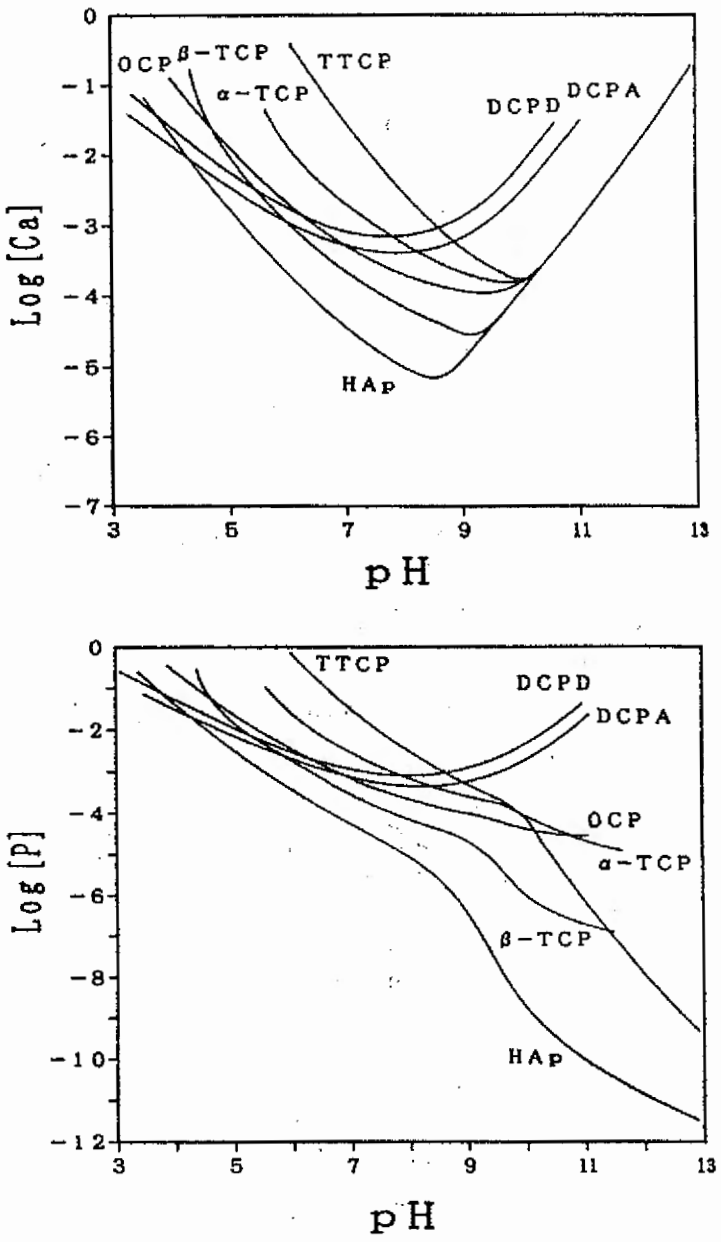

Fig. 2.3 Solubility phase diagram for the ternary $Ca(OH)_2$-H_3PO_4-H_2O system at 25° [5]

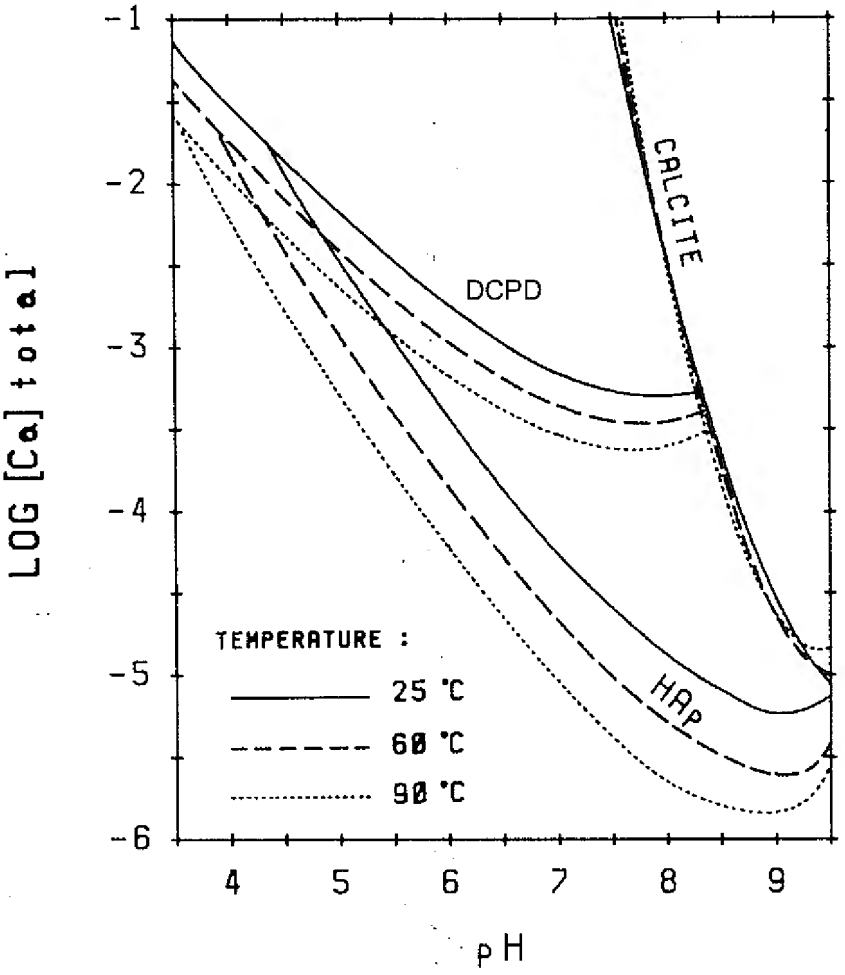

Figure 2.4 Influence of temperature on the solubility isotherms of HAp, DCPD and calcite in the system $Ca(OH)_2 - H_3PO_4 - KOH - HNO_3 - CO_2 - H_2O$ [8]

CHAPTER 3: Si, Zn-MODIFIED TRICALCIUM PHOSPHATES: A PHASE COMPOSITION AND CRYSTAL STRUCTURE STUDY

A Paper published in the *Key Engineering Materials*[1]

Xiang Wei[a] and Mufit Akinc[b]

Department of Materials Science and Engineering and Ames Laboratory, Iowa State University, Ames, IA 50011, U.S.A

[a]xiangwei@iastate.edu, [b]makinc@iastate.edu

Abstract

Tricalcium phosphate modified by silicon and zinc was synthesized as a candidate for resorbable temporal bone implant having a controlled solubility and improved biocompatibility. Since Si and Zn are essential trace elements in human bone, the release of Si and Zn during the resorption process is expected to increase the osteogenic activity for the new bone formation. From XRD and ICP analyses, it was shown that up to 10 mol% Si and Zn can be incorporated in the tricalcium phosphate lattice without formation of a second phase. Changes in lattice parameters and unit volume of TCP as calculated by Rietveld refinement analysis indicate that Si and Zn substitute for P and Ca respectively.

I. Introduction

In the past couple of decades, many efforts in artificial bone engineering have involved the use of synthetically formed HAp. However, the synthetic HAp differs from the natural bone in stoichiometry, crystallinity, and composition, which limits the body's bone cells to remodel. Alternatively, a metastable compound can be implanted, which can convert into a material to mimic natural HAp or is otherwise biocompatible when exposed to the

bone cells to remodel. Alternatively, a metastable compound can be implanted, which can convert into a material to mimic natural HAp or is otherwise biocompatible when exposed to the body environment. β-TCP is the low temperature phase of tricalcium phosphate. Upon heating, it transforms to α at 1125°C[1]. Both of these materials are more soluble and resorbable than stoichiometric HAp and therefore may be incorporated into bone more readily by osteocytes. It is well known that α-TCP can convert to HAp upon aging in aqueous solution, whose composition can be much closer to the natural bone component than synthesized HAp under physiological conditions[2, 3]. However, dissolution rate of α-TCP is higher than bone remodeling rate resulting in loss of strength. An ideal bone implant material would maintain the strength and support the activity of osteoblasts in the development of new bone, while simultaneously being resorbed by osteoclasts as part of the lifelong orderly process of bone remodeling[4]. Therefore, the biphasic material of α and β with controlled dissolution behavior will be a promising resorbable biomaterial for temporary bone substitution.

A number of studies have been carried out to understand the dissolution behavior of HAp. However, study of TCP is limited to a few reports. The purpose of this research is to understand the dissolution behavior of chemically modified tricalcium phosphates. Moreover, the osteoconduction and osteosubstitution can be increased by controlling the biodegradation of the materials. The selection of additives used in this research is not only based on their role in dissolution behavior but also on their pharmaceutical ability to enhance bone formation, or enhance tissue regeneration, which are desirable for a surgical implant. In particular, Si for P and Zn for Ca substitution in limited amounts have been considered. The crystal structure and dissolution behavior of chemically modified calcium phosphates are investigated, which in turn will help explain the stability mechanism.

II. Materials and Method

The commercial reagent grade $CaCO_3$ (Fisher, USA), $NH_4H_2PO_4$ (Fisher, USA), ZnO (Fisher, USA) and fumed SiO_2 (Aldrich, USA) were used as received. All Si,Zn-TCP samples were prepared by reacting the appropriate chemical mixture at 1300°C for 4 hours in air and quenched in dry air. Before sintering, the mixture was milled in anhydrous ethanol for 4 hours using alumina media and the slurry was vacuum filtered

and dried. Samples containing various levels of Si and Zn, were prepared to investigate the role of additives on the thermal stability and crystal structure of Si,Zn-TCP. The molar ratios of (Zn+Ca):(Si+P) kept constant at 1.5 as in stoichiometric TCP, and the maximum Zn and Si substitutions were limited to 10 mol percent of P and Ca (i.e., $Si/(Si+P) = Zn/(Zn+Ca) = 0.1$).

Calcium, phosphorous, silicon and zinc concentrations of the powders were determined by the ICP (Thermo Jarrell-Ash AtomScan16, Thermo Elemental, Franklin, MA). An X-ray powder diffractometer (PAD V, Scintag Inc. CA) with Cu Kα radiation was used for crystal structure analysis and lattice parameter determinations. An accelerating voltage 45kV and a current of 40 mA were used. The XRD data were collected over 2θ range of 10-80° at a step size of 0.02°. The Rietveld analysis of the diffraction patterns with different additive levels was performed by Rietica software. Determination of the lattice parameters with background parameters, zero shift, and peak shape parameters was made by Lebail techniques.

III. Results and Discussion

1. Chemical Composition and Powder Stoichiometry

Table 1 lists the nominal and measured calcium, phosphorus, zinc and silicon contents for synthesized α-TCP and Si,Zn-TCP powders as determined by ICP. The accuracy of analysis was 3% with a reproducibility of 5%. The nominal and measured values are very close and no loss of components occurs during sintering. Measured values of Ca:P and (Zn+Ca):(Si+P) are around 1.5, close that of stoichiometric TCP.

Table 1 ICP analysis of the prepared samples

Samples	Si [wt%]		Zn [wt%]		Ca:P	(Zn+Ca):(Si+P)
	N	M	N	M	M.	M.
α-TCP	0	0.008	0	0.099	1.53	N/A
Si,Zn-2	0.36	0.35	1.25	1.27	1.487	1.457
Si,Zn-10	1.77	1.97	6.15	6.03	1.477	1.433

N=Nominal, M=Measured

Si,Zn-2: TCP modified by the addition of 2 mol% each of Si and Zn.

2. Phase Composition

X-ray diffraction patterns for sintered Si,Zn-TCP are shown in Figure 1. The patterns show an excellent agreement with the published JCPDS files of α-TCP (#29-395), β-TCP(#09-169), or mixture of these two phases depending on the level of additives. No evidence for other crystalline phases, such as $CaSiO_3$ or other phosphates, are observed. It indicates that Zn and Si are dissolved completely in the TCP after sintering for 4h at 1300°C. Figure 1 also compares XRD of Si,Zn-5, Si-5, and Zn-5 samples. Si,Zn-5 shows a mixture of α and β phases, while Zn-5 has only β phase and Si-5 has α as the major phase. Therefore, Zn addition seems to favor β phase structure, which will increase β to α phase transformation temperature; while Si addition favors α structure, which will decrease the transformation temperature. The phase distribution of Si,Zn-TCP samples was calculated by the Rietveld refinement method. The results show that α:β ratio decreases from about 9:1 to 2:3 as the concentration of additives increased from 0.01 to 0.05, which implies that Zn addition dominates the phase composition as doping level increased. From phase diagrams of $Ca_3(PO_4)_2$-Ca_2SiO_4, the solubility limit of Si in TCP is approximately at a molar ratio of 0.04 expressed as $Si/(Si+P)$ [5]. In the Si-5 sample, silicocarnotite appears as the second phase. However, Si,Zn-TCP samples show that up to 0.1 Si and Zn can be incorporated into the tricalcium phosphate lattice without formation of a second phase. Therefore, the solubility of Si increased if Si and Zn were doped together.

3. Crystal Structure

Comparing XRD patterns of Si,Zn-TCP and pure TCP, all peaks of Si,Zn-TCP show slight shift, indicating a change in the lattice parameters imposed by the additives. Table 2 lists the ionic radii for the given co-ordination numbers of elements relevant to this work[6]. The data indicate that the substitution of Zn for Ca will lead to a contraction, while the substitution of Si for P will cause expansion of the structure. The lattice parameters and unit cell volumes for both α- and β-phases are varied with the level

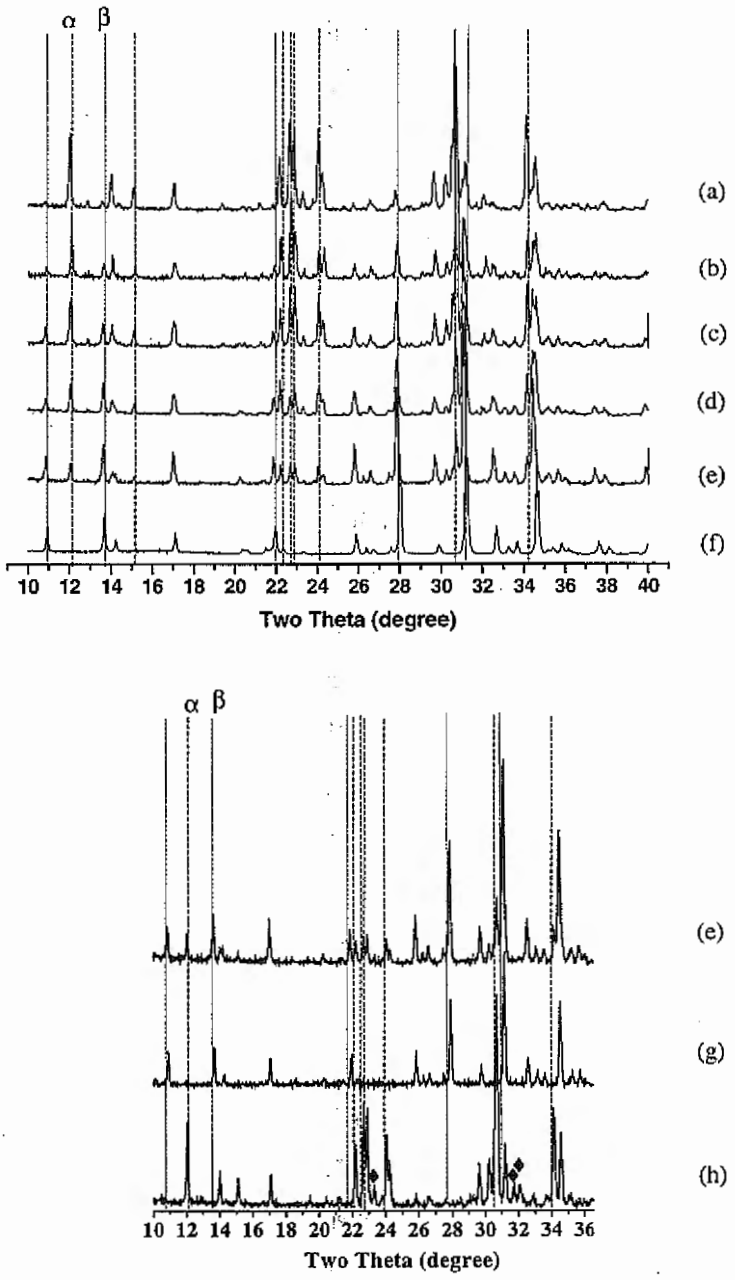

Fig. 1 XRD patterns of Si,Zn-TCP with different doping levels. (a)Si,Zn-1 (b)Si,Zn-2 (c) Si,Zn-3 (d)Si,Zn-4 (e)Si,Zn-5 (f)Si,Zn-10 (g)Zn-5 (h)Si-5. The number 1 to 10 means the addition is at a molar ratio of 0.01 to 0.1 in $Si/(Si+P)$, or $Zn/(Zn+Ca)$, or both. The dotted lines represent the distinct peaks for α-TCP, and the dashed lines are β-TCP. Silicocarnotite phase is represented by ♦.

of Si and Zn added. The profile residual factor Rp in Lebail refinement for all samples is in the range of 0.05 to 0.08. For comparison purpose, Figure 2 shows the unit cell volume of pure and doped TCP. The Zn addition effect on the structure was clearly shown by Zn-TCP samples. The α phase volume of Zn-5 is 10 $Å^3$ smaller than α-TCP (4307.5 $Å^3$ vs 4317.6 $Å^3$). The β phase volumes of Zn-5 and Zn-10 are 3472.8 and 3441.5 $Å^3$, compared with 3527.3 $Å^3$ of β-TCP, again showing a substantial contraction of unit cell volume with the addition of Zn. The volume of Si-5 is 4351.7 $Å^3$, much larger than that of α-TCP, indicating that Si expands the structure. As expected, Si,Zn-TCP samples showed competitive effect of Si and Zn: the α phase volumes of Si,Zn-TCP samples are larger than that of the pure α-TCP, but decrease at higher doping level; the β phase volumes of Si,Zn-TCP are smaller than pure β-TCP, even though they are larger than Zn-TCP. Therefore, zinc content has the dominant effect on the β phase, and silicon has a dominant effect on the α phase. As the level of doping increases, Zn dominates the structural changes brought by the additives. These data are also consistent with the phase stability study.

Table 2 Ionic Radii of Relevant Ions Employed

Ion	Ca^{2+}	Zn^{2+}	P^{5+}	Si^{4+}
Coordination Number	6	6	4	4
Ionic Radius [Å]	1.00	0.74	0.17	0.26

In β-TCP unit cell, Ca(4) and Ca(5) sites are unique compared to other three sites. Ca(4) has an unusual coordination to the O(9), O(9'), O(9'') face of the $P(1)O_4$ group and the Ca(4)···O(9) bonds are longer (3.041(1) Å) than normal Ca···O bond in accord with the Pauling's rule[7]. The Ca(5) site have six-fold octahedral coordination surrounded by oxygens, and all six Ca···O distances are relatively short, falling into the range 2.238-2.287Å. The normal value is ~2.4Å[7]. Therefore, these two sites are very suitable for the smaller cation, but are highly constrained for a Ca^{2+} ion. Substitution of smaller Zn^{2+} for Ca^{2+} results in more stable TCP structure by reducing the strain in the structure. Similarly, tetrahedral PO_4^{3-} ions in the TCP structure may be replaced by SiO_4^{4-} units, resulting in Si substituted TCP. According to the structure, each formula unit occupies

180 $Å^3$ in α-TCP compared with 168 $Å^3$ in the β form[1]. Since α-TCP has a more open structure than β-TCP, the larger Si^{4+} ions favor α over β phase.

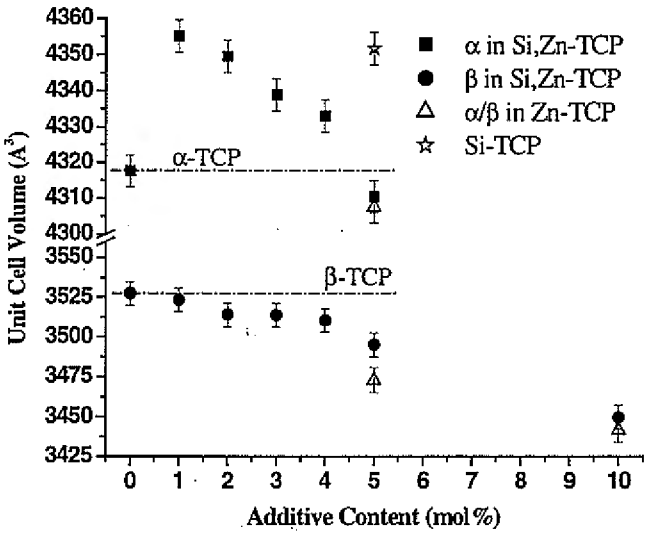

Fig. 2 Unit cell volume of Si,Zn-TCP determined by Lebail refinement. The error bar shows the standard deviation of one sample which has been duplicated three times.

Conclusion

Si,Zn-modified TCP exhibits α-, β-TCP structure, or mixture of the two depending on the level of the additives. The changes in lattice parameters and unit cell volume clearly demonstrate that Si and Zn are structurally incorporated into TCP and stabilize the structure. Zn can substitute for the Ca and Si can substitute for the P. It was shown that Zn, a smaller ion than Ca, causes a contraction of the unit cell, while Si larger than P results in expansion of the unit cell. Effect of these additives on the resorption characteristics of TCP is currently being investigated.

References

1. J.C.Elliott. Structure and Chemicstry of the Apatites and other Calcium Orthophosphates. London: Elsevier, 1994.

2. Durucan C, Brown PW. α-Tricalcium phosphate hydrolysis to hydroxyapatite at the near physiological temperature. Journal of Materials Science: Materials in Medicine 2000;11:365-371.

3. Park JB, Lakes RS. Biomaterials: An Introduction 2nd ed. New York: Plenum Publishing, 1992.

4. Langstaff S, Sayer M. Resorble bioceramics based on stabilized calcium phosphates. Part II: evaluation of biological response. Biomaterials 2001;22:135-150.

5. Nurse RW, Welch JH, Gutt W. High-temperature phase equilibria in the system dicalcium silicate-tricalcium phosphate. Journal of the chemical society 1959:1077-1083.

6. Lide DR. CRC Handbook of Chemistry and Physics 84th edition. Boca Roton: CRC Press LLC, 2003.

7. Dickens B, Schroeder LW, Brown WE. Crystallographic Studies of the Role of Mg as a Stabilizing Impurity in β-tricalcium phosphate: I. The Crystal Structure of Pure β-tricalcium phosphate. J Solid state Chemistry 1974;10:232-248.

CHAPTER 4:

CRYSTAL STRUCTURE ANALYSIS OF Si, Zn-MODIFIED TRICALCIUM PHOSPHATE BY NEUTRON POWDER DIFFRACTION

A manuscript to be submitted to *Biomaterials*

Xiang Wei and Mufit Akinc*

Department of Materials Science and Engineering and Ames Laboratory, Iowa State University, Ames, IA 50011, USA.

*Email: makinc@iastate.edu

Abstract

Tricalcium phosphate (TCP) is a candidate for the temporary bone implant. Attempts were made to tune the resorption rate of implant for bone reforming by doping different level of Si and Zn. In this paper, the crystal structure of Si,Zn-modified tricalcium phosphate (Si,Zn-$Ca_3(PO_4)_2$, Si,Zn-TCP) was studied by using a time-of-flight (TOF) neutron powder diffraction and the Rietveld analysis method. Si,Zn-TCP was confirmed to have a rhombohedral structure (space group R3c, Z = 21), with the unit cell parameters a = b =10.3958(1) Å, c = 37.3122(7) Å, $\alpha = \beta = 90°$, and $\gamma = 120°$ in the hexagonal setting. Of the five cation sites, Ca(1), Ca(2), and Ca(3) positions are still occupied by Ca with minor change in Ca-O bond distance compared to the pure β-TCP. Whereas, Ca(5) site was totally occupied by Zn. Compared with the original Ca(5)···O distance, the shorter and more uniform Zn(5)···O bond distances show the smaller cation substitution effect and a more ideal octahedral geometry. The site Ca(4) was partially substituted by Zn and Ca,Zn(4)···O(9) bond distance is 2.808(5) Å, much shorter than the original 3.041(1). According to the occupancy, multiplicity and total cation sites, the Zn substitution content is calculated to be 10.01% of total Ca sites. A fraction of Si substitutes for P(1) sites and the substitution content is calculated to be 3.86% of total phosphor sites.

I. Introduction

Among the calcium phosphate ceramics, tricalcium phosphate ($Ca_3(PO_4)_2$, TCP) has been investigated most extensively as the primary resorbable bioceramics for bone replacement [1-3]. TCP was reported to be more bioresorbable than HAp, which usually shows minimal resorption. Due to the high solubility, TCP is expected to degrade in the host and be gradually replaced by the regenerating bone, meanwhile it acts as a seed for the new bone and a supplier of the Ca and PO_4 ions. However, higher solubility of TCP results in a reduction of the bone-implant strength. Thus, the suitability of TCP for use in vivo is critically dependent on how the dissolution behavior might be controlled by chemical modification. A possible approach is to dope TCP with small amount of trace elements. Ions with the similar size and charge are capable to substitute Ca^{2+} and PO_4^{3-} sites and to incorporate into the TCP. This can lead to a change in the crystal structure, composition, morphology, and even the porosity, which are the principal factors determining the stability and solubility of calcium phosphates.

The influence of trace elements on crystallization and dissolution has been the subject of numerous studies [4-14]. As reported by others previously, the addition of magnesium to TCP produced β-whitlockite ceramic and reduced the dissolution rate of the TCP [4,11,12,15]. Further investigation suggested that Mg might substitute Ca sites and stabilize TCP structure [16,17], which also effectively suppresses the phase transition from β- to α-TCP, which is the high temperature phase. Similar to Mg, zinc (Zn) and cadmium (Cd) were also proposed to increase the phase transformation temperature and stabilize β-TCP structure[8,18,19]. IR spectra showed a increase in degeneracy of the PO_4^{3-} modes with increasing Cd content, indicating the distortion of PO_4^{3-} from the ideal tetrahedral geometry [19]. The solubility of sintered Zn-TCP decreased steeply with an increase in zinc content, and it decreased to a level of the equilibrium solubility of pure HAp when the zinc content was raised to 3.70wt% [7,8,18,20]. Due to its important role in biomineralization process, silicon has also been investigated extensively as additives for calcium phosphates. Ionic radii considerations suggested that the most likely substitution site for Si was that of phosphorus. Reid, Sayer and Langstaff reported silicon could incorporate into α-TCP structure, causing a linear enlargement of the unit cell, in agreement with its greater ionic radius compared to that of

phosphor (see Table 1) [21-23]. According to Yin's calculation, two SiO_4^{4-} could substitute for a pair of PO_4^{3-} groups with an excess Ca^{2+} for charge compensation, leading to a stable structure [24].

In our research, silicon and zinc were added in a small quantity to modify the dissolution behavior of TCP. Meanwhile, these two elements could increase osteoconductivity of the implant materials and stimulate osteogenesis for new bone growth [25-27]. The previous X-ray diffraction results showed that TCP doped with 10mol% Si and Zn at high temperature is composed of β-TCP, the low temperature phase of TCP. No secondary or amorphous phase was observed in the X-ray diffraction pattern, which indicates that Zn and Si are incorporated into the TCP structure after high temperature sintering. The dissolution study also confirmed that the Zn,Si-doped TCP is stabilized in the simulated body fluid compared with the pure TCP [28].

Our previous XRD data analysis for lattice parameters and unit-cell volume showed the effect of Zn and Si on the crystal structure [29]. However, the exact site substitution of Si and Zn in the TCP phase is still unclear due to the low angular resolution of XRD and the small difference in scattering factors of Si^{4+} and P^{5+}. Therefore, the crystal structure of Si,Zn-TCP is further investigated in this paper by using high resolution powder neutron diffraction and the Rietveld method.

II. Materials and Methods

The chemical reagent grade $CaCO_3$, $NH_4H_2PO_4$, ZnO (Fisherscientific, Hampton, NH) and fumed SiO_2 (Sigma-Aldrich, St. Louis, MO) were used as received. TCP was synthesized by reacting the appropriate chemical mixture according to the following equation.

$$3CaCO_3 + 2NH_4H_2PO_4 \rightarrow Ca_3(PO_4)_2 + 3CO_2 + 2NH_3 + 3H_2O$$

10 atom% of ZnO and SiO_2 were mixed with the above chemicals, which means the Zn and Si substitutions were 10% of Ca and P sites (i.e., $Si/(Si+P) = Zn/(Zn+Ca) = 0.1$). Then, the resulting formula is $Ca_{2.7}Zn_{0.3}(P_{0.9}Si_{0.1}O_4)_2$ and the molar ratio of (Zn+Ca):(Si+P) kept constant at 1.5 as in the stoichiometric TCP. The mixture was milled in anhydrous ethanol for 4 hours by using alumina media. The slurry was vacuum filtered and dried. Thereafter, the

powder was sintered at 1300°C for 10 hours in air, followed by quenching in dry air.

A time-of-flight (TOF) neutron powder diffraction experiment was carried out with a General Purpose Powder Diffractometer, GPPD [30], installed in Argonne National Laboratory's Intense Pulsed Neutron Source division (IPNS). The powdered sample was contained in a cylindrical vanadium cell with rubber compression seal: 1.11 cm in diameter, 5.715 cm in height and the total volume 5.53 cm^3. Multiple detector banks are centered at 2θ values of ±145°, ±125°, ±90° and +53°, which provide measurement of anisotropy in any of a variety of structural parameters such as scattering intensity (texture) and lattice parameter (anisotropic strain). The unit-cell and structural parameters of Si,Zn-TCP were refined by using the general structure analysis system *(GSAS)*, a Rietveld profile-analysis code developed by Larson & Von Dreele (2001) [31]. During the refinement, multiple banks were combined in consideration of small-d-spacing data effect on the temperature factors accuracy and lager-d-spacing data effect on the lattice parameter accuracy. For histograms 1 (taken from the 145° 2θ detector bank), a d-spacing range of 0.68 to 2.431 Å was used; for histogram 2 (from the 90° 2θ detector bank), a range of 1 to 3.176 Å was used; for historgram 3 (from the 53° 2θ detector bank), a range of 1.5 to 4.575 Å was used. The background function is the fourth function with 6 terms. The TOF profile function 3 is used to include the generally Lorentzian broadening exhibited by most samples. It is a convolution of the back-to-back exponentials with a pseudo-Voigt function to model both the Gaussian instrumental component and the anisotropic Lorentzian component due to the sample. Six parameters in this profile are refined, including pulse-shape parameters β_0 and β_1, Gaussian broadening coefficients σ_1 and σ_2 (σ_0 was set equal to zero), and particle size coefficients γ_2 and γ_{2e}. Isotropic thermal parameters were refined for all atoms and the site occupancy parameters were refined for Ca(4), Ca(5) and P(1) sites, which were substituted by Zn and Si atoms.

III. Data Analysis and Results

TCP has three polymorphs: α, β, and γ, depending on the temperature [32]. As reported by Dickens et al.[33], the β-TCP crystallizes in the rhombohedral space group R3c with unit-cell parameters a=10.439(1) Å, c=37.375(6) Å. According to the previous phase

study for Si,Zn-TCP [34], Rietveld refinement of neutron powder diffraction data were done by assuming that Si,Zn-TCP has R3c space group as β-TCP. The unit-cell and structural parameters of pure β-TCP were also used as the initial values for Si,Zn-TCP in the preliminary refinement.

In the first preliminary analysis, the pure β-TCP structure was refined without Si and Zn substitution. The occupancy factors (F) for Ca, P and oxygen sites were fixed to be unity except Ca(4) 0.491(8), whereas the isotropic thermal parameters (B) were refined independently. The initial value was 1 $Å^2$, the typical value for inorganic ionic crystals and many coordination compounds. All the thermal parameters were assumed to be isotropic due to the difficulty of the convergence in the refinements with anisotropic thermal parameters. The refinement result shows that the thermal parameters for Ca(4), Ca(5) and P(1) are negative. In the simplest form of the atom oscillatory motions, temperature factor of the j^{th} atom is represented as [35]:

$$t^j = \exp\left\{-B^j \frac{\sin^2\theta}{\lambda^2}\right\}$$

The isotropic thermal parameter B is expressed as:

$$B^j = 8\pi^2(\bar{u}^2)^j$$

where $(\bar{u}^2)^j$ is the root mean square deviation of the j^{th} atom from its equilibrium position (x, y, z) in $Å^2$. Therefore, the isotropic thermal parameters are only physical when they are positive.

In the secondary refinement, the occupancy factors for Ca(4), Ca(5) and P(1) were refined, while the thermal parameters were fixed at 1 $Å^2$. The results showed that F(Ca(4))>0.491, F(Ca(5))>1 and F(P(1))<1, which indicate that two Ca sites are occupied with the element that has more electrons than Ca and P(1) sites are occupied with the element that has less electrons. Considering Si,Zn-TCP composition, Ca(4) and Ca(5) sites are possibly substituted by Zn and P(1) sites are substituted by Si.

In the final analysis, Zn were added to Ca(4) and Ca(5) sites, and Si was added to P(1) sites. Constrains were setup for atomic coordinates, isotropic thermal parameters and occupancy factor (Table 2). According to Schroeder's study on Mg-substituted TCP [16], Mg

will fill Ca(5) sites first until the theoretical maximum of 9.52% for this site is reached. And then, Ca(4) sites will be filled. In our study, the level of Zn substitution is about 10% of total Ca sites. Therefore, Ca(5) sites will be fully occupied by Zn and the remaining 0.48% Zn will substitute for Ca(4) sites. The result of the final refinement is shown in Tables 2 and 3. Table 4 and 5 shows selected bond lengths, coordination number (CN) of cations, bond angle variance, and PO_4 group geometry calculated from the refined crystal parameters. Figure 1 to 3 show the Rietveld pattern of neutron powder diffraction data at 2θ 145°, 90° and 53°. The final refinement used 11819 data points and 1418 reflections for histrogram 1, 454 reflections for histogram 2 and 138 for histogram 3. The final χ^2 (offset/sig) is 5.426 for 64 variables and other statistics data are shown in Table 2. The error analysis was run to examine the final refinement results. In Figure 4, the normal probability plot for histogram 3 gave a nearly straight line, indicating that the $I_o - I_c$ values are for the most part normally distributed. The slop and intercept of the normal probability plot are 1.7466 and 0.0053. The slope is close to 1 indicating a good fit in the refinement, and the nearly zero intercept indicates that the normal distribution is properly centered about zero. For the histograms 1 and 2, the slope and intercept of the normal probability plot are 2.476 and 0.0227, and 2.2543 and 0.0613 respectively due to the complex background at small d-spacing.

The polycrystalline Si,Zn-TCP was confirmed to have a rhombohedral structure with unit-cell parameters $a = b$ =10.3948(1) Å, c = 37.3079(7) Å, $\alpha = \beta = 90°$, and $\gamma = 120°$ in the hexagonal setting (space group R3c, Z = 21). According to the occupancy parameters, multiplicity and the total atom sites, the Zn and Si content were calculated. The multiplicity of Ca(4) and Ca(5) sites is 6 and there are 63 cation sites in the hexagonal unit cell. The occupancy of Zn for these two sites is 1 and 0.05(6). Thus, the Zn content in the unit cell is 10.01% for all Ca sites, which is very close to the designed composition and chemical analysis result [34]. The multiplicity of P(1) sites is 6 and there are 42 P sites in the hexagonal unit cell. The occupancy of Si is 0.27(6), so the total Si content in the unit cell is 3.86% for all P sites, which is less than the designed composition and chemical analysis result. The other 6.14% Si might form calcium silicate phase. Preliminary solid state NMR results indicate that this Si-rich phase forms nano-scale clusters of approximately 2 nm in diameter [36], which may be accounted for the poor background fitting at small d-spacing.

After refinement, all thermal parameters are positive and the statistical data are much better than those without substitution.

IV. Discussion

1. Two Columns Structure

The Rietveld analysis shows that 10% Si and Zn doped TCP still maintain the basic crystal structure of the pure β-TCP. The structure can be described as two kinds of columns of A and B types, arranging in the hexagonal unit cell along the c-axis (Figure 5) [37]. In a unit cell, there are three A and nine B columns. The A column has the form of ···$P(1)O_4$ Ca(4) Ca(5) $P(1)O_4$··· , while the B column ···$P(3)O_4$ Ca(1) Ca(3) Ca(2) $P(2)O_4$ $P(3)O_4$···. Each A column is surrounded by six B columns, while each B column by two A and four B columns (Fig.5a). In the A column, all the x and y atomic coordinates of Ca(4), Ca(5), and P(1) have the value of zero, indicating that these atoms are located on a straight line along the *c*-axis (as shown in Fig. 5b). There are no sharing oxygen atoms among $P(1)O_4$, $Ca(4)O_3$, and $Ca(5)O_6$ groups, and only one Ca^{2+} ion per pair of Ca(4) sites in a column to maintain the charge balance. In the B column, the x and y atomic coordinates of Ca(1), Ca(2), Ca(3), P(2), and P(3) have different values from each other (Fig. 5c), and three Ca cations are coordinated to seven or eight oxygens, including sharing PO_4 edges or apexes. CaOn (n=coordination number, i.e. 3, 6, 7 or 8) groups are also linked to each other by sharing edges in the column B.

2. CaO_6 and ZnO_6 Polyhedral

Maintaining the same structure as β-TCP, Si,Zn–TCP have five crystallographic sites for cations Ca(1) to Ca(4), Zn(4) and Zn(5). The CN for the Ca and Zn site are: Ca(1)=7, Ca(2)=6 or 8, Ca(3)=8, Ca,Zn(4)=3, and Zn(5)=6.

In the pure β-TCP, Ca (4) is on the 3-fold axis and the coordination is completed by three O(1) atoms from surrounding $P(2)O_4$ groups. The occupancy of Ca(4) is only 0.491(8). This cation site has an unusual coordination to the O(9), O(9'), O(9'') face of the $P(1)O_4$ group. The Ca(4)···O(9) bonds are 3.041(1) Å, longer than the normal Ca···O bond of 2.4 Å. Therefore, Ca(4) is slightly disordered along *c*, weakly bonded and forms deficiency, which

suggests that this site is easily substituted by the impurity ions [16,37]. In Si,Zn-TCP, Ca(4) site was partially substituted by Zn at the coordinates [0, 0, -0.0754(3)]. The occupancy of Zn(4) is 0.05(6) of the total 0.491 for this site. The Ca,Zn(4)···O(9) bond length is 2.775(10) Å, much shorter than the original 3.041(1) Å in the pure β-TCP. The isotropic thermal parameters of this site also decrease to 0.12(30) $Å^2$, compared with 2.0(8) $Å^2$ in the pure β-TCP as reported by Yashima [38]. The decrease of the bond distance and isotropic thermal parameters indicate that the stronger Ca,Zn(4)···O bonds are formed and the structure disorder is minimized.

In β-TCP, the Ca(5) site is also located on the threefold axis. The coordination is essentially octahedral with no shared PO_4 edges. The Ca(5)···O distances are relatively short in the range 2.238-2.287Å, suggesting overbonding in the $Ca(5)O_6$ polyhedron [16]. Thus, this site is constrained for Ca^{2+} ions, but favors the incorporation of the smaller cations requiring a coordination number of six. In Si,Zn-TCP, Ca(5) is totally substituted by Zn at the coordinates [0, 0, -0.2643(1)]. Compared with the Ca(5)···O bond length, the Zn(5)···O distance (2.175(4)-2.185(5)Å) is shorter and more nearly equal. These distances agree well with reported Zn···O values [39]. The O(4)···Ca(5)···O(4) and O(7)···Ca(5)···O(7) angels are 82.7(1)° and 77.1(1)° in β-TCP. The O(4)···Zn(5)···O(4) and O(7)···Zn(5)···O(7) angles are much similar and close to 90°, providing further confirmation of a more ideal octahedral configuration. Therefore, substitution of smaller Zn^{2+} for Ca^{2+} results in a more stable TCP structure by reducing the strain in the structure.

3. PO_4 and SiO_4 Polyhedral

In the pure β-TCP structure, phosphorus atoms are located at three crystallographic sites of P(1), P(2), and P(3). All P atoms are four-fold coordinated with oxygen atoms (n = 4). Given the similar tetrahedral structure of PO_4^{3-} and SiO_4^{4-}, the P in the TCP structure may be replaced by Si. Since P(1) is in the same column A with Ca(4) and Ca(5), the substitution of Ca(4) and Ca(5) by the smaller Zn will leave more open space for larger Si to substitute P(1) site. Dickens's study also showed the positional disorder of $P(1)O_4$ which is likely correlated with the occupancy of the Ca(4) site [33].

After refinement, Si substitutes P(1) sites at [0, 0, 0] and the substitution amount is 3.86mol% of total P sites. The P,Si(1)···O(9) bond distance is 1.534(2) Å, close to P(1)···O(9) (1.536(5) Å) in pure β-TCP. On the contrary, the bond length of P,Si(1)···O(10) is 0.089 Å larger than P(1)···O(10) distance (1.498(12) Å), showing the larger Si substitution effect along *c* axis. The average of O(9)···P,Si(1)···O(9') and O(9)···Si,P(1)···O(10) bond angle is 109.43°, close to the ideal bond angle 109.5° in the tetrahedral structure. Si substitution has a negligible effect on the P(2) and P(3) polyhedral group. The bond length and angles for P(2)···O and P(3)···O sites vary slightly, and the average bond angles are 109.47° and 109.46° respectively.

The refinement shows that Si substitutes for P sites 27% in column A and 3.86% of total P sites in the unit cell, which is much lower than the designed 10% composition. In the histogram 3, a small region from d-spacing 3.85 to 3.95 Å was excluded since there is a small and broad peak that cannot be identified. The solid state NMR is used to analyze the Si environment in Si,Zn-TCP structure. The preliminary results show that the part of Si forms Si-rich nano-sized clusters with a diameter of approximate 7 nm, which can explain the remaining 6.14% Si location [36]. NMR study indicates that Si Q_0 sites accounts for about 20% of the total Si content (10%) in Si,Zn-TCP, which means that about 2% Si forms SiO_4^{2-} and substitutes P sites, in reasonable agreement with the neutron diffraction analysis result.

4. Theoretical Bond Length and Si/Zn Substitution Effect on other Polyhedral Group

The bond distance in Si,Zn-TCP was also compared with the value calculated from the ionic radius (Figure 6). The ionic radii used for Ca^{2+} were r(CN=6) = 1.00 Å, r(CN=7) = 1.06 Å, and r(CN=8) = 1.12 Å; the ionic radii used for Zn^{2+} was 0.74 Å with CN=6; and for O^{2-} was1.38 Å with CN=4 [40].

The calculated Ca···O and Zn···O bond length increased linearly with increase in CN of Ca and Zn. The Ca···O distances at Ca(1), Ca(2), and Ca(3) sites obtained in the Rietveld analysis agreed well with the calculated values. In pure β-TCP, Ca(2) is coordinated strongly to six oxygens and less strongly to two others, O(5) and O(6), of the shared $P(3)O_4$ edges. With Si and Zn addition, the bond distances of Ca(2)···O(5) and Ca(2)···O(6) decreased by

0.075 and 0.045 Å respectively, which indicated the thermal parameters of Ca(2) in Si,Zn-TCP are more isotropic than undoped one. Compared to β-TCP [38], Ca(3) in Si,Zn-TCP has larger thermal parameters due to the coordinated oxygens which correspond to the large thermal displacements (e.g. O(10) 3.69 $Å^2$; O(1) 1.77 $Å^2$; O(9) 1.61 $Å^2$). The larger displacements of O(10) and O(9) are due to the Si substitution for P at P(1) site, while the large displacement of O(1) is due to the Ca(4) partial occupancy and Zn substitution. This suggests that the effect of the Zn(4) and Si(1) substitution is transmitted through several neighbor-neighbor interactions. The refined Ca,Zn(4)···O distance was smaller than Ca(4)···O, but still larger than the calculated value, indicating the smaller Zn^{2+} substitution and the partial occupancy effect on this site. The Ca(5)···O distance in β-TCP is much smaller than the calculated value, suggesting a polyhedral distortion effect [40]. Brown and Shannon reported that this octahedral sites containing Mg^{2+}, Zn^{2+}, Co^{2+} and Li^{+} are generally less distorted than those of V^{5+}, Cu^{2+}, Ca^{2+} and Mn^{3+} and show a less pronounced dependence on mean bond length [41]. The refined Zn(5)···O distance was close to the calculated value of Zn···O, indicating a more ideal octahedral configuration than $Ca(5)O_6$ does.

V. Conclusion

The crystal structure of Si,Zn-modified tricalcium was studied by the time-of-flight (TOF) neutron powder diffraction and the Rietveld method. This material was confirmed to have a rhombohedral structure (space group R3c, Z = 21), with the unit cell parameters a = b =10.3958(1) Å, c = 37.3122(7) Å, $\alpha = \beta = 90°$, and $\gamma = 120°$ in the hexagonal setting. Ca(1), Ca(2), and Ca(3) are still occupied by Ca atom, coordinated with seven, eight, and eight oxygen atoms, respectively. Their coordinates and bond distance with oxygen show minor change compared with pure β-TCP. The site Ca(4) was partially substituted by Zn at the coordinates [0, 0, -0.076(3)]. The Ca,Zn(4)···O(9) bond distance is 2.808(5) Å, much shorter than the original 3.041(1) Å. Ca(5) was totally substituted by Zn at the coordinates [0, 0, -0.2643(1)]. Zn(5)…O bond distance decreases about 0.1 Å compared to Ca(5)…O distance, showing the smaller cation effect. This value is also close to the theoretical calculated one per the ionic radii, suggesting a more ideal octahedral configuration to eliminate the distortion and stabilize the crystal. The total Zn substitution amount is 10.01% of total Ca

sites. Si partially substitutes P(1) sites at [0, 0, 0] and the substitution amount is 3.86% of total P sites, presumably, the remaining Si forms amorphous nano-clusters of Si-rich phase.

Acknowledgments

This work has benefited from the use of the Intense Pulsed Neutron Source at Argonne National Laboratory, which is funded by the US Department of Energy, BES-Materials Science, under Contract No. W-31-109-ENG-38. The authors would like to thank Dr. James W. Richardson and Dr. Evan Maxey for neutron diffraction experiment and discussion on Rietveld refinement. Ames Laboratory is operated for the U.S. DOE by ISU under contract No. W-7405-ENG-82.

References

1. LeGeros RZ, LeGeros JP, Daculsi G, Kijkowaka R. Encyclopedic Handbook of Biomaterials and Bioengineering. New York: Marcel Deker, 1995.

2. Klein CPAT, Driessen AA, de Groot K. Relationship between the degradation behaviour of calcium phosphate ceramics and their physical-chemical characteristics and ultrastructural geometry. Biomaterials 1984;5(3):157-160.

3. Park JB, Lakes RS. Biomaterials: An Introduction 2nd ed. New York: Plenum Publishing, 1992.

4. Manjubala I. preparation of biphasic calcium phosphate doped with magnesium fluoride for osteoporotic applications. J Mater Sci letter 2001;20:1225-1227.

5. Koutsoukos PG. Influence of metal ions on the crystal growth of calcium phosphate. Boston: Kluwer academic publishers, 1998.

6. Langstaff S, Sayer M. Resorble bioceramics based on stabilized calcium phosphates. Part II: evaluation of biological response. Biomaterials 2001;22:135-150.

7. Ito A. Resorbability and solubility of zinc-containing tricalcium phosphate. J Biomed Mater Res. 2002;60:224-231.

8. Ito A. Preparation, solubility, and cytocompatibility of zinc-releasing calcium phosphate ceramics. J Biomed Mater Res. 2000;50:178-183.

9. Gibson IR, Best SM, Bonfield W. Chemical characterization of silicon-substituted hydroxyapatite. J biomed Mater Res. 1999;44:422-428.

10. Ruys AJ. Silicon-doped hydroxyapatite. Journal of Australian Ceramic Society

1993;29:71-80.

11. Serre CM, Papillard M, Chavassieux P, Voegel JC, Boivin G. Influence of magnesium substitution on a collagen–apatite biomaterial on the production of a calcifying matrix by human osteoblasts. J Biomed Mater Res, 1998;42:626–633.

12. Bigi A, Foresti E, Gregorini R, Ripamonti A, Roveri N, Shah JS. The role of magnesium on the structure of biological apatites. Calcified Tissue International 1992;50(5):439-444.

13. Xie D, Feng D, Chung I-D, Eberhardt AW. A hybrid Zinc-calcium-silicate polyalkenoate bone cement. Biomaterials 2003;24:2794-2757.

14. Mayer I, Cuisinier FJG, Popov I, Schleich Y, Gdalya S, Burghaus O, et al. Phase Relations Between β-Tricalcium Phosphate and Hydroxyapatite with Manganese(II): Structural and Spectroscopic Properties. European Journal of Inorganic Chemistry 2006;7:1460-1465.

15. Ergun C, Webster TJ. Hydroxylapatite with substituted magnesium, zinc, cadmium, and yttrium. I. Structure and microstructure. J Biomed Mater Res. 2002;59:305-311.

16. Schroeder LW, Dickensand B, Brown. WE. Crystallographic Studies of the Role of Mg as a Stabilizing Impurity in β-tricalcium phosphate: II. Refinement of Mg-containing β-tricalcium phosphate. J Solid State Chemistry 1977;22:253-262.

17. Bigi A, Falini g, Foresti E, Ripamonti A. Rietveld structure refinement of synthetic magnesium substituted β-tricalcium phosphate. Zeitschrift fur Kristallographie 1996;211:13-16.

18. Bigi A, Foresti E, Gandolfi M, Gazzano M, Roveri N. Isomorphous substitutions in β-tricalcium phosphate: the different effects of zinc and strontium. Journal of Inorganic Biochemistry 1997;66(4):259-265.

19. Bigi A, Foresti E, Gazzano M, Ripamont A, Roveri N. Cadmium-substituted tricalcium phosphate and crystal structure refinement of β'-tricadmium phosphate. Journal of Chemical Research, Synopses 1986(5):170-171.

20. Ito A. Zinc-releasing calcium phosphate for stimulating bone formation. Materials Science and Engineering C 2002; 22:21-25.

21. Sayer M, Stratilatov AD, Reid J, Calderin L, Stott MJ, Yin X, et al. Structure and composition of silicon-stabilized tricalcium phosphate. Biomaterials 2003;24:369–382.

22. Reid JW, Tuck L, Sayer M, Fargo K, Hendry JA. Synthesis and characterization of single-phase silicon-substituted α-tricalcium phosphate. Biomaterials 2006;27(15):2916-2925.

23. Langstaff S, Sayer M. Resorble bioceramics based on stailized calcium phosphates. Part I: rational design, sample preparation and materials characterization. Biomaterials 1999;20:1727-1741.

24. Yin X, Stott MJ. Theoretical insights into bone grafting silicon-stabilized α-tricalcium phosphate. Journal of Chemical Physics 2005;122(2):024709.

25. Carlisle EM. Silicon: a requirement in bone formation independent of vitamin D. Calcif Tissue Int 1981;33(1):27-34.

26. Yamaguchi M, Oishi. H. Stimulatory effect of zinc on bone formation in tissue culture. Biochem Pharmacol 1987;36:4007-4012.

27. Yamaguchi M, Oishi H. Zinc stimulation of bone protein synthesis in tissue culture. Biochem Pharmacol. 1988;37:4075-4080.

28. Wei X, Ugurlu O, Akinc M. Dissolution behavior and cytotoxicity test of Si, Zn-modified tricalcium phosphate. to be submitted.

29. Wei X, Akinc M. Resorption rate tunable bioceramic: Si&Zn-modified tricalcium phosphate. In: Mizuno M, editor. Ceramic Engineering and Science Proceedings--Proceeding of the 29th International Conference on Advanced Ceramics and Composites. Cocoa Beach: The American Ceramic Society, 2005. p. 129-136.

30. Jorgensen JD, Faber J, Carpenter JM. electronically focused time-of-flight powder diffractometers at the intense pulsed neutron source. J Appl Cryst 1989;22:321-333.

31. VonDreele RB, Larson AC. General Structure Analysis System (GSAS), Los Alamos National Laboratory, Report LAUR 86-748., 2004.

32. Nurse RW, Welch JH, Gutt W. High-temperature phase equilibria in the system dicalcium silicate-tricalcium phosphate. Journal of the chemical society 1959:1077-1083.

33. Dickens B, Schroeder LW, Brown WE. Crystallographic Studies of the Role of Mg as a Stabilizing Impurity in β-tricalcium phosphate: I. The Crystal Structure of Pure β-tricalcium phosphate. J Solid State Chemistry 1974;10:232-248.

34. Wei X, Akinc M. Si,Zn-modified tricalcium phosphates: A phase composition and crystal structure study. Key Engineering Materials 2005;284-286:83-86.

35. Pecharsky V, Zavalij P. Fundamentals of Powder Diffraction and Structural Characterization of Materials. 1st ed. ed. Boston, USA: Kluwer Academic Publishers, 2003.

36. Rawal A, Schmidt-Rohr K. The Dispersion of SiO_2 in Tricalcium Phosphate Elucidated by Solid-State NMR. to be submitted.

37. Elliott JC. Structure and Chemistry of the Apatites and other Calcium Orthophosphates.

London: Elsevier, 1994.

38. Yashima M, Sakai A, Hoshikawa A. Crystal structure analysis of β-tricalcium phosphate $Ca_3(PO_4)_2$ by neutron powder diffraction. Journal of Solid State Chemistry 2003;175:272–277.

39. Waddington TC. Advances in Chemistry and Radiochemistry. New York: Academic Press, 1959.

40. Shannon RD. Revised effective ionic radii and systematic studies of interatomic distances in halides and chalcogenides. Acta Crystallographica, Section A: Crystal Physics, Diffraction, Theoretical and General Crystallography A 1976;32(5):751-767.

41. Brown ID, Shannon RD. Empirical bond-strength-bond-length curves for oxides. Acta Cryst. 1973;A29:266-282.

Table 1 Ionic Radii of some substituted ions for Ca and P

Ion	Ca^{2+}	Mg^{2+}	Zn^{2+}	Cd^{2+}	P^{5+}	Si^{4+}
Coordination number (CN)	6	6	6	6	4	4
Ionic Radii (IR in Å)	0.99	0.65	0.74	0.95	0.17	0.26

Table 2 A part of refinement results of neutron diffraction data for Si,Zn-TCP

Space group		R3c
Unit-cell parameters		$a = b$ =10.3958(1)Å c = 37.3122(7) Å
Unit cell volume		3491.15(5) $Å^3$
Calculated unit cell formula weight		6665.916
Calculated Density		3.17 g/cm^3
Number of data points used		11819
Number of reflections used		Histogram 1: 1418 Histogram 2: 454 Histogram 3: 138
Reliability factors	Rwp	3.99%
	Rp	2.99%
	χ^2	5.426

Table 3 Atomic Positions and isotropic thermal parameter

Atom	w_{yc}	x	y	z	Occupancy	B (Å^2)
Ca1	18b	-0.2745(3)[a]	-0.1414(4)	0.1661(1)	1.000	0.24(6)
Ca2	18b	-0.3841(3)	-0.1762(4)	-0.0344(1)	1.000	0.62(7)
Ca3	18b	-0.2729(2)	-0.1475(3)	0.0604(1)	1.000	1.49(6)
Ca4	6a	0.0000	0.0000	-0.0754(3)	0.44(6)	0.12(30)
Zn4	6a	0.0000	0.0000	-0.0754(3)	0.05(6)	0.12(30)
Zn5	6a	0.0000	0.0000	-0.2643(1)	1.000	0.56(7)
P1	6a	0.0000	0.0000	0.0001(1)	0.73(6)	0.49(15)
Si1	6a	0.0000	0.0000	0.0001(1)	0.27(6)	0.49(15)
O9	18b	0.0102(3)	-0.1354(2)	-0.0122(1)	1.000	1.61(6)
O10	6a	0.0000	0.0000	0.0426(1)	1.000	3.69(16)
P2	18b	-0.3141(3)	-0.1398(3)	-0.1315(1)	1.000	1.00(7)
P3	18b	-0.3469(2)	-0.1517(3)	-0.2338(1)	1.000	1.77(7)
O1	18b	-0.2666(3)	-0.0875(2)	-0.0923(1)	1.000	1.77(7)
O2	18b	-0.2385(3)	-0.2233(2)	-0.14450(0)	1.000	1.37(8)
O3	18b	-0.2701(2)	0.0045(2)	-0.15303(9)	1.000	0.36(6)
O4	18b	-0.4840(2)	-0.2401(3)	-0.13571(9)	1.000	1.23(6)
O5	18b	-0.3941(2)	-0.0412(2)	-0.22208(9)	1.000	0.38(6)
O6	18b	-0.4231(3)	-0.3053(2)	-0.21533(9)	1.000	1.24(6)
O7	18b	-0.1801(2)	-0.0794(2)	-0.22511(9)	1.000	0.69(5)
O8	18b	-0.3725(2)	-0.1763(3)	-0.27433(9)	1.000	0.78(6)

[a] Numbers in parenthesis are estimated standard error in the last digit

[b] Constrains were setup for Ca(4), Zn(4), P(1) and Si(1):

Coordination: x (Ca) = x (Zn) ; y (Ca) = y (Zn) ; z (Ca) = z (Zn); x (P) = x (Si); y (P) = y (Si); z (P) = z (Si)

Thermal Parameters: B (Ca) = B (Zn); B(P)=B(Si)

Ocuupancy: F(Ca) + F(Zn) = 1; F(P) + F(Si) = 1

Table 4 Cation-Oxygen bond lengths and bond angle variance in Si,Zn-TCP

		β-TCP[a]	Si,Zn-TCP
Ca(1)	O(6)	2.316(4) Å	2.319(4)[b] Å
CN=7	O(5)	2.393(4)	2.463(4)
	O(8)	2.421(4)	2.391(3)
	O(4)	2.449(5)	2.467(4)
	O(9)	2.456(5)	2.475(4)
	O(4')	2.503(4)	2.484(4)
	O(3)	2.507(4)	2.533(4)
Ca(2)	O(3)	2.369(4)	2.369(4)
CN=8	O(9)	2.371(5)	2.353(4)
	O(7)	2.398(4)	2.404(5)
	O(7')	2.419(4)	2.413(4)
	O(2)	2.437(4)	2.447(4)
	O(1)	2.444(5)	2.425(4)
	O(5)	2.704(4)	2.629(4)
	O(6)	2.752(4)	2.707(4)
Ca(3)	O(5)	2.384(4)	2.382(4)
CN=8	O(3)	2.388(4)	2.408(4)
	O(8')	2.544(4)	2.578(4)
	O(6)	2.558(4)	2.563(4)
	O(2)	2.568(5)	2.550(3)
	O(10)	2.580(4)	2.547(2)
	O(8)	2.611(4)	2.544(4)
	O(1)	2.650(5)	2.643(4)
Ca, Zn(4)	O(1,1',1")	2.538(5)	2.527(4)
CN=3	O(9,9',9")	3.041(11)	2.775(10)
Zn(5)	O(4,4',4")	2.238(4)	2.175(4)
CN=6	O(7,7',7")	2.287(4)	2.185(5)
	O(4)-Zn(5)-O(4)	82.7(1)°	81.85(19)°
	O(7)-Zn(5)-O(7)	77.1(1)°	80.18(20)°

[a] Data from reference [33]

[b] The number in parentheses is the standard error in the last digit as estimated in the final cycle of full-matrix least squares refinements.

Table 5 Summary of the geometry of the PO_4 groups in Si,Zn-TCP

		β-TCP[a]	Mean	Si,Zn-TCP	Mean
P,Si(1)	O(9,9',9")	1.536(5) Å	1.517 Å	1.534(2) Å	1.561 Å
	O(10)	1.498(12)		1.587(6)	
	O(9)-P(1)-O(9')	109.8(4)°	109.5°	111.43(17)°	109.43°
	O(9)-P(1)-O(10)	109.2(4)°		107.43(18)°	
P(2)	O(1)	1.539(4) Å		1.554(4) Å	
	O(2)	1.532(4)	1.535 Å	1.519(4)	1.543 Å
	O(3)	1.530(4)		1.554(5)	
	O(4)	1.537(4)		1.546(4)	
	O(1)-P(2)-O(2)	110.2(2)°		110.37(24)°	
	O(1)-P(2)-O(3)	105.5(2)°		105.08(24)°	
	O(1)-P(2)- O(4)	112.0(3)°	109.5°	112.79(22)°	109.47°
	O(2)-P(2)-O(3)	115.9(2)°		113.17(25)°	
	O(2)-P(2)-O(4)	108.5(3)°		108.85(24)°	
	O(3)-P(2)-O(4)	104.9(2)°		106.56(21)°	
P(3)	O(5)	1.548(4) Å		1.521(4) Å	
	O(6)	1.532(4)	1.535 Å	1.546(4)	1.536 Å
	O(7)	1.542(4)		1.541(4)	
	O(8)	1.518(4)		1.534(4)	
	O(5)-P(3)-O(6)	114.0(2)°		117.36(25)°	
	O(5)-P(3)-O(7)	107.7(2)°		106.31(21)°	
	O(5)-P(3)-O(8)	107.8(2)°	109.48°	108.40(19)°	109.46°
	O(6)-P(3)-O(7)	106.8(2)°		106.24(19)°	
	O(6)-P(3)-O(8)	108.9(2)°		108.09(22)°	
	O(7)-P(3)-O(8)	111.7(2)°		110.36(21)°	

[a] Data from reference [33]

[b] The number in parentheses is the standard error in the last digit as estimated in the final cycle of full-matrix least squares refinements.

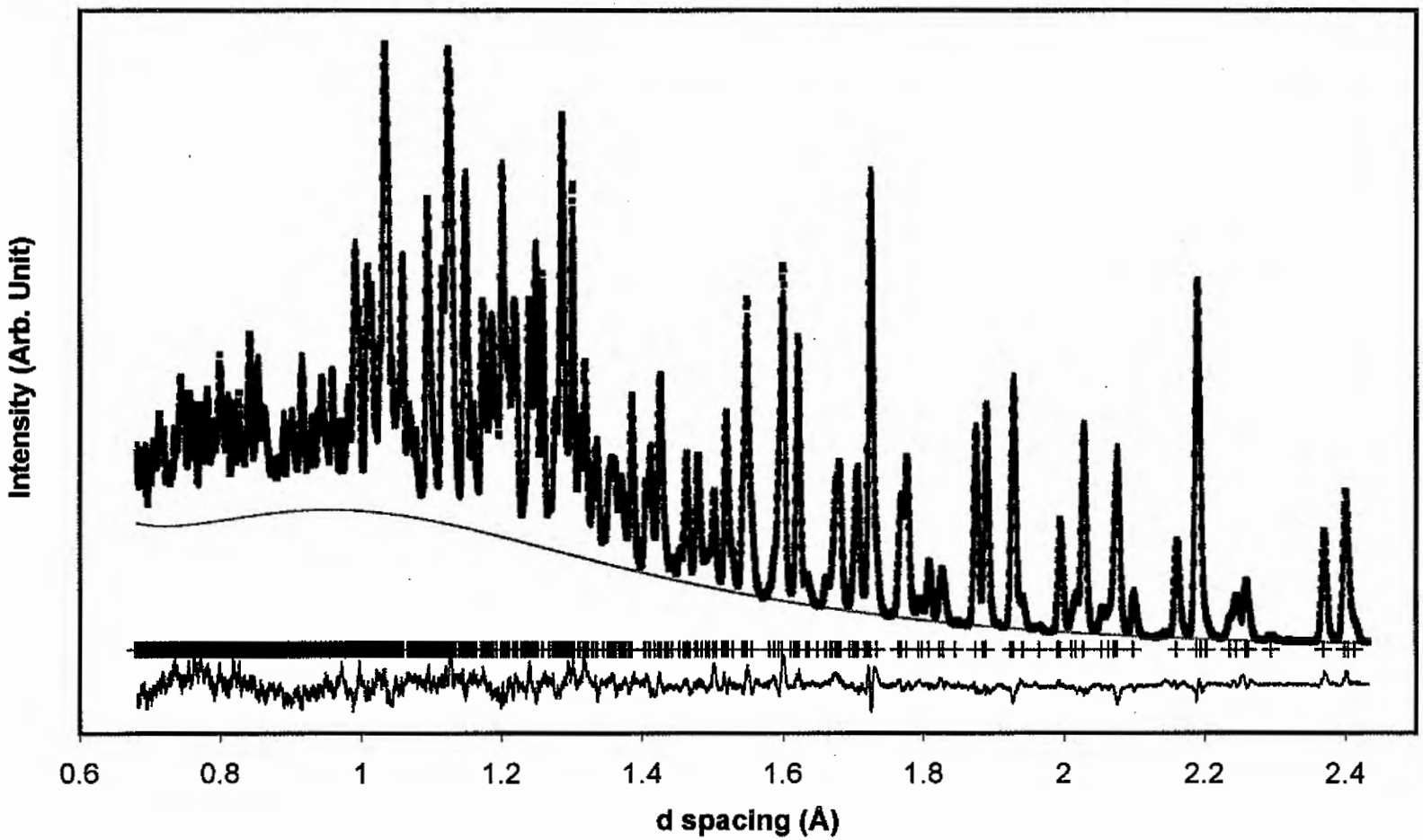

Figure 1 TOF neutron diffraction profile fit to the 145° bank. The observed data are shown as points. The solid line is the calculated profile and the difference curve is shown at the bottom on the same scale. The short vertical "+" lines show the position of Bragg reflections.

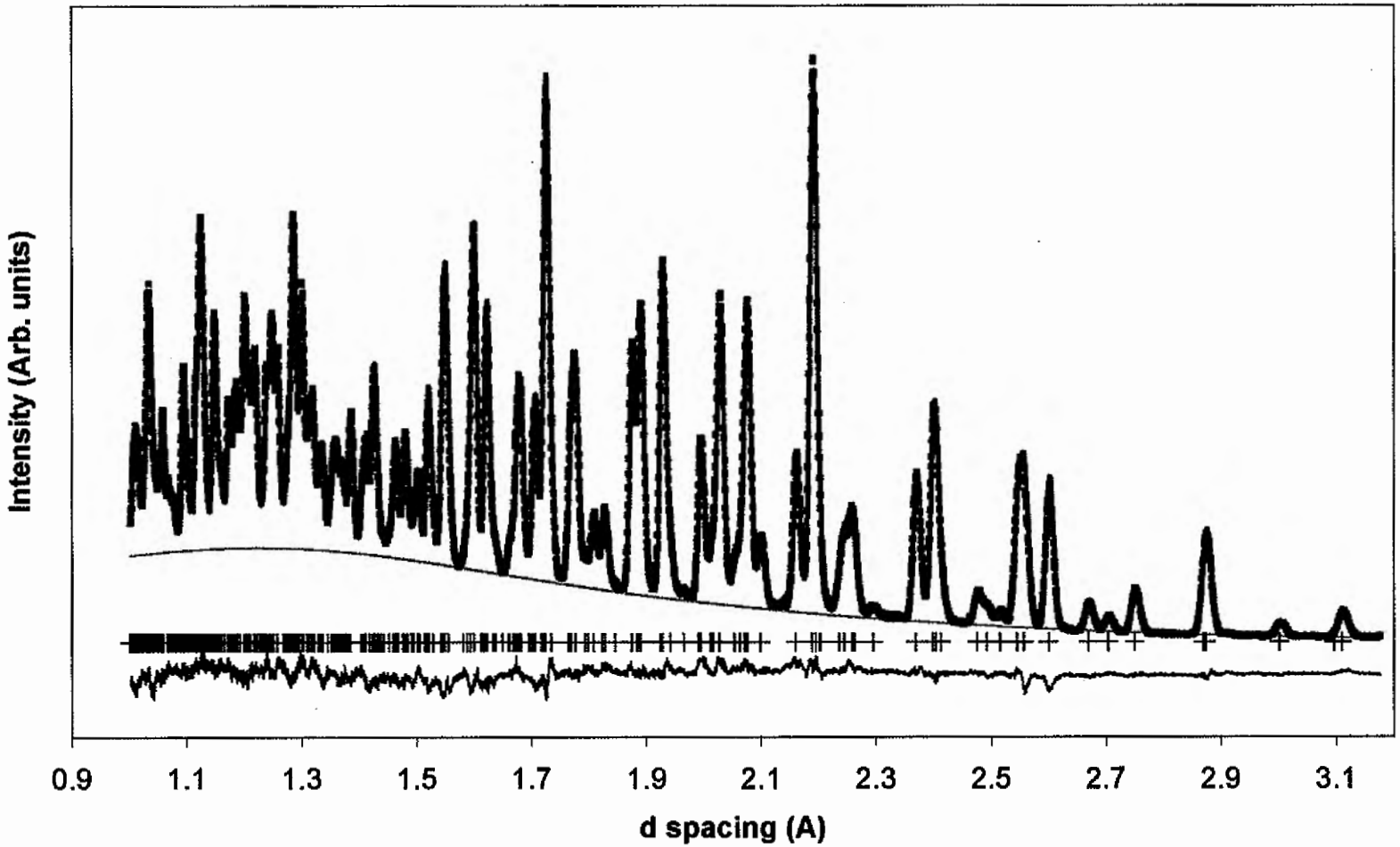

Figure 2 TOF neutron diffraction profile fit to the 90° bank. The data are shown as points. The solid line is the calculated profile and the difference curve is shown at the bottom on the same scale. The short vertical "+" lines show the position of Bragg reflections.

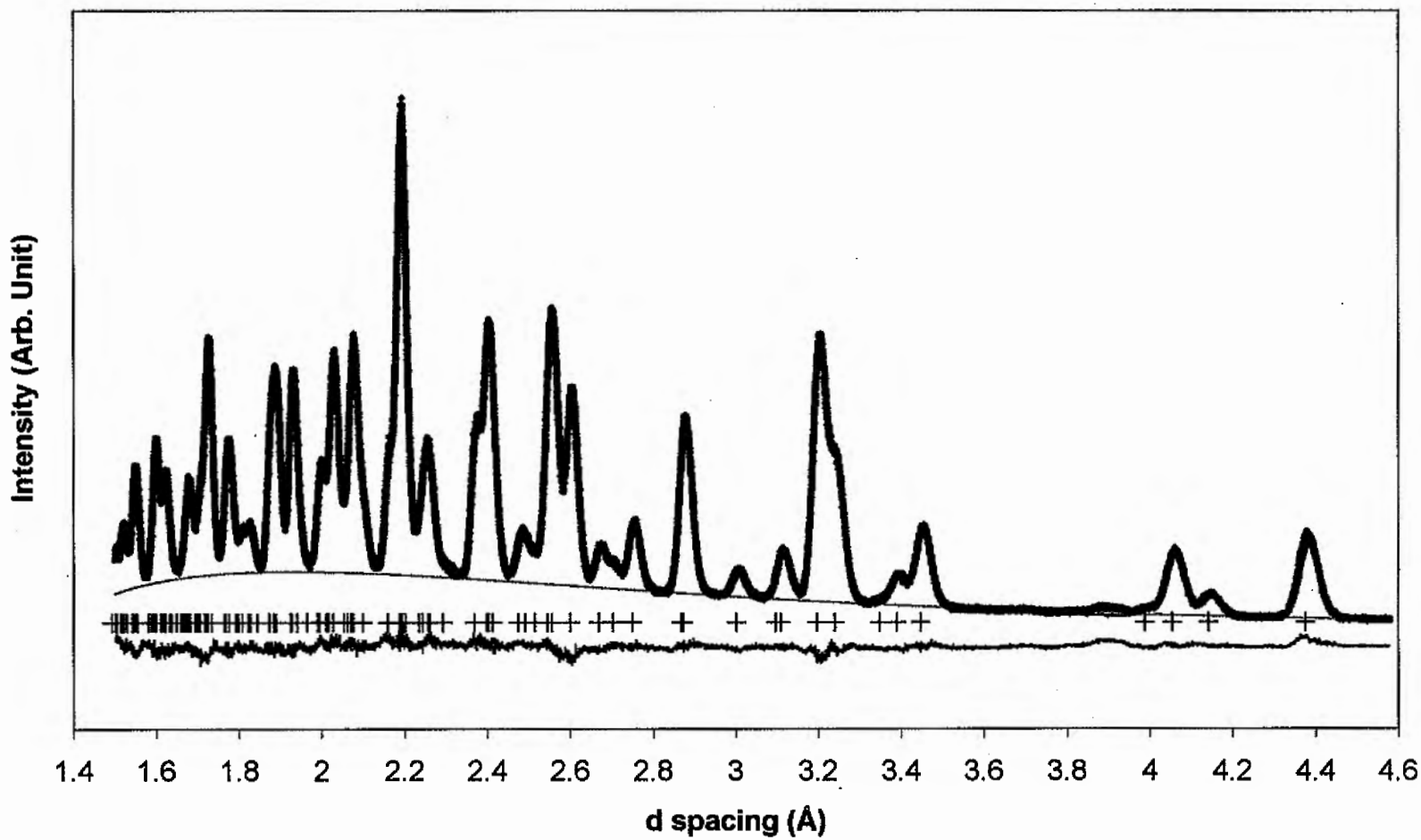

Figure 3 TOF neutron diffraction profile fit to the 53° bank. The data are shown as points. The solid line is the calculated profile and the difference curve is shown at the bottom on the same scale. The short vertical "+" lines show the position of Bragg reflections.

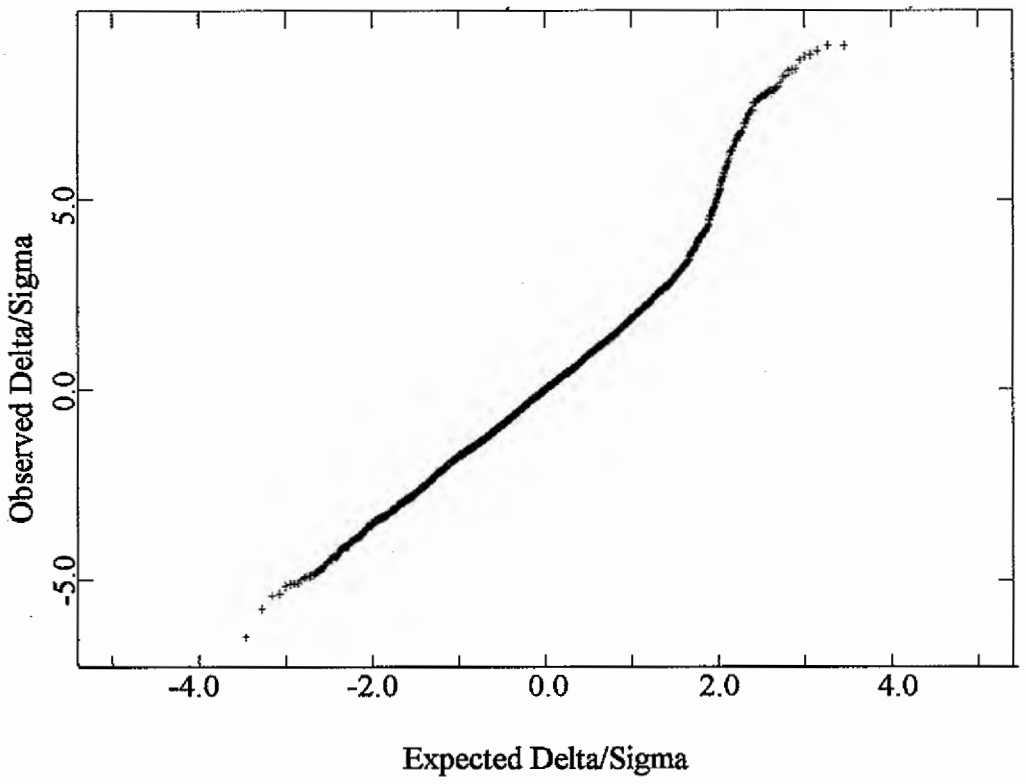

Figure 4 Normal Probability Plot of Histogram 3 for Si,Zn-TCP after the final refinement

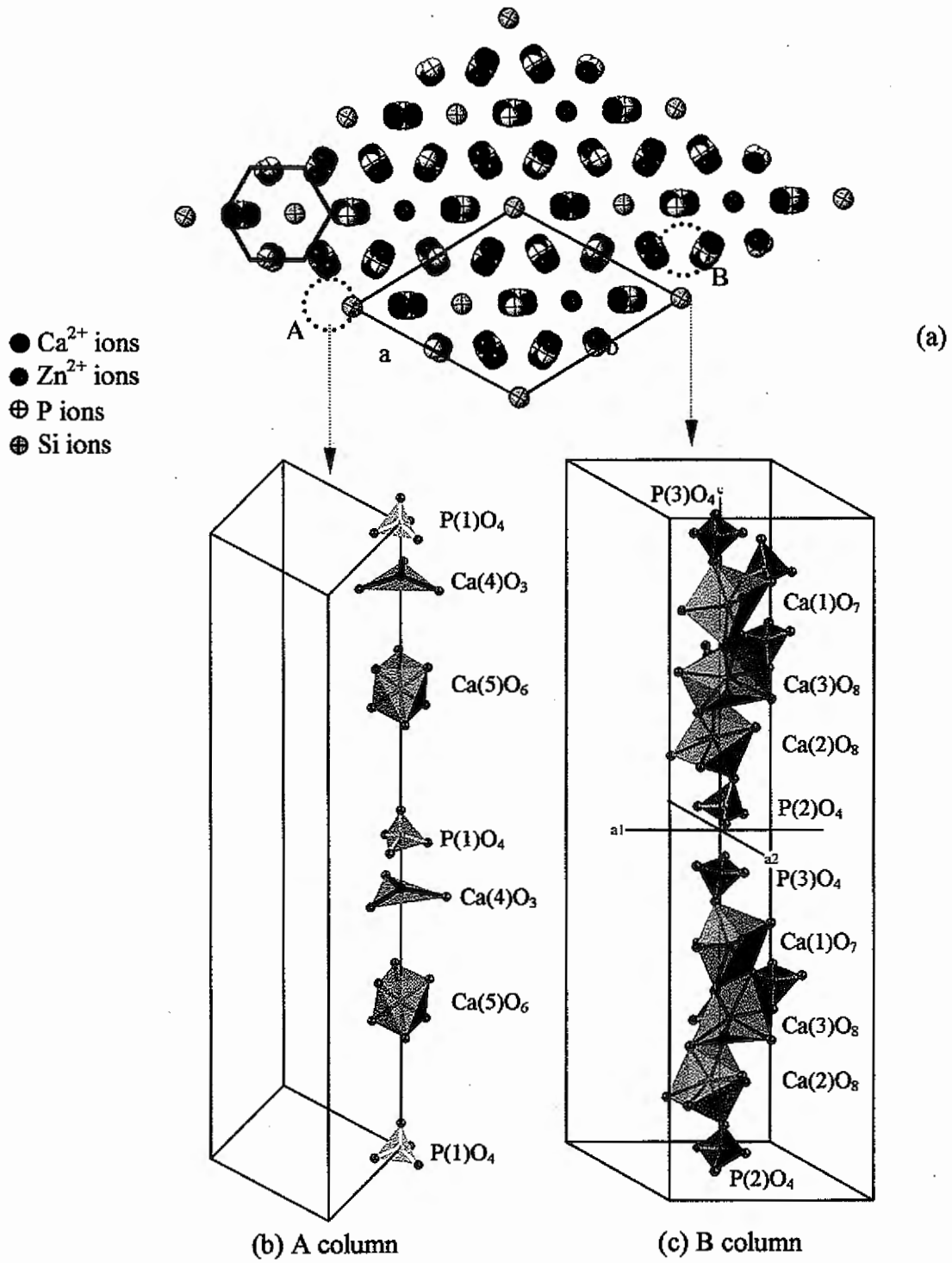

Figure 5 (a) Projection of the crystal structure of TCP along the [001] direction, showing the hexagonal unit cell with A and B columns. Oxygen atoms were deleted for clarity. (b) and (c) are the configuration of CaOn and PO_4 groups in the A and B columns, respectively, along the *c*-axis of the hexagonal cell.

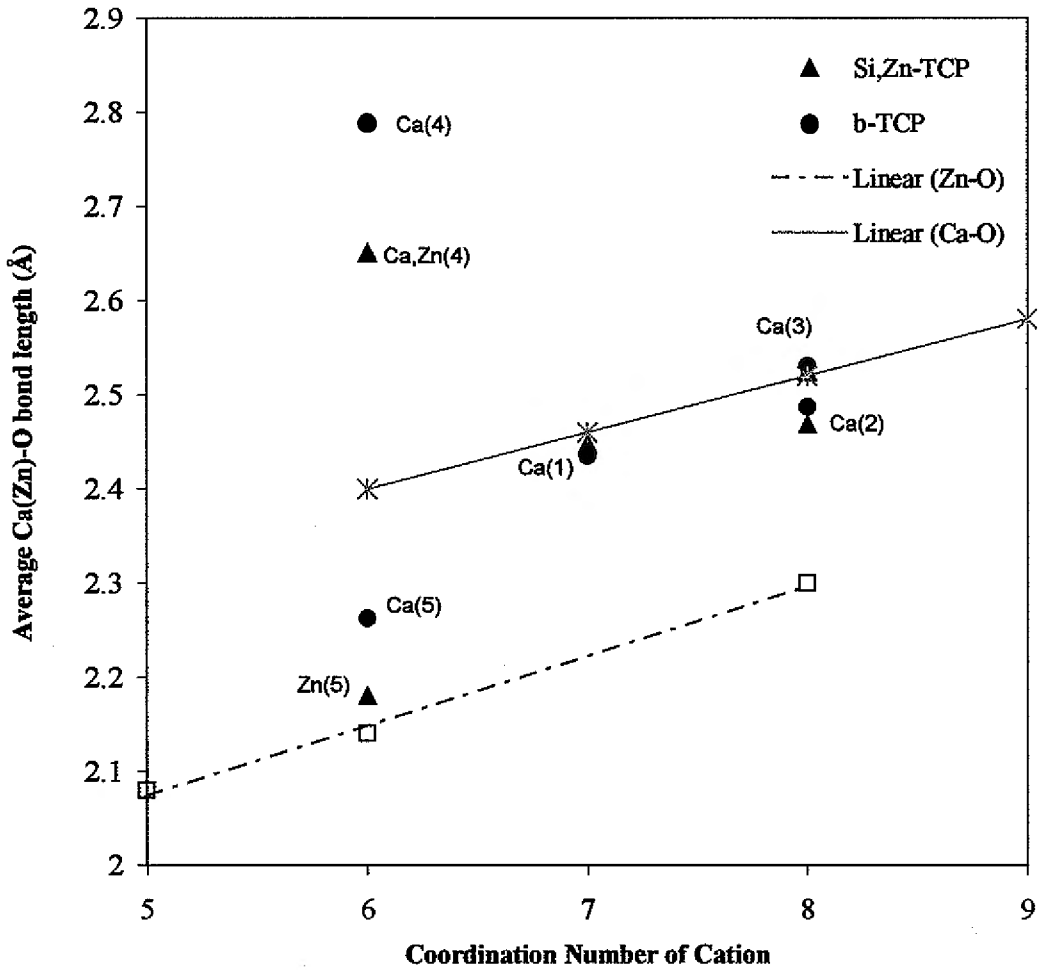

Figure 6 Relationship between the CN and the average Ca(*i*)-O bond length in the pure β-TCP[15] and Si,Zn-TCP (*I*=1, 2, 3, 4, and 5). The crosses and solid line represents the calculated Ca(*i*)-O bond lengths per ionic radii; the open square and dot line are the calculated Zn(*i*)-O bond lengths per ionic radii [19].

CHAPTER 5:

DISSOLUTION BEHAVIOR OF Si,Zn-MODIFIED TRICALCIUM PHOSPHATES

A manuscript to be submitted to *Biomaterials*

Xiang Wei, Ozan Ugurlu and Mufit Akinc*

Department of Materials Science and Engineering and Ames Laboratory, Iowa State University, Ames, IA 50011, USA.

* Email: makinc@iastate.edu

Abstract

Synthetic materials for the reconstruction of bone defects have to fulfill a wide range of requirements: they should be biocompatible and ideally osteoconductive; they should have suitable mechanical properties if used in load bearing bone defects; they also have to be bio-resorbable with a degradation characteristic that allows the organism to replace the implant material by fully functional bone in a balanced time schedule. Silicon and zinc modified tricalcium phosphate (Si,Zn-TCP) was synthesized as a candidate for resorbable temporal bone implant having a controlled solution-driven resorption rate (i.e. dissolution rate) and pharmaceutical effect to stimulate osteogenetic activity for new bone growth. Si and Zn effect on dissolution behavior of tricalcium phosphate (TCP) has been investigated. The dissolution study was carried out in the simulated body fluid (SBF) at 37°C. The concentration changes of calcium and phosphorus in SBF by sample dissolution/precipitation were measured. Surface morphologies and phase composition of the sample before and after immersion were followed as a function of time. The experimental results show that the dissolution rate decreases with increasing Si and Zn content in TCP. Zinc inhibits HAp reprecipitation from SBF, while Si induces HAp formation. The additives appear to modify the dissolution mechanism by altering the phase composition, stabilizing the structure and

changing the surface characteristics. The cytotoxicity test shows that Si and Zn addition has no cytotoxic behavior on the cell within the additive level employed in this study.

Keywords: Tricalcium phosphate, Dissolution, Simulated body fluid, Hydroxyapatite, Calcium phosphate, Cytotoxicity

I. Introduction

The synthetic materials for bone repair and augmentation have been investigated for many years. In the early 1970s, Driskell used the beta-tricalcium phosphate (β-$Ca_3(PO_4)_2$, β-TCP) to repair hard-tissue avulsive wounds and oro-facial fractures [1]. Subsequent research has shown that this porous and resorbable implant material may eliminate a second operation to obtain autogenous grafting materials. It has a shelf life of at least eight years. When placed in close position to the freshly cut and bleeding bone, the ceramic matrix is rapidly invaded by bone-forming tissue. Meanwhile, the implant is resorbed and the process continues for approximately six to 18 months [2]. It has been reported that TCP is more bioresorbable than hydroxyapatite ($Ca_5(OH)(PO_4)_3$, HAp), which has a relatively slow resorption rate compared to rates of new bone formation [3,4].

The bioresorption of TCP is assumed to take place by both cell-mediated and solution-driven processes [5]. As reported previously, the TCP has a much higher dissolution rate than the stoichiometric HAp (s-HAp)[6,7]. The dissolution rate of dense β-TCP was 12.3 times higher than that of dense HAp in buffered lactic acid solution (0.4M, pH 5.2), and was 22.3 times higher than that of HAp in buffered EDTA solution (0.05M, pH 8.2) [6]. Aoki proposed that α-TCP dissolves in the body 10 times faster than HAp [8]. Ducheyne et al. compared the dissolution rates of six calcium phosphates in calcium and phosphate free solution at pH 7.3. In terms of the dissolution of calcium, the dissolution rate increased from s-HAp to tetra calcium phosphate (TTCP) in the following order [9]:

$$\text{TTCP} > \alpha\text{-TCP} > \beta\text{-TCP} > \text{OCP} > \text{CDHA} > \text{s-HAp}$$

where OCP is octacalcium phosphate, CDHA is calcium-deficient hydroxyapatite and α-TCP is the high temperature phase of TCP. Although pure TCP has good resorbablility, the higher solubility and faster dissolution rate results in strength reduction during the bone

remodeling process, and finally leads to the implant failure. An ideal bone implant material would simultaneously be resorbed, meanwhile maintaining the strength and supporting the activity of osteoblasts in the development of new bone [10]. Thus, from the point of physico-chemical process view, the suitability of TCP for use in vivo is critically dependent on how the dissolution rate might be controlled by different mechanisms.

A number of studies have been carried out to understand the effects of additives on the dissolution behavior of calcium phosphate [10-20]. The results revealed that the halide (e.g. F^- and Cl^-) ions could substitute hydroxide and stabilize HAp structure. Hence, the solubility of HAp decrease and the dissolution is inhibited. On the other hand, the substitution of divalent cations (e.g. Mg^{2+} and Zn^{2+}) for Ca^{2+} sites and the substitution of complex anions (e.g. SiO_4^{4-}, TiO_4^{4-}, and CO_3^{2-}) for PO_4^{3-} will increase the distortion of the HAp structure and lead to the enhancement of the solubility. The content of these additives in HAp structure is limited, and at a higher additive level HAp will decompose to form TCP phase. From the crystallography point of view, TCP crystal can supply better environment for these impurities substitution due to the original distortion in the structure [21-24]. These additives were claimed to stabilize TCP, but enhance HAp dissolution. It is important to note that Si addition can stabilize the high temperature phase α-TCP, which has higher solubility and dissolution rate. α-TCP powder sets to form calcium-deficient HAp when mixed with water, and thus is used in dental and medical clinical practice as a root sealer and bone-filling cement [25-31]. This material is moldable and could adapt to the bone cavity, eliminating the need for high temperature sintering of the implant material common in traditional ceramic processing operation. Hence, the biphasic α-/β-TCP with controlled dissolution behavior may be a promising resorbable biomaterial as a temporary implant.

In this work, silicon and zinc were added to modify the dissolution behavior of TCP. The previous X-ray diffraction results showed that Si and Zn doped TCP (Si,Zn-TCP) is composed of a mixture of α- and β-TCP phases [32]. The α:β phase ratio was found to be dependent on the additive content. No secondary phase was observed in the X-ray diffraction pattern, indicating that Zn and Si are incorporated into the TCP structure after high temperature sintering [33]. The crystal structure study from X-ray and neutron diffraction

data confirmed that Si and Zn substitution for P and Ca sites decreased the distortion and stabilized TCP structure [21,32]. Meanwhile, the solid state NMR and neutron diffraction analysis show that the only one-third Si substitutes for P sites and the remaining forms the Si-rich nano-scale phase as the secondary phase. The purpose of this study is to understand the dissolution behavior of tricalcium phosphates that are modified by substitution of Si and Zn at concentrations less than 10 mol%. The dissolution behavior was studied in the simulated body fluid (SBF) at 37°C and pH=7.4, which is usually utilized for the first step in evaluating biomaterials and is more precisely mimic the physico-chemical behavior in vivo.

The pharmaceutical effect was also considered during the selection of additives used in this research. Zinc has been found in all human tissues and the concentration of Zn in bone is higher than in most other tissues [34]. Zinc ions were suggested to have an active participation in the synthesis of the biological apatite crystals under in vivo conditions [34]. In clinical studies, Walsh et al. have demonstrated the efficacy of Ca, Cu, Mn and Zn supplementation on spinal bone mineral density in postmenopausal women [35]. Silicon is known to be essential for the growth and development of vertebrates, and perform a vital role in skeletal development [36-38]. Silicon deficiency has been found to retard bone development in chicks [39]. Dietary silicon has been found to increase the rate of bone calcification, and nodular ill-formed bone results from silicon deficiency [36,37]. An increase in dietary silicon has been directly linked to an increase in bone mineralization. Therefore, Si,Zn-TCP was also designed to stimulate osteogenesis for new bone growth by slowly releasing Si and Zn to the local environment.

II. Materials and Method

The chemical reagent grade $CaCO_3$, $NH_4H_2PO_4$, ZnO (Fisher, Hampton, NH) and fumed SiO_2 (Sigma-Aldrich, St. Louis, MO) were used as received. The mixture at predetermined mole ratio of the starting powders was first milled in anhydrous ethanol for 4h using alumina media. The slurries were vacuum filtered. For Si,Zn-TCP and pure α-TCP, the precursor powder were then fired in alumina combustion boat in an open atmosphere furnace at 1300°C for 6 hours and quenched in dry air. The β-TCP was produced by sintering $CaCO_3$ and $NH_4H_2PO_4$ at 1000°C for 4 hours. The biphasic α-/β-TCP without additives was obtained

by heating the β-TCP in air at 1300°C for 2 hours and cooling slowly. The fired powder was ground using an alumina mortar and kept in a desiccator. The fraction of each phase of the biphasic powders was determined by X-ray powder diffractometer (XRD) (Scintag X1, Cupertino, CA), using the pure β-TCP and α-TCP standards. An accelerating voltage 45kV and a current of 40 mA were used. The XRD data were collected over 2θ range of 10-80° at a step size of 0.02°. Table 1 lists the eight samples with their additive content and phase ratio, which was calculated by integrating the phase distinct peak area of α and β phases respectively.

All samples were crushed and sieved to obtain the desired grain size approximately 20 μm in diameter. Dissolution experiments were carried out in sealed glass bottles in a water bath shaker. Two grams of granules were placed in 100 ml simulated body fluid (SBF) at 37°C. The ion concentration of SBF is given in Table 2 [40]. The pH of the solution was monitored by Fisher AR15 pH meter (Fisher, Hampton, NH), with an accuracy of ±0.02. A 2.5 mL of solution was taken out after the certain time for Ca and P concentration analysis. Ca concentration was determined by an atomic absorption spectroscopy (AAS) (Perkin-Elmer 5000, Wellesley, MA). After 0.25mL lanthanum solution was added to control interferences, the solution was diluted to 25 mL. Samples were run in triplicate for each data point. As a reference, the standard solution for AAS were prepared using the same ion concentrations of SBF except Ca^{2+}. Phosphorus concentration was determined colormetrically using the ascorbic acid molybdate method (EPA Method 365.4). After aging the sample for a predetermined time, it was centrifuged, washed by de-ionized water and dried in vacuum prior to XRD analysis. Microstructure evolution was followed by the scanning electron microscopy (SEM) (JEOL JSM-606LV, Peabody, MA) and transmission electron microscopy (TEM) (Philips CM30, 300kV, Netherlands). The powder specimens for TEM were ground in acetone, and collected on 200 mesh carbon-coated copper TEM grids. Electron beam transparent particles were chosen for TEM examination by selected area diffraction (SAD). Energy-dispersive X-ray spectrometer (EDS) was used to confirm the elemental composition of the samples.

Cytotoxicity tests of samples containing Si and Zn were performed by a direct contact assay outlined by the American Standards for Testing and Measurements [41]. The SKOV3

human ovarian carcinoma cell line was used for cytotoxicity experiments. Cells were cultured with low-glucose Dulbecco's modified eagle medium (DMEM) containing 10% fetal bovine serum (FBS, Sigma, St. Louis, MO). Neither antibiotics nor antimycotics were used to avoid the possibility of artificial membrane permeabilization effects from these agents. Cell cultures were maintained in a humidified environment with 5% CO_2 at 37°C and passaged regularly to allow them to remain sub-confluent. Samples were sterilized by swabbing with 70% ethanol and dried in aseptic conditions. The media was removed from the well plates containing the cells and the samples were placed into the wells, leaving one well empty for comparison. Media was added to the wells and the plates with samples were placed in an incubator for another 24 h. All samples were run in four replicates, and experiments were repeated twice. After incubation with samples, changes in morphology and detachment of cells from the dish were also observed using an Olympus IMT-2 (Melville, NY) inverted, phase-contrast light microscope equipped with objective of 100x magnification.

III. Results and Discussion

1. Dissolution and Precipitation

Variation of the calcium and phosphor concentration of α-TCP, β-TCP, Si,Zn-3, Si,Zn-5, Si,Zn-10, Si-5, Zn-5, and α-/β-TCP as a function of time in the SBF solution are presented in Figure 1 and Figure 2 respectively. Except Zn-5 and Si,Zn-10, the other six samples exhibit qualitatively similar response with time. That is, both Ca and P concentrations increased in the first few days, reached the maximum value and then decreased with the longer immersion time. This behavior may be explained by an initial dissolution of Ca^{2+} and PO_4^{3-} followed by reprecipitation in the form of HAp as the solution becomes supersaturated.

Generally, the dissolution and precipitation rate of calcium phosphates may be interpreted in terms of an empirical kinetic equation [42]:

$$R = km_0 F(\frac{m}{m_0})\sigma^n \qquad (1)$$

in which m_0 and m are the masses of solid phase initially and at time t, σ is the relative super- or undersaturations, and n is the kinetic rate order of reaction. $F(m/m_0)$ represents the influence of changes in the sizes and shapes of the crystals, including the surface area. The relative super- and understaturation may be expressed in terms of equation 2.

$$\sigma = \pm\left[\left(\frac{IP}{K_{SO}}\right)^{1/\nu} - 1\right] \tag{2}$$

with

ν = the number of ions in the formula unit

IP = *the ionic activity product*

K_{SO} = the equilibrium constant or the ionic activity product at saturation

The dissolution and precipitation is a reversible reaction. The direction that the reaction will move in is determined by the difference between the IP and the equilibrium constant K_{SO}. The initial ionic activity product IP_0 in solution is below K_{SO}, which leads to dissolution until saturation concentration is reached. The dissolution rate will decrease with increasing IP. The reaction on the surface will reverse to precipitation when $IP > K_{SO}$. The value of IP for TCP and HAp can be expressed as:

$$IP = [Ca^{2+}]^3[PO_4^{3-}]^2 y_1^3 y_2^2 \tag{3}$$

$$IP = [Ca^{2+}]^{10}[PO_4^{3-}]^6[OH^-]^2 y_1^{10} y_2^6 y_3^2 \tag{4}$$

where y_i is the ionic activity coefficient decided by the ionic strength. Since IP is related to concentration, the dissolution and precipitation reactions could be simply implied by the concentration change in the solution. If the ionic concentration C is lower than the equilibrium concentration C_∞ in the solution, the dissolution takes place. Conversely, the precipitation takes place when C is higher than C_∞.

However, the dissolution of TCP in SBF is a much more complicated process. According to the solubility phase diagram for the ternary $Ca(OH)_2$-H_3PO_4-H_2O system at 37° [43], there are only two calcium phosphate materials that are stable at room temperature when in contact with aqueous solution. At a pH lower than 4.2, the component $CaHPO_4 \cdot 2H_2O$ (Dicalcium phosphate dihydrate) is the most insoluble phase, while at

higher pH (>4.2) HAp is the most stable calcium phosphate phase. Hence, it may be already supersaturated with respect to the stable HAp phase before the initial dissolution leads to a saturated solution with respect to the unstable TCP phases. This supersaturation drives HAp nucleation and growth on the TCP surface by consuming the Ca and P from the solution. The gradual transition from TCP to HAp surface results in the change in solubility of a TCP surface to a value approaching the solubility of HAp, meanwhile the dissolution rate of TCP decreases. Therefore, the apex of each curve in Figures 1 and 2 is neither the saturation point ($IP = K_S$) for TCP, nor the beginning of HAp precipitation. It can be concluded that the TCP dissolution dominates the reaction in SBF before the ionic concentration reaches the apex; and HAp precipitation rate is faster than TCP dissolution rate after the apex. The concentration gradient of the curve represents the dissolution and reprecipitation rate.

Figure 3 shows the variation of Ca^{2+} concentration with time for the first 24 hours, when the dissolution is the predominant reaction in the solution. The rise of $[Ca^{2+}]$ suggests that the dissolution of pure TCP and Si,Zn-n ($n \leq 5$) commenced immediately after the samples were immersed into SBF. Even Zn-5 sample has a slightly positive slope, indicating release of small amount of Ca^{2+} ions. Within the experimental error, Ca^{2+} concentration remains constant for Si,Zn-10 sample. The pure α-TCP had the fastest dissolution rate despite the reprecipitation of HAp. With increasing additives, the dissolution rate of Si,Zn-TCP decreased. Si-5 dissolves faster than Si,Zn-5 and Zn-5 even though they contain the same additive level. Apparently, Zn depresses dissolution of TCP more effectively than Si. The order of the dissolution rate is:

$$\text{Si,Zn-10} < \text{Zn-5} < \beta\text{-TCP} < \text{Si,Zn-5} < \text{Si,Zn-3} < \alpha\text{-}/\beta\text{-TCP} < \text{Si-5} < \alpha\text{-TCP}$$

In Figures 1 and 2, the concentration gradient (G) of curve after apex implies the HAp precipitation rate since precipitation is the dominant reaction during this period. The largest gradient of Ca and P concentration is observed in pure TCP and $G_{\alpha\text{-TCP}} > G_{\beta\text{-TCP}}$. The gradient of Si,Zn-TCP decreased as increasing additive content, and $G_{Si,Zn\text{-}3} > G_{Si,Zn\text{-}5} > G_{Si,Zn\text{-}10}$. In Figure 2, Si-5 has larger gradient than Si,Zn-5 and Zn-5; the α-/β-TCP sample has smaller gradient then the monophase α-TCP, but larger than other samples. The HAp precipitation rate is summarized as the following order:

Si,Zn-10 < Zn-5 < Si,Zn-5 < Si,Zn-3 < β-TCP < Si-5 < α-/β-TCP < α-TCP

After four weeks, the Ca and P concentrations in SBF still continue decreasing, suggesting that the solution has not reached the equilibrium condition for HAp yet. The precipitation also resulted in a slightly increase in pH of solution, ranging between 7.4 to 7.8 for these samples. This led to the formation of calcium phosphates with a low Ca/P molar ratio, confirmed by previous ICP analysis[44].

2. Phase Composition and Evolution of Morphology in SBF

X-ray diffraction patterns of eight samples before and after aging in SBF are shown in Figure 4. Except Si,Zn-10, all other samples present distinct HAp peaks for (211), (112) and (300) planes after immersion in SBF. The TCP phase content decreases and HAp content increases with the immersion time. For Si,Zn-n (n=3, 5, 10), HAp content decrease with increase of the additive level. There is no HAp phase identified in Si,Zn-10 sample after four weeks immersion. Although α-/β-TCP and Si,Zn-3 have the similar phase composition before aging in SBF, HAp content in α-/β-TCP is much larger than in Si,Zn-3 after immersion. For samples with the same additive level of 5%, it is obvious that HAp favors to precipitate on Si-5, rather than on Zn-5.

The surface morphological changes with immersion in SBF of the samples are shown in Figure 5. The surface of pure TCP (α and β) shows a characteristic solution-precipitated needle-like morphology of HAp after four weeks exposure to SBF (Fig. 5a). This typical morphology is also shown in TEM micrographs (Figure 6). The fine HAp grains are about 1nm in width and a few tens of nanometers in length in two weeks sample (Fig. 6a). After four weeks, the HAp grains grow into thin fiber-like crystals, radiating from the center out. The crystal size is about 20nm in width and about 300nm in length (Fig. 6b). EDS analysis performed in the TEM on these crystals confirmed the presence of calcium and phosphor and the Ca/P ratio is about 1.5, indicating this phase is calcium-deficient HAp. This HAp layer on TCP surface is not continuous, and some TCP surface can still be observed (Fig. 6b). Si-5 formed a much denser HAp layer on the surface, consisting of aggregates of small flaky crystals (Fig. 5b). Si,Zn-3 and Si,Zn-5 exhibit larger and granules on some particle surface instead of needle-like crystals (Fig. 5c&d). In the micrograph of Si,Zn-5, a big particle with

the clean and smooth surface was also observed after four weeks immersion, similar to the particle morphology shown in Zn-5 and Si,Zn-10 micrographs. This morphology suggests that HAp has preferred nucleation sites.

In Figure 6d, TEM micrograph of Si,Zn-3 shows four different particle morphologies after immersion: small and irregular shape particles (A), bigger and clean particles (B), needle-like crystal aggregates (C), and nanosized spherical grains aggregates (D). They are corresponding to α phase, β phase, HAp phase and initial crystalline HAp, respectively. More morphology details are shown in Figure 8. On the α particle/solution interface, clusters of spherical grains measuring 10 to 20 nm are observed in the high magnification image (Fig. 8b). These grains have the characteristic morphology of precipitations from the solution at the initial stage. The area between spheres is a gel-like amorphous phase since no regular contrast patterns were shown in bright field images during the sample tilting. Variations in the gray scale across the picture are likely due to changes in thickness. TEM examinations reveal broad rings in the diffraction patterns, characteristic of amorphous and nano-size materials, which consistent with the assumption that the amorphous phase is the precursor for crystalline HAp [45-48]. EDS analysis in this area shows much higher Si signal than surroundings, indicating a Si-rich area formed on the α-phase/solution surface. Si might have an active participation in the HAp nucleation process. Figure 8c is the high magnification image of the center particle (D), i.e. nanosized spherical grains aggregates, which has a different morphology from α, β or HAp crystals. The Moire fringes in the high-resolution image shows that this particle consists of aggregates formed by 20 to 50 nm crystallites (Fig. 8d). SAD pattern also presents rings and diffraction points, a characteristic polycrystalline structure with small grains. It is plausible that the HAp phase nucleated from nano-size amorphous particles leading to aggregates of crystalline HAp.

No obvious morphology change was observed in Zn-5 and Si,Zn-10 sample in SEM micrograph (Fig. 5f&g). The HAp phase content and morphology change with the additive level indicate that the additive affects not only TCP dissolution but also HAp precipitation.

3. Mechanism of Additive Effect on Dissolution and Precipitation

The additives may alter the mechanism of dissolution by three ways: adjusting the phase composition, decreasing the solubility and changing the surface properties. The previous XRD study has confirmed that the phase composition could be adjusted by the additive content since Zn favors β phase and Si favors α phase [32]. The biphasic structure in Si,Zn-3 and Si,Zn-5 samples is clearly shown in Figures 5c, 5d and 6c, in which there are two different particle morphologies: one is small in size with irregular shape; the other one is bigger with smooth surfaces. EDS analysis for these two particles shows that the smaller particle has higher Si content than Zn, and the bigger has higher Zn than Si. The selected area diffraction pattern taken from A area of Figure 6c shows the clear hexagonal unit cell of β phase along the $[1\bar{2}1]$ direction. The high-resolution image for particle A is presented in Figure 7a. This is a single particle approximately 50nm in size and consist of several grains. There are two major orientations of the grain (Fig. 7b&c), in which the lattice spacing was measured to be 8.235 Å and 5.294 Å. The index of the pattern in the selected area diffraction pattern is based on the previous crystal study of Si,Zn-3 [33], in which α phase has monoclinic structure of $P2_1/a$ with cell parameters a=12.859 Å, b=27.389 Å, c=15.222 Å and β=125.929°, and the atom positions taken from the α-TCP unit cell [49]. The zone axis of this diffraction pattern is [-4, 2, -1]. In comparison to pure TCP, the d spacing of these two phases has a slight variance due to the Si and Zn substitution, which coincides with the previous crystal structure study [33]. The α:β phase ratio decreased as dopant level increased, and Zn has a dominant effect at the higher additive content [33]. As shown in Table 1, the α:β phase ratio of all samples is in the following order:

β-TCP < Si,Zn-10 < Zn-5 < Si,Zn-5 < α-/β-TCP < Si,Zn-3 < Si-5 < α-TCP

which has the similar sequence to dissolution/precipitation rate of samples studied.

It was already established that the α-TCP had a higher dissolution rate than β-TCP [9,50]. With the same additive level 5%, Si-5 has higher dissolution rate than Si,Zn-5 and Zn-5, as it has over 95% α phase. Similarly, Si,Zn-5 has about 20% α phase, resulting in the higher dissolution rate than Zn-5 which has only 5% α phase. Si,Zn-3 also dissolves faster

than Si,Zn-5 due to the higher α phase fraction. On the other hand, samples with more α phase release Ca^{2+} faster, leading to the high relative supersaturation (σ) and accelerating the HAp precipitation rate. After four weeks in SBF, HAp phase content is much higher in Si-5 than in Si,Zn-5 and Si,Zn-3, while Zn-5 only has very small amount of HAp (Fig. 4). Since α phase with higher dissolution rate form supersaturated region on the surface, HAp favors to nucleate on the surface of α-phase rather than of β-phase. Figure 5d and Figure 6d clearly show that the needle shape HAp crystals grow on α-phase, while the β-phase is devoid of needle-like HAp phase. Inhibiting ability of Zn on HAp nucleation can be accounted by a mechanism offered by Bigi [18,51]. According to him, Zn could enter the HAp pre-nuclei structure embryo, distort it and create a structural mismatch, thus preventing further growth of HAp crystal.

The reduction of TCP solubility can be attributed to increased stability of the crystal structure as a result of zinc and silicon addition. According to the previous crystal structure study of Si,Zn-TCP [21], Zn substitution for Ca sites will results in the contraction and decrease the distortion in pure β-TCP structure. Zn behaves like Mg in whitlockite, which is less soluble than β-TCP [23,52]. Si substitution for P sites increases PO_4^{3-} group distortion in β-TCP, but Zn addition dominates the structure change at higher doping levels. For α-TCP, Yin and Stott proposed that two SiO_4^{4-} may substitute for a pair of PO_4^{3-} groups with an excess Ca^{2+} for charge compensation based on *ab initio* density functional calculations [53]. This substitution leads to a more stable structure than pure α-TCP, and the stability increases with Si concentration. There is a calcium vacancy in the anion–cation columns of the α-TCP structure which provides a particularly favorable location for an excess Ca atom [23]. Therefore, Si,Zn-TCP has lower internal energy and have a lower reactivity in water than pure TCP. As shown in Figure 3, with increase of doping content, the solubility of TCP decreases, leading to decrease of dissolution rate (Si,Zn-10 < Si,Zn-5 < Si,Zn-3). The dissolution rate of Si,Zn-TCP will be less than that of even pure β-TCP when additive content reaches 10%. This result is consistent with Ito's report for zinc-containing tricalcium phosphate, in which the calculated solubility product decreased with increasing of Zn content [13]. The dissolution rate of Si-5 is lower than pure α-TCP, indicating the Si stabilization

effect on α phase. Compared with α-/β-TCP, Si,Zn-3 has more α phase but with lower dissolution rate, indicating both Si and Zn increase the stability of TCP structure.

In Figure 4, the doped TCP shows different surface morphology compared to the pure TCP. Si-5 has a characteristic porous morphology with a network of interconnected particles. According to the phase diagram of $Ca_3(PO_4)_2$-Ca_2SiO_4 [54], Si addition increases the melting point of TCP. This sample exhibited highly porous structure as the result of solid state sintering at 1300°C, which may lead to higher the surface area. According to Equation 1, both dissolution and precipitation rates increase with the larger surface area due to m/m_0 term. However, the effect of surface area on precipitation rate is more prominent in this case due to the effect of Si on stability of the structure. It is clearly shown in Figure 4 that the HAp layer on Si-5 surface is much thicker than on other samples and it may effectively minimize further dissolution of TCP. For the samples containing Zn, most particles have smoother and dense surface with sharp edges. According to Kreidler and Hummel [55], Zn-containing β-TCP melts incongruently around 1500°C, whereas the compound $CaZn_2(PO_4)_2$ melts incongruently at 1040°C. They form a eutectic solidifying at 1029°C. This system is the most suitable for carrying out the process of densification by liquid sintering. Hence, the density and the grain size increase with Zn doping, which may result in the lower surface area and lower dissolution and precipitation rates.

4. Cytotoxicity Test

The results of the cytotoxicity evaluations indicated that the samples doped with Si and Zn displayed no cytotoxic behavior. Images of the cell/sample interface for Si,Zn-TCP, positive control (ZnO powder), and negative control (no sample) are shown in Figure 9. The positive control (Fig. 9a) elicited a cytotoxic response, as expected. The cell density near the ZnO powder interface is extremely low and the few cells that are present appear to have detached from the surface of the well plate. There is also considerable cellular debris present, likely due to cell lysis. In the well without any sample (Fig. 9b), the cell density is constant eliciting no cytotoxic response. The Si,Zn-TCP samples with different additive content (Fig. 9c&d) displayed similar cytotoxic characteristics as the negative control. The cell bodies

were large and healthy. The cell density is constant up to the sample interface, and cells are confluent and fully adhered to the well.

IV. Conclusion

When samples were aged in SBF, dissolution of TCP is not the only reaction in the solution. Reprecipitation of HAp on TCP surface occurs at the same time because HAp is the most stable phase in SBF and TCP initial dissolution can quickly lead to a supersaturated solution with respect to HAp. The gradual transition from TCP to HAp surface results in the change in solubility of a TCP surface to a value approaching the solubility of HAp, meanwhile the dissolution rate of TCP decreases. Before the ionic concentration reaches the apex, the dissolution of TCP dominates the reaction in SBF; and HAp reprecipitation rate is faster than TCP dissolution rate after the apex.

The orders of dissolution/reprecipitation rate and development of phase and surface morphology indicate that both TCP dissolution and HAp reprecipitation behavior might be controlled by varying the Zn and Si doping level. Zn addition inhibits both dissolution and precipitation by stabilizing β-phase structure, forming of low solubility β-phase and reducing surface area as a result of liquid sintering. Si addition decreases the dissolution rate by stabilizing α-phase structure, but it also promotes HAp reprecipitation by forming the highly porous structure. With both Zn and Si addition, Zn has the dominant effect on the Si,Zn-TCP behavior.

Direct contact cytotoxicity tests revealed that Si,Zn-TCP composition investigated in this work are not toxic. The health cells were tightly bounded to the particle surface, suggesting the good biocompatibility of Si,Zn-TCP. In future work, the availability of biphasic materials will be investigated by estimating the osteoconductivity in animal experiments (in vivo) and the expression of mRNA in type I collagen, phosphatase activity and osteocalcine in cell culture.

Acknowledgement

We are grateful to Dr. Ankit Agarwal for SKOV3 cell cultivation and interpretation of the micrographs. Ames Laboratory is operated for the U.S. Department of Energy by Iowa

State University under contract number W-7405-ENG-82. This research was supported by the office Basic Energy Science, Materials Science Division.

Reference:

1. Driskell TD, Hassler CR, McCoy LR. Significance of resorbable bioceramics in the repair of bone defects. Proceedings of the Annual Conference on Engineering in Medicine and Biology; 1973; 1973. p. 199.

2. Metsger DS, Driskell TD, Paulsrud JR. Tricalcium phosphate ceramic-a resorbable bone implant: review and current status. J Am Dent Assoc. 1982;105:1035-1038.

3. Klein C, Driessen AA, de Groot K, A. VDH. Biodegradation behavior of various calcium phosphate materials in bone tissue. J Biomed Mater Res. 1983;17:769-784.

4. Whittaker JM, James RA, Lozada J, Cordova C, GaRey DJ. Histological response and clinical evaluation of heterograft and allograft materials in the elevation of the maxillary sinus for the preparation of endosteal dental implant sites. Simultaneous sinus elevation and root form implantation: an eight-month autopsy report. J Oral Implant. 1989;15:141-144.

5. Hollinger JO, Battistone GC. Biodegradable bone repair materials. Synthetic polymers and ceramics. Clin Orthop. 1986;207:290-305.

6. Jarcho M. Calcium phosphate ceramics as hard tissue prosthetics. Clinical Orthopaedics and Related Research 1981;157:259-278.

7. Park JB, Lakes RS. Biomaterials: An Introduction 2nd ed. New York: Plenum Publishing, 1992.

8. Aoki H. Medical Applications of Hydroxyapatite. St. Louis: Smyaku Euro Americ, 1994.

9. Ducheyne P, Radin S, King L. The effect of calcium phosphate ceramic composition and structure on in vitro behavior. I. Dissolution. Journal of Biomedical Material Research 1993;27:25-34.

10. Langstaff S, Sayer M. Resorble bioceramics based on stabilized calcium phosphates. Part II: evaluation of biological response. Biomaterials 2001;22:135-150.

11. Manjubala I. preparation of biphasic calcium phosphate doped with magnesium fluoride for osteoporotic applications. J Mater Sci letter 2001;20:1225-1227.

12. Koutsoukos PG. Influence of metal ions on the crystal growth of calcium phosphate. Boston: Kluwer academic publishers, 1998.

13. Ito A. Resorbability and solubility of zinc-containing tricalcium phosphate. J Biomed Mater Res. 2002;60:224-231.

14. Ito A. Preparation, solubility, and cytocompatibility of zinc-releasing calcium phosphate ceramics. J Biomed Mater Res. 2000;50:178-183.

15. Gibson IR, Best SM, Bonfield W. Chemical characterization of silicon-substituted hydroxyapatite. J biomed Mater Res. 1999;44:422-428.

16. Ruys AJ. Silicon-doped hydroxyapatite. Journal of Australian Ceramic Society 1993;29:71-80.

17. Serre CM, Papillard M, Chavassieux P, Voegel JC, Boivin G. Influence of magnesium substitution on a collagen–apatite biomaterial on the production of a calcifying matrix by human osteoblasts. J Biomed Mater Res, 1998;42:626–633.

18. Bigi A, Foresti E, Gregorini R, Ripamonti A, Roveri N, Shah JS. The role of magnesium on the structure of biological apatites. Calcified Tissue International 1992;50(5):439-444.

19. Xie D, Feng D, Chung I-D, Eberhardt AW. A hybrid Zinc-calcium-silicate polyalkenoate bone cement. Biomaterials 2003;24:2794-2757.

20. Mayer I, Cuisinier FJG, Popov I, Schleich Y, Gdalya S, Burghaus O, et al. Phase Relations Between β-Tricalcium Phosphate and Hydroxyapatite with Manganese(II): Structural and Spectroscopic Properties. European Journal of Inorganic Chemistry 2006;7:1460-1465.

21. Wei X, Akinc M. Crystal structure analysis of Si, Zn-modified Tricalcium phosphate by Neutron Powder Diffraction. To be submitted.

22. Schroeder LW, Dickensand B, Brown. WE. Crystallographic Studies of the Role of Mg as a Stabilizing Impurity in β-tricalcium phosphate: II. Refinement of Mg-containing β-tricalcium phosphate. J Solid State Chemistry 1977;22:253-262.

23. Elliott JC. Structure and Chemistry of the Apatites and other Calcium Orthophosphates. London: Elsevier, 1994.

24. Saint-Jean SJ, Camire CL, Nevsten P, Hansen S, Ginebra MP. Study of the reactivity and in vitro bioactivity of Sr-substituted α-TCP cements. Journal of Materials Science: Materials in Medicine 2005;16(11):993-1001.

25. Yoshikawa M, Toda T. Reconstruction of Alveolar Bone Defect by Calcium Phosphate Compounds. Journal of biomedical materials research 2000;53(4): 430-437.

26. Kurashina K, Kurita H, Hirano M, de Blieck JMA, Klein CPAT, de Groot K. Calcium phosphate cement: in vitro and in vivo studies of the α-tricalcium phosphate-dicalcium

phosphate dibasic-tetracalcium phosphate monoxide system. Journal of Materials Science: Materials in Medicine 1995;6(6):340-347.

27. Kurashina K, Kurita H, Hirano M, Kotani A, Klein CPAT, de Groot K. In vivo study of calcium phosphate cements: implantation of an α-tricalcium phosphate/dicalcium phosphate dibasic/tetracalcium phosphate monoxide cement paste. Biomaterials 1997;18(7):539-543.

28. Kurashina K, Kurita H, Kotani A, Kobayashi S, Kyoshima K, Hirano M. Experimental cranioplasty and skeletal augmentation using an α-tricalcium phosphate/dicalcium phosphate dibasic/tetracalcium phosphate monoxide cement: a preliminary short-term experiment in rabbits. Biomaterials 1998;19(7-9):701-706.

29. Kurashina K, Kurita H, Kotani A, Takeuchi H, Hirano M. An in vivo study of alpha-TCP/DCPD/TECP cement in rabbit mandibles. Bioceramics, Proceedings of the International Symposium on Ceramics in Medicine 1996;9:259-261.

30. Kurashina K, Kurita H, Kotani A, Takeuchi H, Hirano M. In vivo study of a calcium phosphate cement consisting of α-tricalcium phosphate/dicalcium phosphate dibasic/tetracalcium phosphate monoxide. Biomaterials 1997;18(2):147-151.

31. Kurashina K, Kurita H, Takeuchi H, Hirano M, Klein CPAT, de Groot K. Osteogenesis in muscle with composite graft of hydroxyapatite and autogenous calvarial periosteum: a preliminary report. Biomaterials 1995;16(2):119-123.

32. Wei X, Akinc M. Si,Zn-modified tricalcium phosphates: A phase composition and crystal structure study. Key Engineering Materials 2005;284-286:83-86.

33. Wei X, Akinc M. Resorption Rate Tunable Bioceramic: Si&Zn-Modified Tricacium Phosphate. In: Mizuno M, editor. Ceramic Engineering and Science Proceedings (the 29th International Conference on Advanced Ceramics and Composites - Advances in Bioceramics and Biocomposites). Cocoa Beach, FL: The American Ceramic Society, 2005. p. 129 - 136.

34. Barrea RA, Perez CA, Ramos AY. Zinc incorporation in human dental calculus. J Synchrotron Rad 2001;8:990-992.

35. Walsh PM, O'Connor JM, Strain JJ. The role of trace elements in bone health. Nutritional Aspects of Bone Health 2003:351-368.

36. Nielsen FH. Ultratrace elements in nutrition. Annual Review of Nutrition 1984; 4:21-41.

37. Carlisle EM. Silicon: a requirement in bone formation independent of vitamin D. Calcif Tissue Int 1981;33(1):27-34.

38. Olson RE, Doisy AA. Clinical nutrition, an interface between human ecology and internal medicine. Nutrition Reviews 1978;6:161-178.

39. Carlisle EM. A silicon requirement for normal skull formation in chicks. The Journal of nutrition 1980;110(2):352-359.

40. Tas AC. Synthesis of biomimetic Ca-hydroxyapatite powders at 37C in synthetic body fluids. Biomaterials 2000;21:1429-1438.

41. Ulreich JB. In vitro toxicity testing: a quantitative microassay. Philadelphia: ASTM, 1983.

42. Christoffersen J. Kinetics of dissolution of calcium hydroxyapatite. Journal of Crystal Growth 1980;49:29-44.

43. Driessens F. Formation and stability of calcium phosphate in relation to the phase composition of the mineral in calcified tissues. Boca Raton: CRC Press, 1983.

44. Wei X, Ugurlu O, Akinc M. Hydrolysis of α-Tricalcium Phosphate in Simulated Body Fluid at 37°C. to be submitted.

45. Termine JD, Peckauskas RA, Posner AS. Calcium phosphate formation in vitro. II. Effects of environment on amorphous-crystalline transformation. Arch Biochem Biophys 1970;140:318.

46. Eanes ED, Termine JD, Nylen MU. Electron microscopic study of the formation of amorphous calcium phosphate and its transformation to crystalline apatite. Calcified Tissue Research 1973;12(2):143-158.

47. Meyer JL, Eanes ED. A thermodynamic analysis of the secondary transition in the spontaneous precipitation of calcium phosphate. Calcified Tissue Research 1978;25(3):209-216.

48. Meyer JL, Eanes ED. A thermodynamic analysis of the amorphous to crystalline calcium phosphate transformation. Calcified Tissue Research 1978;25(1):59-68.

49. Mathew M, Schroeder L, Dickens B, Brown W. The crystal structure of α-Ca3(PO4)2. Acta Cryst 1977;B33:1325-1333.

50. Ducheyne P, Radin S. London: Butterworth-Heinemann, 1991.

51. Bigi A. Inhibiting effect of zinc on hydroxylapaite crystallization. Journal of Inorganic Biochemistry 1995;58:49-58.

52. Klein CPAT. A comparative study of different whitlockite ceramics in rat cortical bone with regard to their biodegradation behavior. Biomaterials 1986;7:144-146.

53. Yin X, Stott MJ. Theoretical insights into bone grafting silicon-stabilized α-tricalcium phosphate. Journal of Chemical Physics 2005;122(2):024709.

54. Nurse RW, Welch JH, Gutt W. High-temperature phase equilibria in the system dicalcium silicate-tricalcium phosphate. Journal of the chemical society 1959:1077-1083.

55. Kreidler E, Hummel F. Phase relationships in the system SrO-P_2O_5 and the influence of water vapor on the formation of Sr4P2O9. Inorg Chem. 1967;6:884-891.

Table 1. Samples used in the dissolution study

Powder name	Phase(s)	Zn* Content (%)	Si* Content (%)
α-TCP		—	—
β-TCP		—	—
α-/β-TCP	60%α-TCP / 40%β-TCP	—	—
Si-5	96%α-TCP / 4%Calcium Silicates	0	5
Zn-5	3%α-TCP / 97%β-TCP	5	0
Si,Zn-3	65%α-TCP / 35%β-TCP	3	3
Si,Zn-5	20%α-TCP / 80%β-TCP	5	5
Si,Zn-10	100%β-TCP**	10	10

* Zn content: 5% means $^{Zn}/_{Zn+Ca} = 5\%$ Si content: 5% means $^{Si}/_{Si+P} = 5\%$

** The second phase in Si,Zn-10 was not detected by XRD in this study

Table 2. Ion concentration s of SBF solution and human plasma

Ion	SBF (mM)	Human Plasma (mM)
Na	142.0	142.0
Cl^-	125.0	103.0
HCO_3^-	27.0	27.0
K^+	5.0	5.0
Mg^{2+}	1.5	1.5
Ca^{2+}	2.5	2.5
HPO_4^{2-}	1.0	1.0
SO_4^{2-}	0.5	0.5

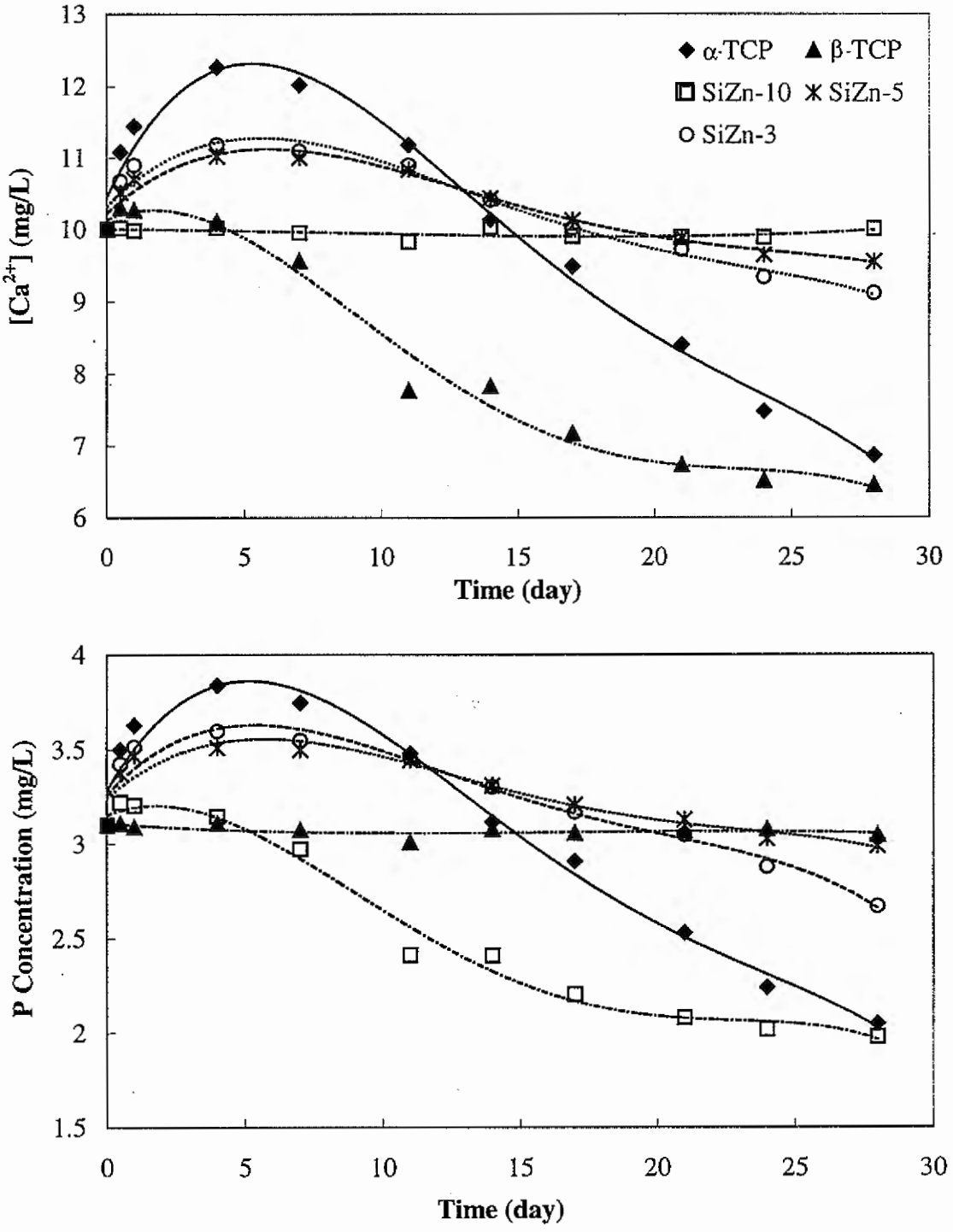

Figure 1 Ca and P concentration in SBF as the function of time, including sample α-TCP, β-TCP, Si,Zn-3, Si,Zn-5 and Si,Zn-10. Solution have been dilute 10 times for chemical analysis. The standard error of each point is within 5%.

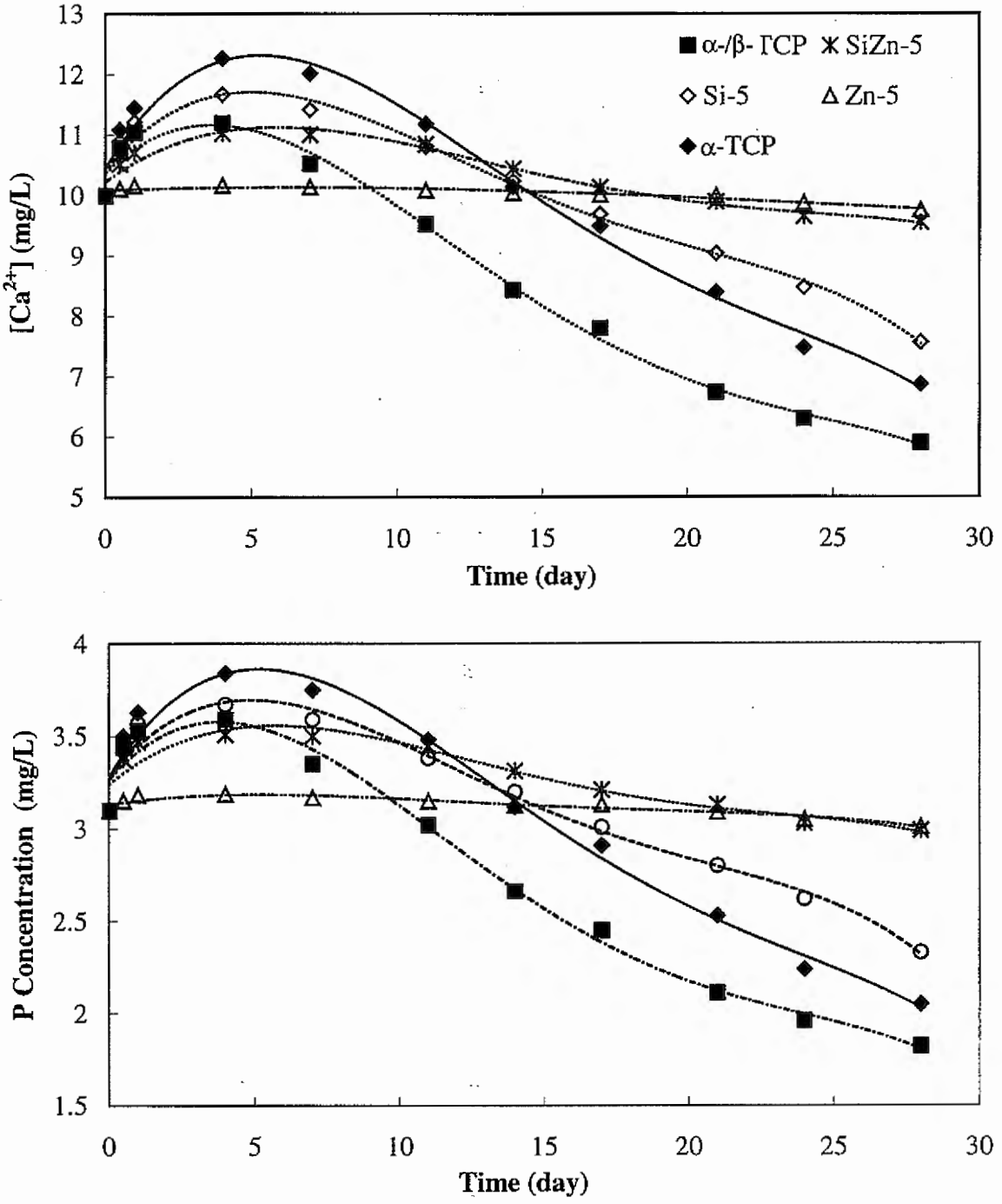

Figure 2 Ca and P concentration in SBF as the function of time, including sample α-TCP, Si-5, Zn-5, Si,Zn-5 and α-/β-TCP. Solution have been dilute 10 times for chemical analysis. The standard error of each point is within 5%.

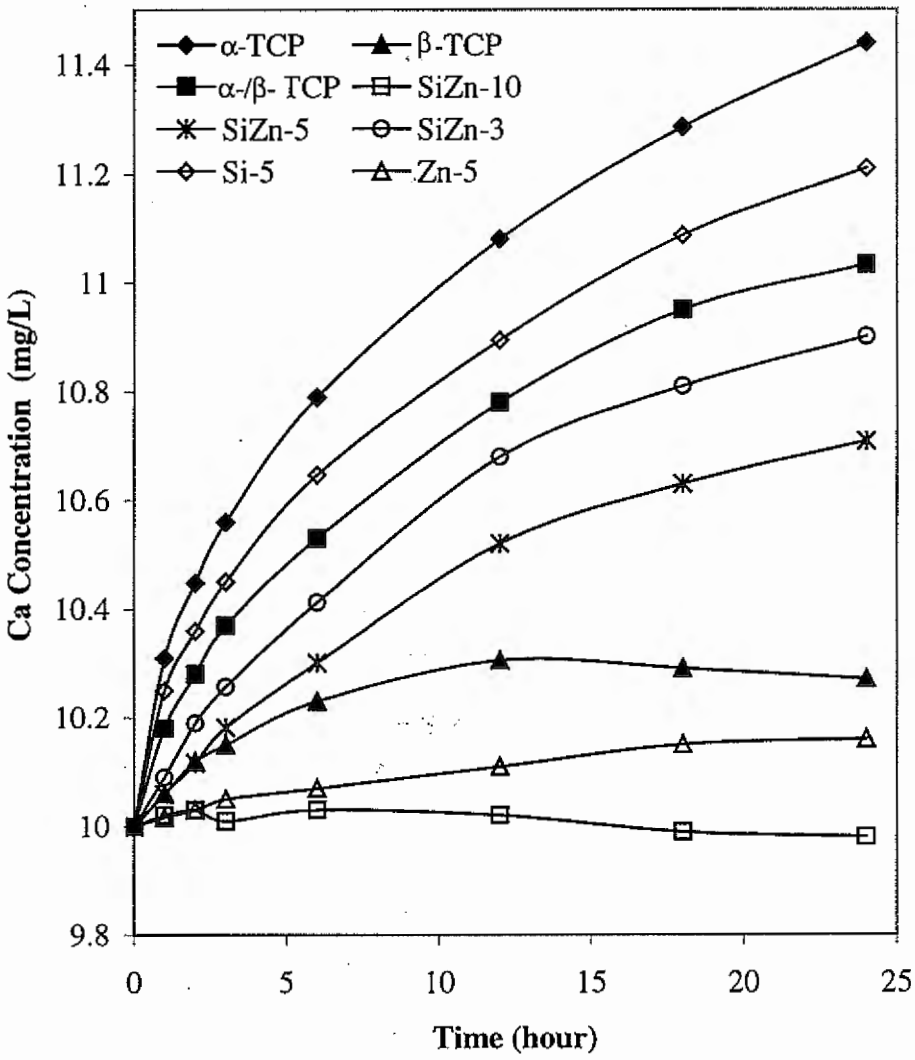

Figure 3 Variation of Ca concentration in SBF with time for the first 24 hours. The standard error of each point is within 5%.

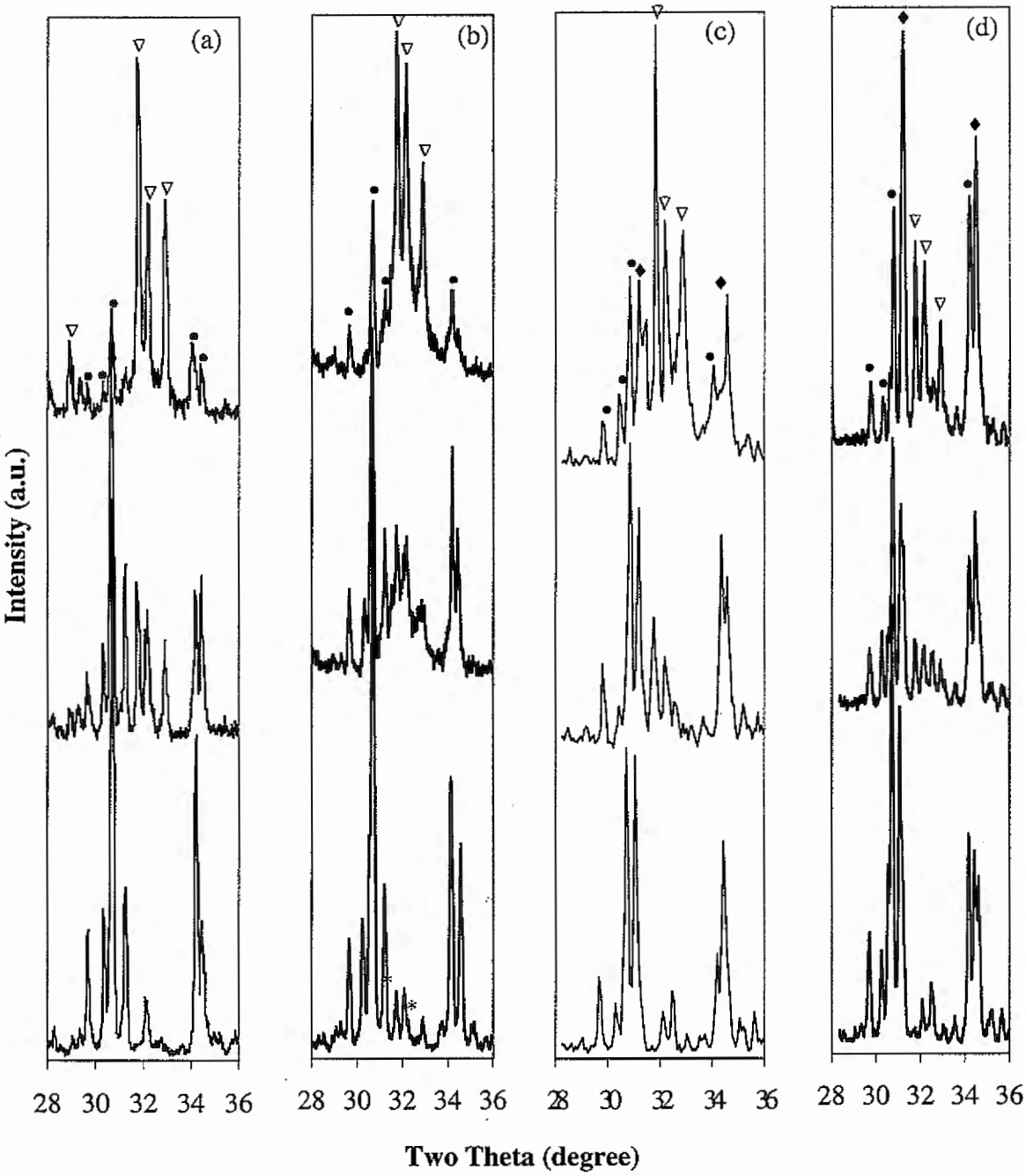
(a)
(b)
(c)
(d)
Intensity (a.u.)
28 30 32 34 36
28 30 32 34 36
28 30 32 34 36
28 30 32 34 36
Two Theta (degree)

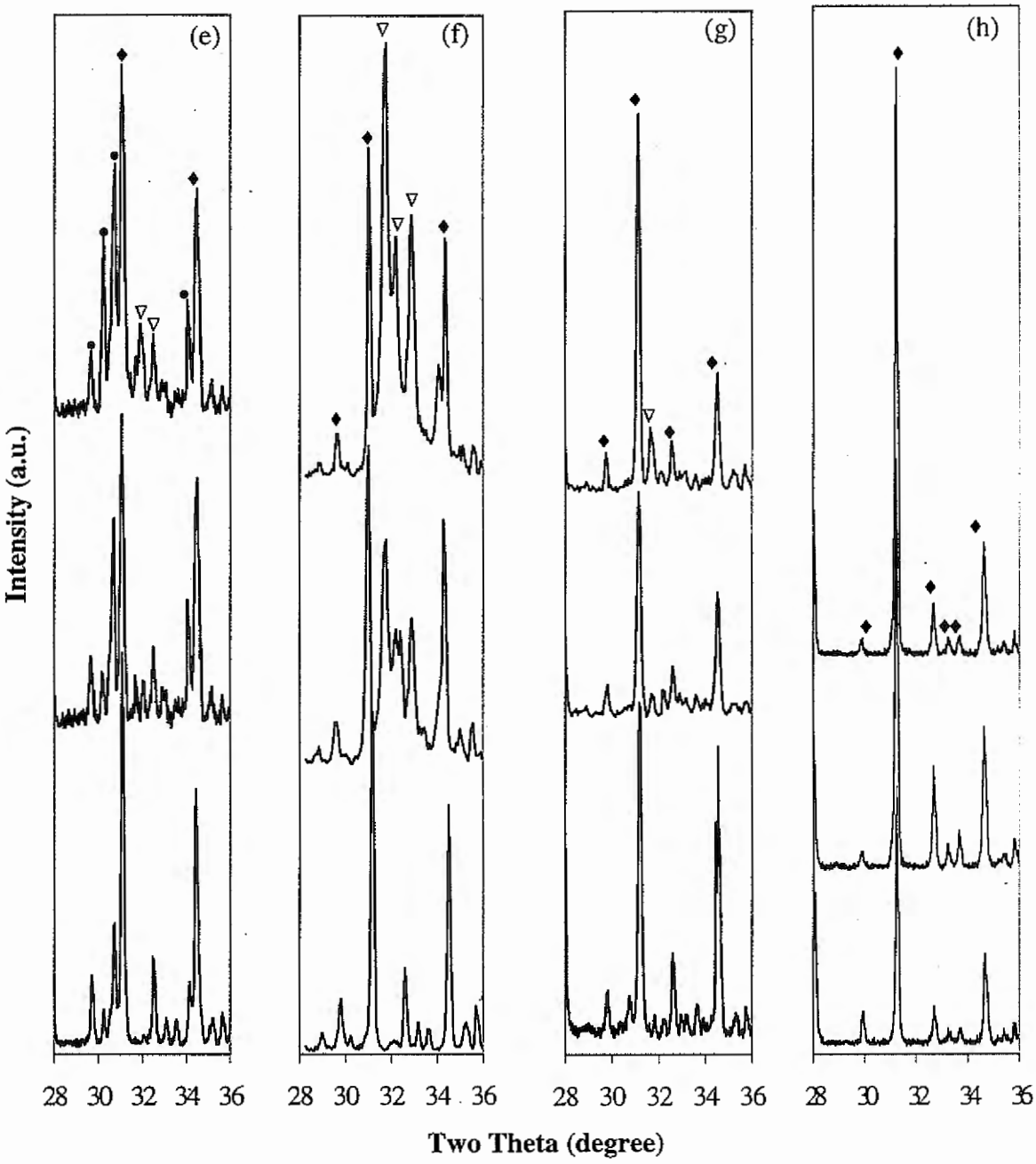

Figure 4 X-ray diffraction patterns of samples before (lower curve) and after immersion in SBF two weeks (middle curve) and four weeks (upper curve). (a) α-TCP; (b) Si-5; (c) α-/β-TCP; (d) Si,Zn-3; (e) Si,Zn-5; (f) β-TCP; (g) Zn-5; (h)Si,Zn-10. ∇ HAp phase; • α phase; ♦ β phase; * Calcium Silicates

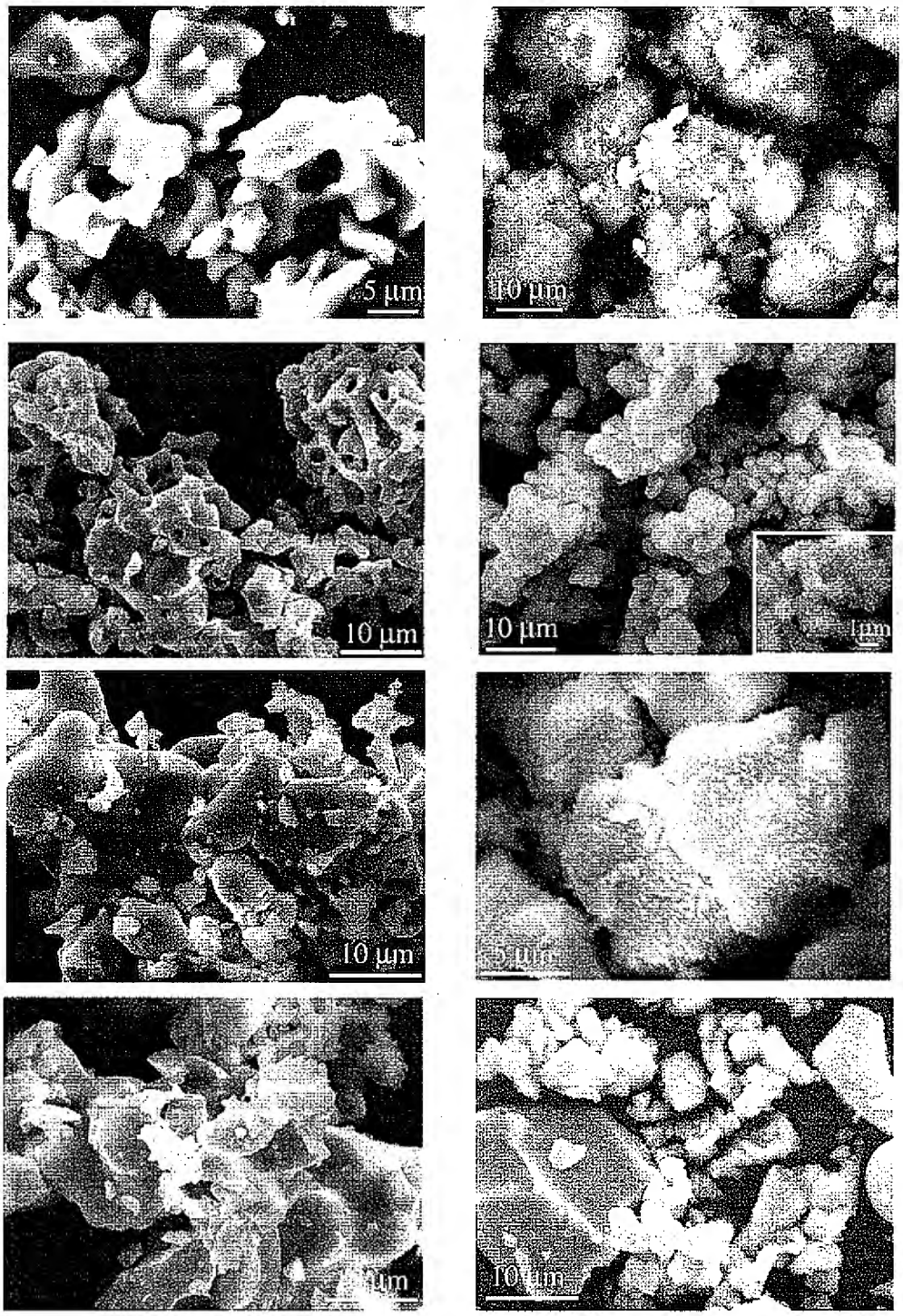
5 µm
10 µm
(a)
10 µm
10 µm
1µm
(b)
10 µm
5 µm
(c)
µm
10 µm
(d)

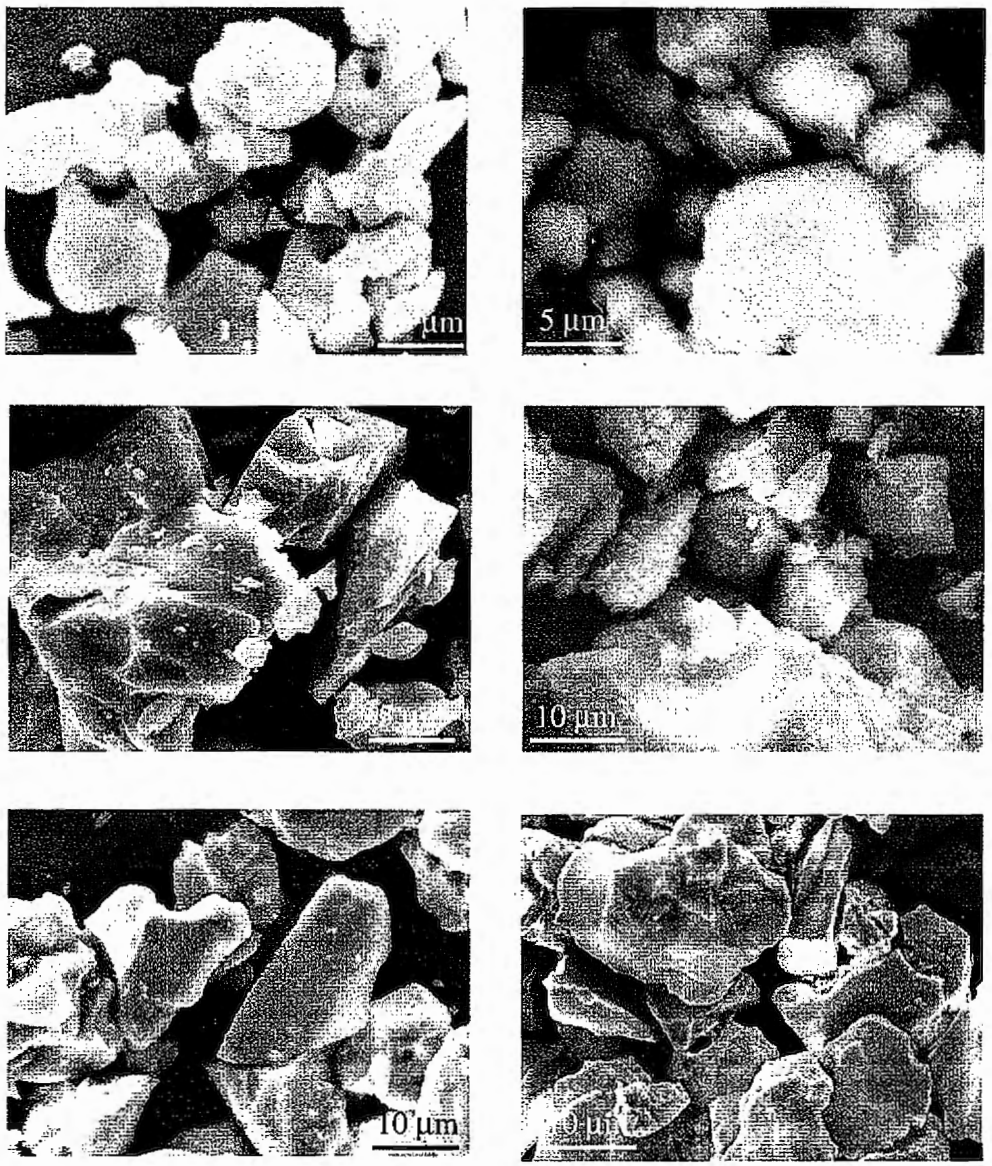

Figure 5 Scanning electron micrographs of samples before and after aging in SBF four weeks. (a) α-TCP; (b) Si-5, inserted high magnification image at corner; (c) Si,Zn-3; (d) Si,Zn-5; (e) β-TCP; (f) Zn-5; (g) Si,Zn-10

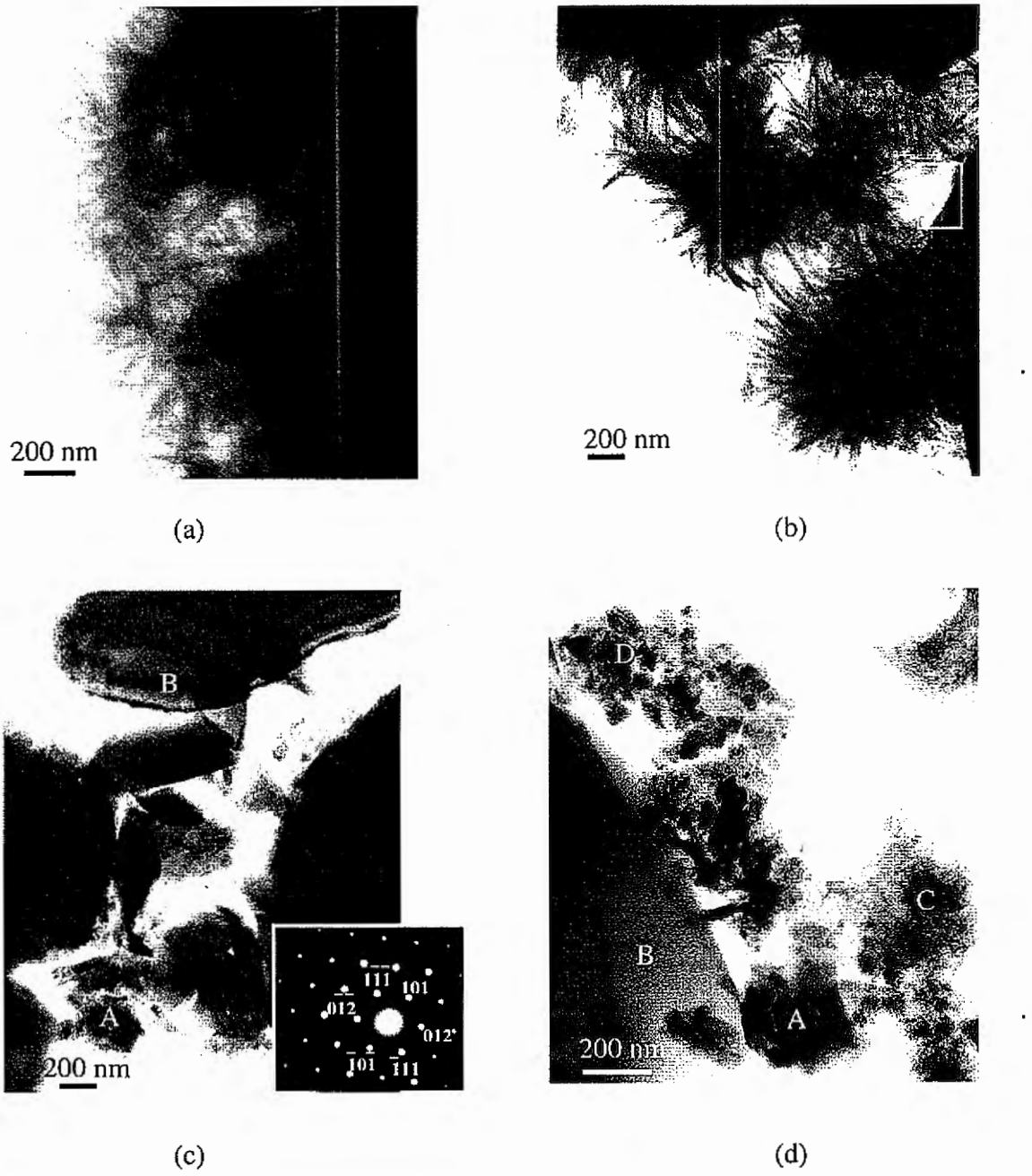

Figure 6 α-TCP and Si,Zn-3 before and after immersion in SBF (a) α-TCP after two weeks (b) α-TCP after four weeks. Highlighted area shows the uncovered area by HAp, indicating that the dissolution of α-TCP could continue even after four weeks. (c) Si,Zn-3 as synthesized. The inserted SAD is β phase along $[\bar{1}2\bar{1}]$ zone axis.; (d) Si,Zn-3 after four weeks, where A is the α phase, B is β phase, C is HAp precipitation with characteristic needle-shape crystal radiant from the center , and D may be the HAp phase at the initial crystallization stage. More morphology details are shown in Figure 8.

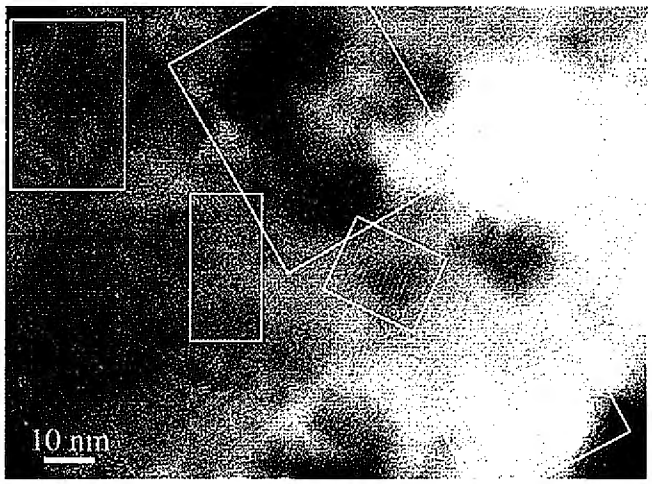

(a)

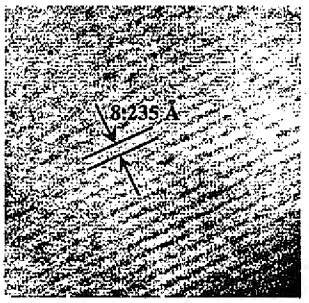

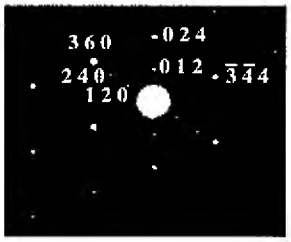

(b)

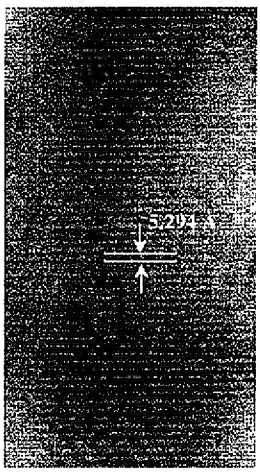

(c)

Figure 7 High magnification image of α phase in Si,Zn-3 (Figure 7a). Highlighted areas are some grains with two major plane spacings. (b) Higher-resolution image of the bottom section of the grain with a plane spacing of 8.235 Å, matching $(\bar{1}20)$ plane of α phase. The indexed SAD was taken from this grain and the zone axis is $[\bar{4}2\bar{1}]$; (c) High-resolution image of the grain in the middle section with a lattice spacing of 5.294 Å, a half of d-spacing of (100) plane. Compared with pure α-TCP, the slight variance of spacing is due to Zn and Si substitution for Ca and P sites.

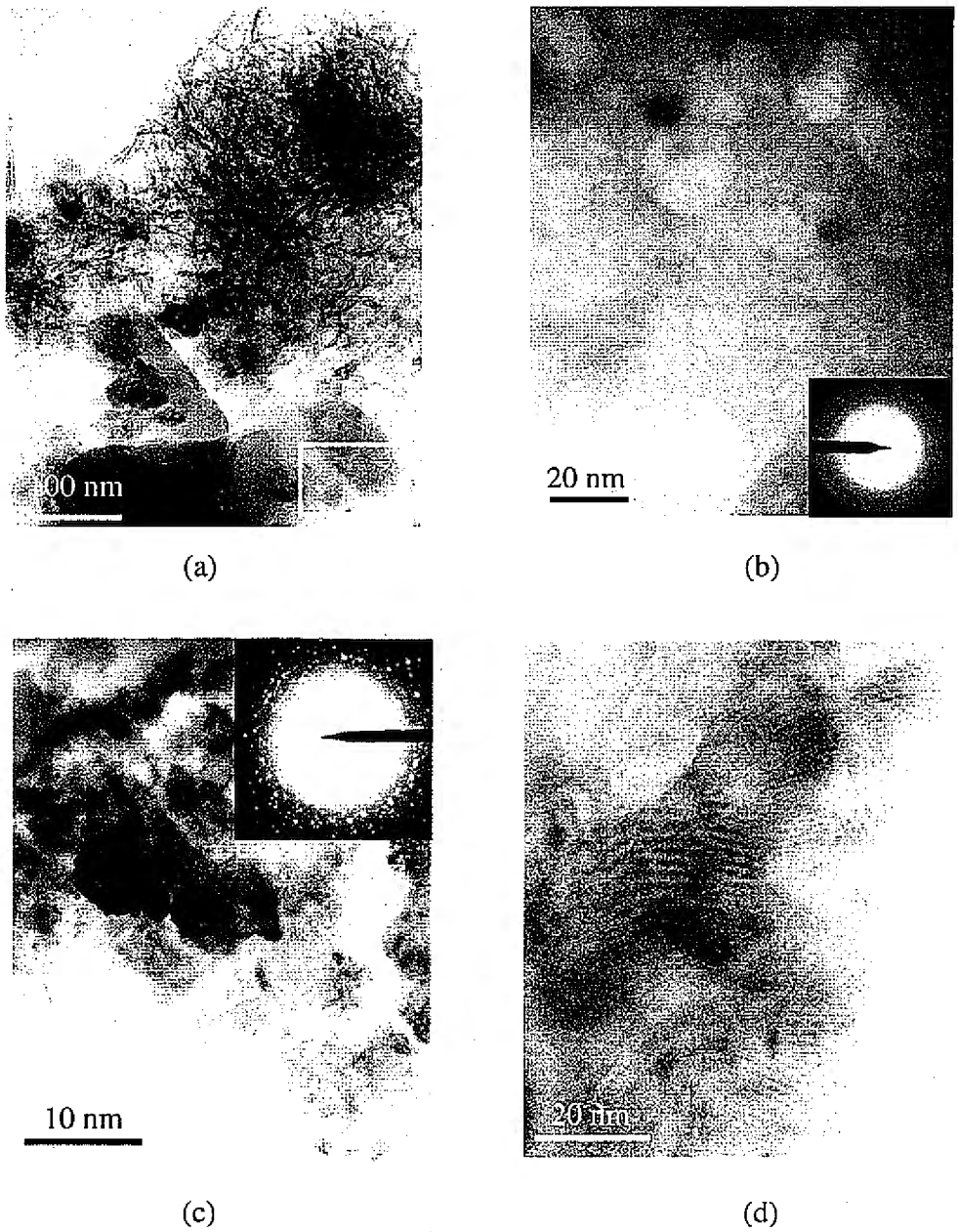

Figure 8 High magnification image in Si,Zn-3 (Figure 7b). (a) B and C areas in Figure 7b; (b) High resolution image of the highlight area in (a). SAD shows broad rings, characteristic of amorphous and nano-size materials; (c) D area high-resolution image and SAD pattern, showing the polycrystalline structure; (d) High-resolution image of the grain in the middle section.

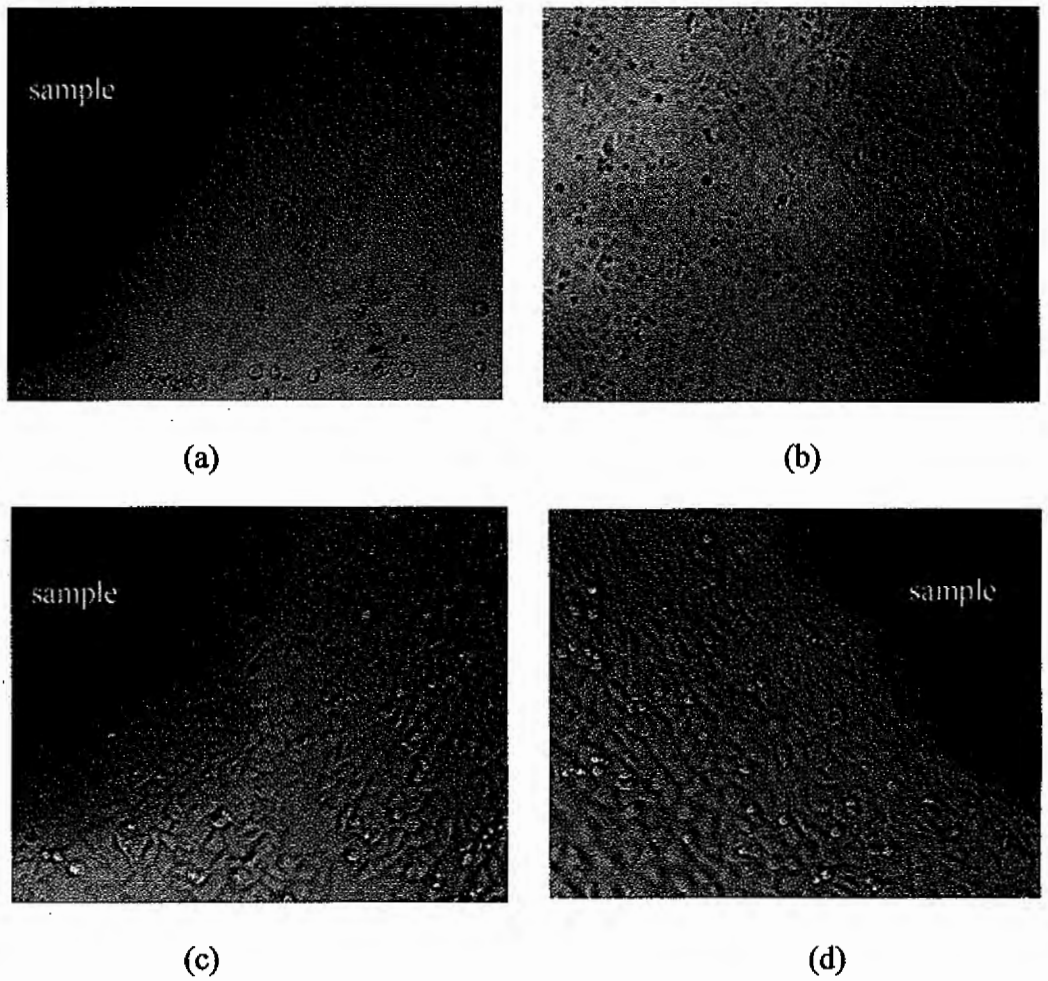

Figure 9 SKOV3 cells after direct contact cytotoxicity testing (100×). (a) Positive control, ZnO; (b) Negative control, No sample (c) Si,Zn-3 sample; (d) Si,Zn-10 sample

CHAPTER 6:
HYDROLYSIS OF α-TRICALCIUM PHOSPHATE IN SIMULATED BODY FLUID AND DEHYDRATION BEHAVIOR DURING DRYING PROCESS

A manuscript to be submitted to *Biomaterials*

Xiang Wei, Ozan Ugurlu and Mufit Akinc*

Department of Materials Science and Engineering and Ames Laboratory, Iowa State University, Ames, IA 50011, USA.

* Email: makinc@iastate.edu

Abstract

The hydrolysis of α-TCP in simulated body fluid (SBF) at 37°C was investigated. Concentration of ions in simulated body fluid (SBF) was monitored by ICP. The hydration rate was found to be slower in SBF than that in deionzed water. The hydrolysis product was carbonate-containing calcium-deficient hydroxyapatite incorporated with Mg^{2+}, Na^{+} and Cl^{-} ionic impurities, which was characterized by XRD, SEM, TEM, FTIR and XPS. An amorphous layer on the α-TCP surface was found to be the precursor of apatite phase, which may lead to either crystalline apatite or can decompose back to α-TCP at lower temperature.

Key words: α-Tricalcium Phosphate, Hydrolysis, Simulated Body Fluid, Calcium-deficient hydroxyapatite, amorphous hydroxyapatite

I. Introduction

Hydroxyapatite ($Ca_{10}(PO_4)_6(OH)_2$, HAp) has been investigated extensively as an implant material for bones and teeth since the 1970s. One of the reasons for its good biological performance is the similarity to the mineral phase of bone, which is mainly a carbonate-containing apatite with many other ionic impurities. However, HAp fabrication method, usually sintering at high temperature, represents a significant drawback for these

materials, since it limits their shape and size. This often causes problems of adaptation and fixation to the bone cavities where they had to be placed. Moreover, stoichiometric HAp is too stable to be resorbed during bone remodeling process [1].

In 1983, Brown and Chow[2] demonstrated the formation of hydroxyapatite in a monolithic form at room or body temperature by means of a cementitious reaction. This material was moldable and could adapt to the bone cavity. Bonding with bone will finally be realized through the converted apatite phase. It presented a good fixation and an optimum tissue–biomaterial contact, necessary for stimulating bone ingrowth. Thus, hydrolysis became one of the most important synthesis methods for HAp. A number of studies established that slightly water-soluble calcium phosphates [e.g., dicalcium phosphate ($CaHPO_4$, DCPA), dicalcium phosphate dehydrate ($CaHPO_4{\cdot}2H_2O$, DCPD), α-tricalcium phosphate (α-$Ca_3(PO_4)_2$, α-TCP), and octacalcium phosphate ($Ca_8H_2(PO_4)_6{\cdot}5H_2O$, OCP)] can convert to HAp in moderate to high pH solution [3-8].

Among them, α-TCP is particularly attractive for several reasons. It is most reactive in an aqueous system due to its high solubility. It utilizes a single precursor and forms various reaction products. DCPD is the reaction product below pH 5.5, OCP forms at pH 5.5–7.5, and HAp above pH 7.5 [3, 9, 10]. The HAp produced by this cement-type reaction may exist over a compositional range and can be characterized in terms of its Ca/P ratio, which is called calcium-deficient HAp (CDHAp or $Ca_{10-x}(HPO_4)_x(PO_4)_{6-x}(OH)_{2-x}$) where x ranges from 0 to 1: x= 0 for stoichiometric HAp and x=1 for fully CDHAp[11]. These "nonstoichiometric" HAp compositions are more soluble than stoichiometric HAp. It may be incorporated into bone more readily by osteocytes. The hydrolysis of α-TCP also results in carbonate-containing HAp($Ca_{10}(PO_4)_6(CO_3)_x(OH)_{2-2x}$) based on the composition of the aqueous solution.

Monma et al. first reported that the α-TCP converts to CDHAp in water below 100°C at pH values ranging from 8.1 to 11.4 [7, 11]. Durucan and Brown examined the transformation kinetics of HAp formation by direct hydrolysis of α-TCP at several temperatures [3]. The reaction completed in 18h at 37°C in de-ionized water. XRD analysis accompanied by FTIR confirmed that phase pure CDHAp was formed. Li et al studied α-TCP hydrolysis in deionized water at 80°C. They proposed a formula for the converted

apatite-TCP phase containing lattice water and a partial structural model along the hydroxyl column[6]. TenHuisen et al developed sodium and fluoride containing HAp based on the hydrolysis of α-TCP in NaF solutions[8]. Monma et al. also found that extent of conversion was retarded in the presence divalent inorganic salts, whereas monovalent inorganic or organic salts favored hydration[12]. The better mechanical properties and accelerated reaction rates was obtained in NaCl solution[3, 13].

Although the hydrolysis reactions of α-TCP in water[14, 15] and in other solutions[12, 16] have been characterized, the reaction in SBF solution appears not to have been fully studied. Since SBF solution mimics the human plasma composition, the hydrolysis product may be similar in composition to the bone mineral. In addition, it is well known that hydration is strongly influenced by the solution composition. It is necessary to understand the hydrolysis reaction of α-TCP that takes into consideration of the complex composition of the SBF. The purpose of this work is to study α-TCP reaction in the simulated body fluid, and phase transformation during the immersion and drying process (dehydration behavior). It also provides the benchmark result for the dissolution behavior of Si,Zn-doped tricalcium phosphate in SBF [17].

II. Materials and Method

α-TCP was formed according to following solid state reactions:

$$2NH_4H_2PO_4 + 3CaCO_3 = Ca_3(PO_4)_2 + 3H_2O + 3CO_2 + 2NH_3 \quad (1)$$

The commercial reagent grade $CaCO_3$ and $NH_4H_2PO_4$ (Fisherscientific, Hampton, NH) were used as received. The stoichiometric mixture of the starting powders was first milled in anhydrous ethanol for 4h using alumina media. The slurries were vacuum filtered. The precursor powder were then fired in alumina combustion boat in an open atmosphere furnace at 1300°C for 6 hours and quenched in dry air. The final powder was ground using an alumina mortar and pestle, and stored in the desiccator. The chemical analysis was performed by the ICP (Thermo Jarrell-Ash AtomScan 16, Thermo Elemental, Waltham, MA).

The α-TCP powder was immersed in the simulated body fluid (SBF), which was prepared according to Bayraktar and Tas [18]. The solid to solution ratio was set at 1:50 g/mL. The glass bottles were sealed and kept in a water bath shaker at a constant temperature

of 37°C. The pH of the solution was measured with an accuracy of ±0.02. After setting time, suspensions were centrifuged. Calcium and phosphorous concentrations of clear solution was measured by ICP. The solid was quickly washed by de-ionized water and dried in a convection oven or a vacuum system. The oven temperature was set at 100°C and samples were deied for two days.

X-ray powder diffraction analyses were performed by a Scintag diffractometer (Scintag X1, Cupertino, CA) with Cu Kα radiation. An accelerating voltage 45kV and a current of 40 mA were used. The XRD data were collected over 2θ range of 10-40° at a step size of 0.02°. The surface area of the powders was determined by BET method with N_2 as the adsorbate (Quantachrome Autosorb 1, Boynton Beach, FL). The samples were outgassed about 12 hours at 100°C prior to adsorption runs. Microstructure development was observed by the scanning electron microscope (SEM) (JEOL JSM-606LV, Peabody, MA) and transmission electron microscopy (TEM) (Philips CM30, 300kV, Netherlands). The powder specimens for TEM were ground in acetone, and then collected on 200 mesh carbon-coated copper TEM grids. Electron beam transparent particles were chosen for TEM examination by selected area diffraction (SAD). Energy-dispersive X-ray spectrometer (EDS) performed in the TEM was used to confirm the elemental composition of the samples. The infrared spectra (IR) were recorded between 400 and 4000 cm^{-1} on a FTIR spectrometer (Perkin-Elmer 1600 M-80, Wellesley, MA). Pellets were prepared by homogeneously mixing about 1wt% sample into KBr matrix. The background data were collected for KBr substrate and subtracted out of each spectrum.

III. Results

ICP analysis shows that calcium, phosphor and Ca/P ratio in the synthesized α-TCP are 38.29 wt%, 19.72 wt% and 1.505 respectively, which are very close to the stoichiometric TCP composition (Ca:38.71 wt%, P: 20 wt%, Ca/P: 1.5). It confirms that the composition obtained was that expected from the starting composition. X-ray diffraction patterns for the synthesized α-TCP agrees well with the published JCPDS files (#29-395), which will be shown later with the hydrolysis products.

During four weeks immersion in SBF, the pH of the solution increased from 7.4 to 7.8. Variation of Ca and P concentration in SBF as function of soaking time is shown in Figure 1. Both Ca and P concentration increased rapidly in the first few days, reached the maximum around four days, and then decreased with further soaking. This behavior may be explained by an initial dissolution of Ca^{2+} and PO_4^{3-} followed by reprecipitation in the form of HAp at increased saturation since HAp is the most stable phase at pH>4.2. In addition, it is well known that SBF is saturated with respect to hydroxyapatite. The dissolution of α-TCP increased the supersaturation level in SBF, i.e. the driving force for the precipitation, finally leading to the formation of the apatite phase by consuming the Ca and P in the solution. The gradual transition from α-TCP to HAp surface results in the change in solubility of a α-TCP surface to a value approaching the solubility of HAp, meanwhile the dissolution rate of α-TCP decreases.

Figure 2 shows XRD patterns of the vacuum dried samples obtained by hydrolysis of α-TCP powder in SBF. Distinct peaks of HAp phases are labeled. Except HAp and α-TCP phases, no other crystalline phase appears in the hydrolysis reaction. The XRD patterns show that the HAp phase appears in the sample that hydrolyzed in one week, and the amount of HAp increases with increasing immersion time. After four weeks, the major phase of hydrolysis product is HAp, but there is still some residual α-TCP left. Compared to previous studies[3, 6-8], the hydration rate of α-TCP in SBF is much slower than in other solutions. The complex ions in SBF may affect the hydrolysis process besides the temperature effect. Based on Monma's conclusion[12], the Na^+, K^+ and Mg^{2+} ions in SBF have competitive effect on α-TCP hydration rate. That is, Na^+ and K^+ accelerate the hydration process, while Mg^{2+} decelerates the hydration rate.

The FTIR spectra of α-TCP and hydrolysis products are shown in Figure 3. The spectra of α-TCP show typical absorption bands of PO_4 vibrations at 800-1100 and 500-700 cm^{-1} (Fig. 3a). Small shoulder around 860cm^{-1} belongs to HPO_4^{2-} peak. The hydrolysis products show small hydroxyl absorption peak at 3569 cm^{-1} along with a broad band around 3500 cm^{-1} (Fig. 3b&c), which fall into the range of weakly hydrogen-bonded groups for absorbed H_2O. The carbonate bands are shown in the region of 1650 to 1300 cm^{-1} due to ν_3

vibrational mode of carbonate ion, and the peak at 873 cm^{-1} is due to the ν_2 vibrational mode. The intensities increased with increase of the immersion time. Occupancy of the ν_2 mode is considered to occur competitively between on the OH^- and carbonate groups at the interface of the growing crystal [19]. For the stoichiometric HAp, there should be a sharp OH^- absorption peak around 630 cm^{-1} on the neighboring principal PO_4^{3-} adsorption bands. However, this peak does not show in our hydrolysis product, which may be due to the formation of carbonate-containing HAp. ICP analysis for the hydrolysis solid product shows that the Ca/P ratio is 1.495, indicating that hydrolysis of α-TCP in SBF results in calcium-deficient apatite formation. According to Kuhl and Nebergall [20], this precipitated calcium-deficient carbonated HAp, named $CO_3 - CDHAp$ in this paper, can be expressed as $Ca_{10-x+y}(HPO_4, CO_3)_x(PO_4)_{6-x}(OH)_{2-x+2y}$, XPS analysis shows that this precipitated phase contains Cl^-, Na^+, and Mg^{2+} impurities on the surface (Figure 4). From the composition point of view, $CO_3 - CDHAp$ has similarity to the bone mineral.

In Figure 5, SEM micrographs show the surface morphology development of α-TCP powders in SBF. Before immersion, the hollowed out appearance of the small granules is due to occluded gaseous products during sintering according to reaction (1). In TEM micrograph (Fig. 6a), no other phase is observed on α-TCP grains before hydrolysis, and the surface is smooth. After one week immersion, the powder surface is covered by a $CO_3 - CDHAp$ layer, composed of aggregates of thin blade-like particles. With immersion time, the $CO_3 - CDHAp$ layer get thicker and the surface became appears to be covered by needle-like apatite crystals. Morphology details of the hydrolysis product are given by TEM micrographs in Figure 6. After immersion in SBF for one day, an amorphous phase layer was observed on the surface of α-TCP, with 150nm in thickness (Figure 6b). After two weeks, the $CO_3 - CDHAp$ layer consists of very fine grains with needle shape, about 1nm in width and a few tens of nanometers in length. After four weeks, α-TCP grains become smaller and $CO_3 - CDHAp$ grow into bigger fiber-like crystals, radiating from the centre out (Figure 6c). The crystal size is about 20nm in width and about 300nm in length. A selected area diffraction pattern displayed (002) arcs corresponding to 0.349 nm d-spacing along the [001]

zone axis of HAp. Slight deviation of d-spacing form standard HAp d-spacing may be due to impurities incorporation in the HAp structure. EDS analysis performed in the TEM on these crystals confirmed the presence of calcium and phosphor with the Ca/P ratio close to 1.5, consistent with ICP results. The specific surface area of the samples increased from 0.47 to 51.47m^2/g in 4 weeks due to the flaky-like crystal morphology and smaller crystal size (Table 1). It suggests that $CO_3 - CDHAp$ has a fine particle structure compared with that of TCP.

The hydrolysis products dried in the convection oven presented different surface morphology and phase composition compared to the samples dried in the vacuum system. In SEM micrographs, there are no flaky- to needle-like crystals on α-TCP surface, but some small granules for sample aged on week in SBF (Figure 7(a)), which implied that the layer formed in the solution is discontinuous at this time. The four-week aged sample had a thick, coarse and continuous layer formed on the particles surface (Figure 7(b)). Besides the amorphous phase, there is also a crystalline $CO_3 - CDHAp$ particle was found in TEM micrographs for the two-week sample (Figure 7(c)). Along the [0001] direction, SAD pattern shows that the hydrolysis product has the typical apatite six-fold hexagonal symmetry. XRD patterns show that $CO_3 - CDHAp$ content increase with ageing time, reach the maximum at two weeks, and then transform back to α-TCP again. After four weeks of immersion and then undergoing the drying process, the phase was almost pure α-TCP (Figure 8). According to the internal standard method of multiphase quantitative analysis, the distinct planes of HAp and α-TCP were chosen to compare their content in the samples by integrating peak area, shown in Table 2. This observed decomposition temperature (T≅100°) is much lower than published values for the HAp, carbonate apatite or CDHAp conversion to TCP (>450°C) [21]. The hydrolysis process in SBF may be related to this unexpected formation of α-TCP (high temperature form of TCP) at such a low temperature.

IV. Discussion

Figure 9 illustrates a schematic solubility diagram with the domains of precipitation and solubility [22]. A supersaturated solution in the labile concentration range forms a

precipitation spontaneously, and an undersaturated solution leads to the dissolution of solids. It is worth noting that a metastable solution may exist between under- and super-saturated solutions, which form no precipitate over a relatively long period. At the initial precipitation period, an "active" phase is generally formed from supersaturated solution. It is usually a very fine crystalline precipitate with a disordered lattice. This "active" phase may persist in metastable solution and may slowly transform into a more stable phase. As shown in Figure 6b, an amorphous apatite phase may be the "active" phase during α-TCP hydrolysis. There is a vast body of literatures reporting that amorphous calcium phosphate (ACP) is a transient phase during the formation of HAp in aqueous systems [23-26]. The transformation from ACP to HAp is significantly influenced by presented ions in the solution, especially Mg^{2+}. Boulet et al showed evidence from precipitation studies that Mg^{2+} ions are incorporated in the "gelatinous" precipitate of ACP [27]. Bachra et al determined a so-called precipitation diagram for the system "calcium-carbonate-phosphate" and found that in the presence of Mg^{2+} ions, the ACP phase field expanded at the expense of the CDHAp field[28]. Termine and Posner reported that the presence of Mg^{2+} ions enhanced ACP formation and retard the transformation of ACP into other calcium phosphate at a given degree of supersaturation[29, 30]. Our ICP analysis shows Mg^{2+} content in SBF decreased about 3mg/L after 4 weeks immersion of α-TCP, which indicated that Mg incorporation into the hydrolysis product. XPS analysis also shows that there are measurable amounts of Cl^-, Na^+, and Mg^{2+} impurities on the surface of precipitated apatite (Figure 4).

The phase transformation during drying process may be partially due to the amorphous phase formation and incorporation of impurities. Taken into account for ACP formation, the hydrolysis process of α-TCP takes place in four stages. The first step is the dissolution of α-TCP. Both calcium and phosphor concentration increase quickly because of the high solubility of α-TCP. The formation of ACP is the second step. It takes place when the solution became critically supersaturated with respect to HAp. At this stage, three reactions occur simultaneously: (1) continuous dissolution of α-TCP; (2) formation of ACP on α-TCP surface; (3) transformation of ACP to $CO_3 - CDHAp$ in the interface of ACP with

solution. Hydrolysis is assumed to be controlled by the available surface area for dissolution of reactant or precipitation of products [31, 32]. The dissolution of α-TCP decrease as the ACP and $CO_3 - CDHAp$ layers grow over α-TCP surface.

At the third stage, α-TCP particles are surrounded by a continuous layer of ACP and $CO_3 - CDHAp$ after two-week. Hydrolysis is controlled by diffusion of the liquid through this layer. With time, the hydrated layer becomes thicker, the diffusion of liquid through it becomes slower and becomes the rate limiting step [5]. This condition limits the further dissolution of α-TCP. However, besides precipitated from the solution, ACP may also be formed by transformation of α-TCP due to their similar structures. ACP has been proposed to consist of roughly spherical $Ca_9(PO_4)_6$ clusters, so-called Posner's clusters (PC), closely packed to form larger spherical particles with water heals in the interstices [33, 34]. In the FTIR spectrum (Figure 3), a broad H_2O peak indicates that the water moleculas may have been incorporated into the crystal lattice. Posner's cluster is a readily recognizable unit in both α- and β-TCP. In addition, ACP has a Ca/P molar ratio of 1.45±0.005, close to stoichiometric TCP. By reaction with the water, the structure of α-TCP may become disordered, and results in formation of the amorphous phase. Therefore, as long as water molecular diffuse into the α-TCP structure through the layer, ACP phase will continue to form for weeks. Since the impurities inhibit transformation of ACP to HAp, the formation of ACP may become the major reaction in SBF, while dissolution of α-TCP and transformation of ACP to HAp are limited kinetically. The solution reaches the equilibrium stage at the fourth step when Ca and P concentrations in the solution are saturated with respect to HAp. During drying in the oven, it is easy for ACP to lose interstitial water and transform back to TCP structure.

V. Conclusion

The hydration rate of α-TCP is much slower in SBF than that in the de-ionized water because the dissolution was limited by the lower surface area as the result of precipitation of hydration products on the surface. The hydrolysis products were carbonate-containing calcium-deficient hydroxyapatite ($CO_3 - CDHAp$) with Mg^{2+}, Na^+ and Cl^- ionic impurities

incorporated into the structure, which has similar composition to the biological apatite. The morphology of $CO_3 - CDHAp$ is typical thin blade- or flake-like shape. Amorphous phase forms as the initial precipitated phase during the hydrolysis, which is the precursor of $CO_3 - CDHAp$ and plays an important role in the hydrolysis process. The amorphous phase may decompose to α-TCP at low temperature. The hydrolysis product obtained in the SBF has three layers: $CO_3 - CDHAp$ is the outside layer; ACP remains as the middle layer; and α-TCP is the core. ACP layer may continuously grow at ACP/α-TCP interface through the diffusion of water molecule into α-TCP structure. The growth of $CO_3 - CDHAp$ from ACP phase is hindered by the impurities ions presented in the SBF.

Acknowledgement

We are grateful to Dr. Jim Anderegg for XPS analysis interpretation of the data. Ames Laboratory is operated for the U.S. Department of Energy by Iowa State University under contract number W-7405-ENG-82. This research was supported by the office Basic Energy Science, Materials Science Division.

References

1. Yaszem MJ, Payne RG, Hayes WC, Langer R, Mikos AG. Evolution of bone transplantation: molecular, cellular and tissue strategies to engineer human bone. Biomaterials 1996;17:175-165.

2. Brown WE, Chow LC. A new calcium phosphate setting cement. J Dent Res 1983;62:672.

3. Durucan C, Brown PW. α-Tricalcium phosphate hydrolysis to hydroxyapatite at the near physiological temperature. Journal of Materials Science: Materials in Medicine 2000;11:365-371.

4. Durucan C. Formation of hydroxyapatite by hydrolysis of alpha-tricalcium phosphate: The Pennsylvania State University; 2003.

5. Ginebra M-P, Fernandez E, Driessens F, Planell J. Modeling of the hydrolysis of α-tricalcium phosphate. J Am Ceram Soc 1999;82(10):2808-2812.

6. Li Y, Zhang X, de Groot K. Hydrolysis and phase transition of alpha-tricalcium phosphate. Biomaterials 1997;18:737-741.

7. Monma H, Ueno S, Kanazawa T. Properties of hydroxyapatite prepared by the hydrolysis of tricalcium phosphate. J Chem Tech Biotechnol 1981;31:15-24.

8. TenHuisen KS, Brown PW. Hydrolysis of α-tricalcium phosphate in NaF solutions. Biomaterials 1999;20(5):427– 434.

9. Bigi A, Boanini E, Botter R, Panzavolta S, Rubini K. α-Tricalcium phosphate hydrolysis to octacalcium phosphate: effect of sodium polyacrylate. Biomaterials 2002;23(8):1849-1854.

10. Li Y, Zhang X, de Groot K. Hydrolysis and phase transition of alpha-tricalcium phosphate. Biomaterials 1997;18(10):737-741.

11. Monma H, Kanazawa. T. The hydration of α-tricalcium phosphate. Yogio-Kyoki Shi 1976;84:209.

12. Monma H, Goto M, Kohmura T. Effect of additives on hydration and hardening of tricalcium phosphate. Gypsum & Lime 1984;188:11-16.

13. Monma H, Makishima A, Mitomo M, Ikegami T. Hydraulic properties of the tricalcium phosphate-dicalcium phosphate mixture. Nippon Seramikkusu Kyokai Gakujutsu Ronbunshi 1988;96(8):878-880.

14. Jansen J, DeRuijter J, Schaeken H, van der Waerden J, Planell J, Driessens F. Evaluation of tricalcium phosphate/hydroxyapatite cement for tooth replacement: an experimental animal study. J Mater Sci: Mater Med 1995;6:653-657.

15. Ginebra M, Fernandez E, Driessens F, Boltong M, Muntasell J, Font J, et al. The effects of temperature on the behavior of an apatitic calcium phosphate cement. J Mater Sci: Mater Med 1995;6:857-860.

16. Ginebra M, Boltong M, Fernandez E, Planell J, Driessens F. Effect of various additives and temperature on an apatitic calcium phosphate cement. J Mater Sci: Mater Med 1995;6:612-616.

17. Wei X, Ugurlu O, Akinc M. Dissolution behavior and cytotoxicity test of Si, Zn-modified tricalcium phosphate. . to be submitted.

18. Bayraktar D, Tas AC. Chemical preparation of carbonated calcium hydroxyapatite powders at 37 C in Urea-containing synthetic body fluids. Journal of Europe Ceramic Society 1999;19:2573-2579.

19. Rehman I, Bonfield W. Characterization of hydroxyapatite and carbonated apatite by photo acoustic FTIR spectroscopy. Journal of Materials Science: Matererials in Medicine 1997;8:1-4.

20. Kuehl G, Nebergall WH. Hydrogen phosphate- and carbonate apatites. Zeitschrift fuer Anorganische und Allgemeine Chemie 1963;324(5-6):313-320.

21. Elliott JC. Structure and Chemistry of the Apatites and other Calcium Orthophosphates. London: Elsevier, 1994.

22. Stumm W, Morgan JJ. Aquatic chemistry : chemical equilibria and rates in natural waters. New York: Wiley, 1996.

23. Termine JD, Eanes ED. Comparative chemistry of amorphous and apatite calcium phosphate preparations. Calcif Tissue Res 1972;10:171.

24. Eanes ED, Termine JD, Nylen MU. Electron microscopic study of the formation of amorphous calcium phosphate and its transformation to crystalline apatite. Calcified Tissue Research 1973;12(2):143-158.

25. Meyer JL, Eanes ED. A thermodynamic analysis of the secondary transition in the spontaneous precipitation of calcium phosphate. Calcified Tissue Research 1978;25(3):209-216.

26. Meyer JL, Eanes ED. A thermodynamic analysis of the amorphous to crystalline calcium phosphate transformation. Calcified Tissue Research 1978;25(1):59-68.

27. Boulte M, Marier JR, Rose D. Effect of magnesium on formation of calcium phosphate precipitates. Arch Biochem Biophys 1962;96:629.

28. Bachra BN, Trautz OR, Simon SL. A precipitation diagram for the system calcium-carbonate-phosphate and the heterogeneous nucleation of solids in the metastability region. Oxford: Pergamon Press, 1965.

29. Termine JD, Posner AS. Calcium phosphate formation in vitro. I. Factors affecting initial phase separation. Arch Biochem Biophys 1970;140:307.

30. Termine JD, Peckauskas RA, Posner AS. Calcium phosphate formation in vitro. II. Effects of environment on amorphous-crystalline transformation. Arch Biochem Biophys 1970;140:318.

31. Frank-Kamenetskii DA, Appleton AJ. Diffusion and heat transfer in chemical kinetics. 2nd ed. New York: Plenum Press, 1969.

32. Laidler KJ. Chemical Kinetics. New York: McGraw-Hill, 1965.

33. Posner AS, Betts F. Synthetic amorphous calcium phosphate and its relation to bone mineral structure. Acc Chem Res 1975;8:273-281.

34. Betts F, Posner AS. X-ray radial distribution study of amorphous calcium phosphate. Materials Research Bulletin 1974;9(3):353-360.

Table 1 Surface area of α-TCP in SBF

Immersion Time	0	1 day	1 week	2 weeks	3 weeks	4 weeks
Specific surface area (m^2/g)	0.47	6.58	19.97	24.27	32.70	51.47

Table 2 Phase composition of α-TCP hydrolysis product dried in oven at 100°C

Immersion Time	0 day	1day	1 week	2 weeks	3 weeks	4 weeks
α-TCP	90	61.4	31.4	31.5	73.3	75.4
HAp	0	28.6	78.6	78.5	16.7	14.6
Si Standard(wt%)	10	10	10	10	10	10

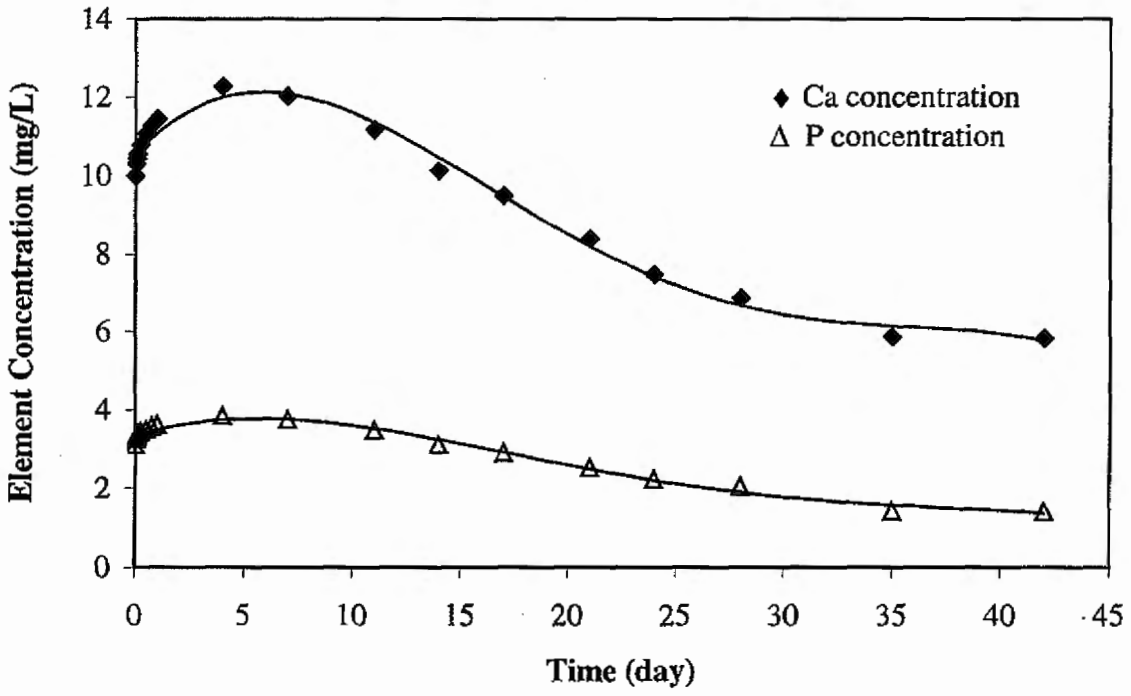

Figure 1 Ca and P concentration in SBF solution as the function of immersion time. Solution have been dilute 10 times for ICP analysis. Samples were run in triplicate for each data point. The standard error of each point is within 3%.

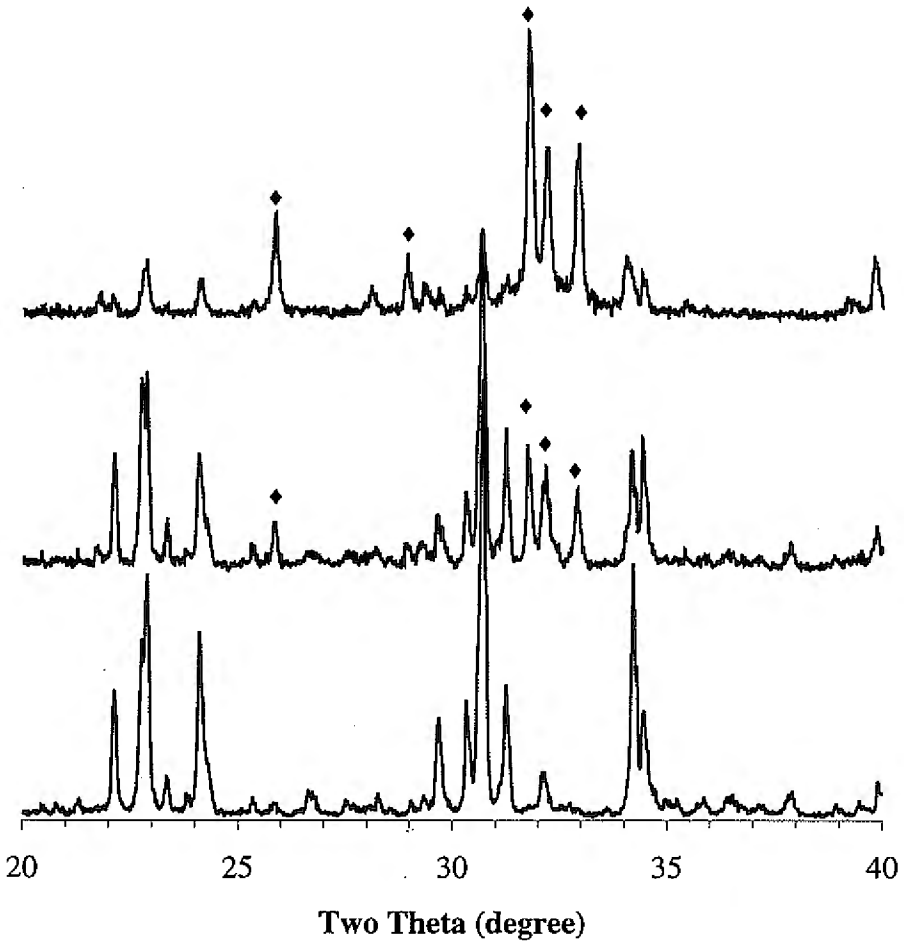

Figure 2 XRD patterns of α-TCP hydrolysis products dried in the vacuum system. The bottom line is the synthesized α-TCP; the middle line is the hydrolysis product after 2 week immersion; the upper line is the hydrolysis product after 4 weeks immersion. ♦ HAp phase

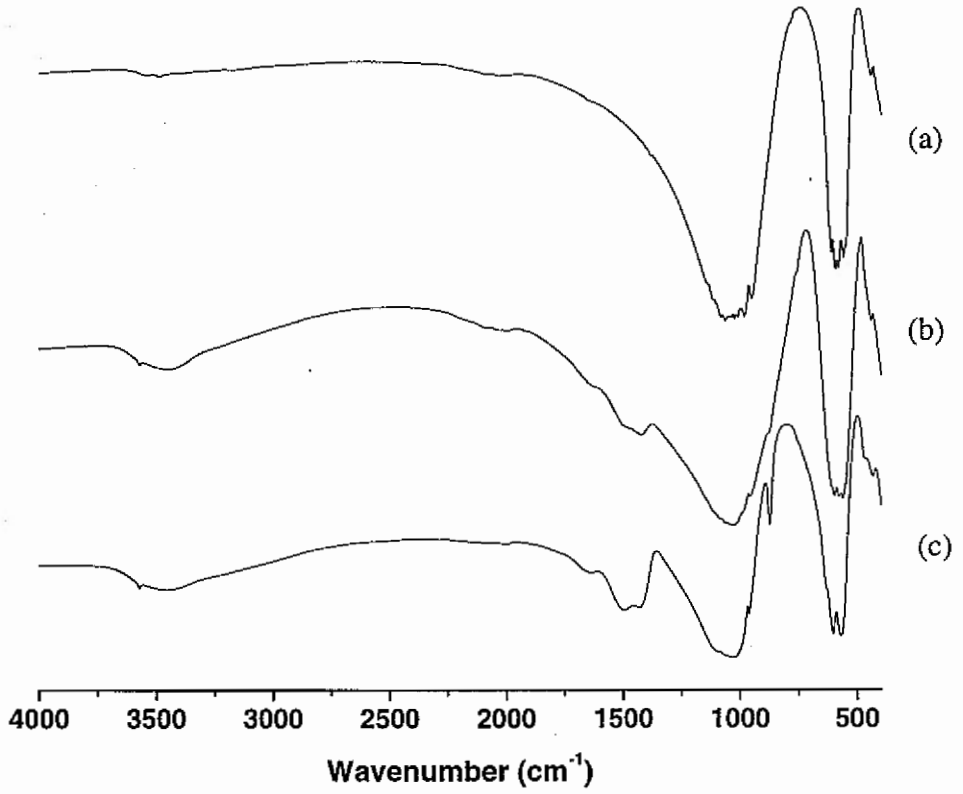

Figure 3 FTIR spectra of α-TCP and hydrolysis products. (a) synthesized α-TCP, (b) in SBF 2 week, (c) in SBF 4 weeks

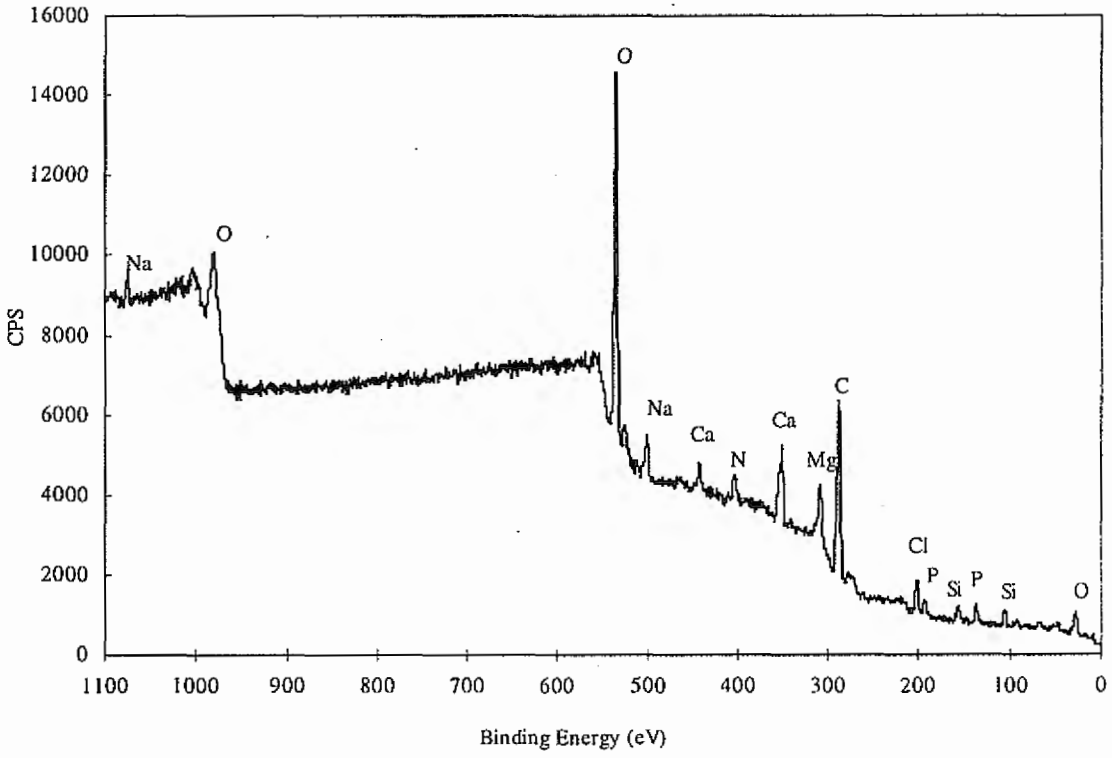

Figure 4 XPS spectra of α-TCP 4-week hydrolysis products dried in the vacuum system

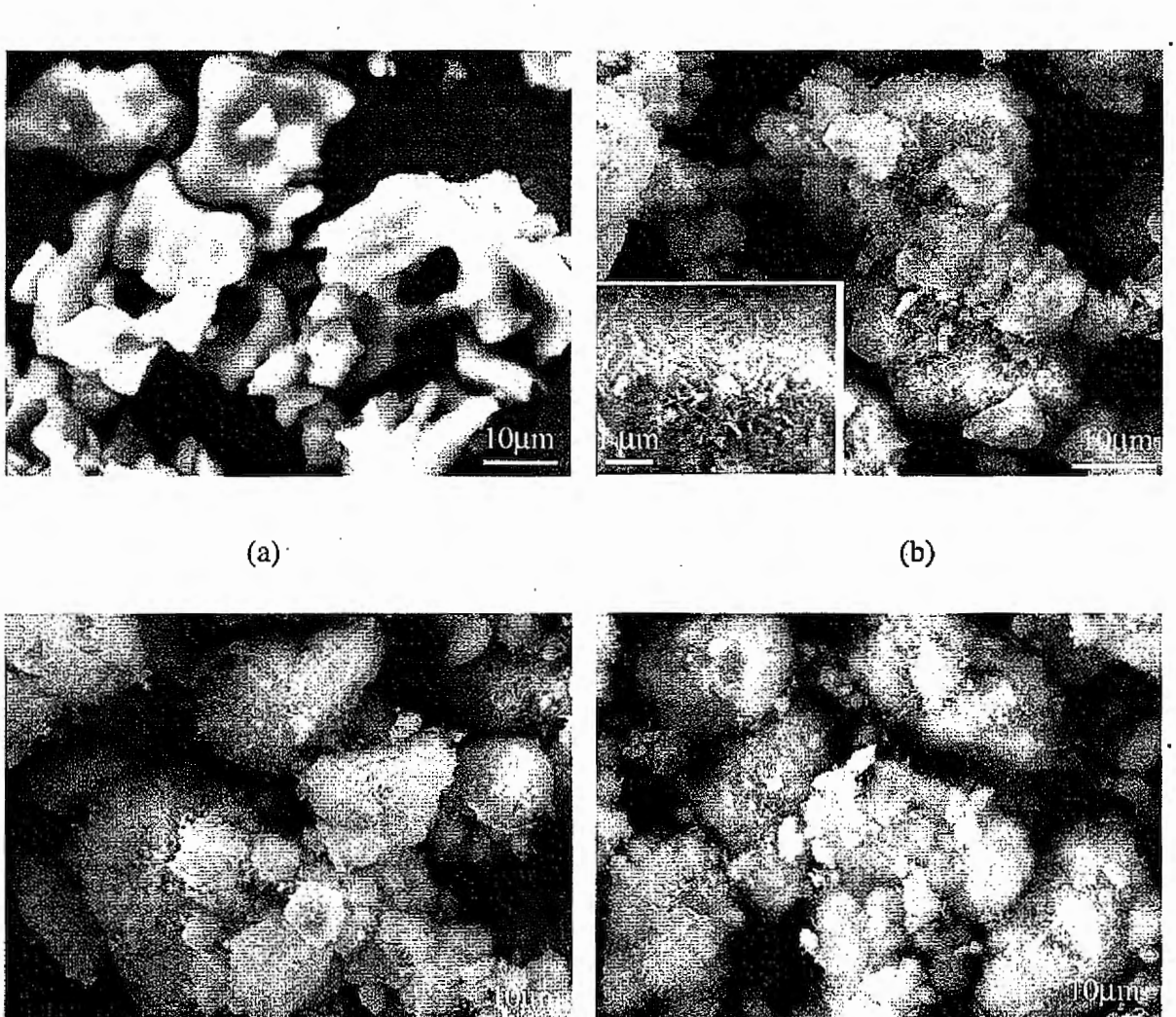

Figure 5 SEM micrographs of α-TCP hydrolysis products dried in vacuum system. (a) synthesized α-TCP, (b) in SBF 1 week, (c) in SBF 2 weeks, (d) in SBF 4 weeks

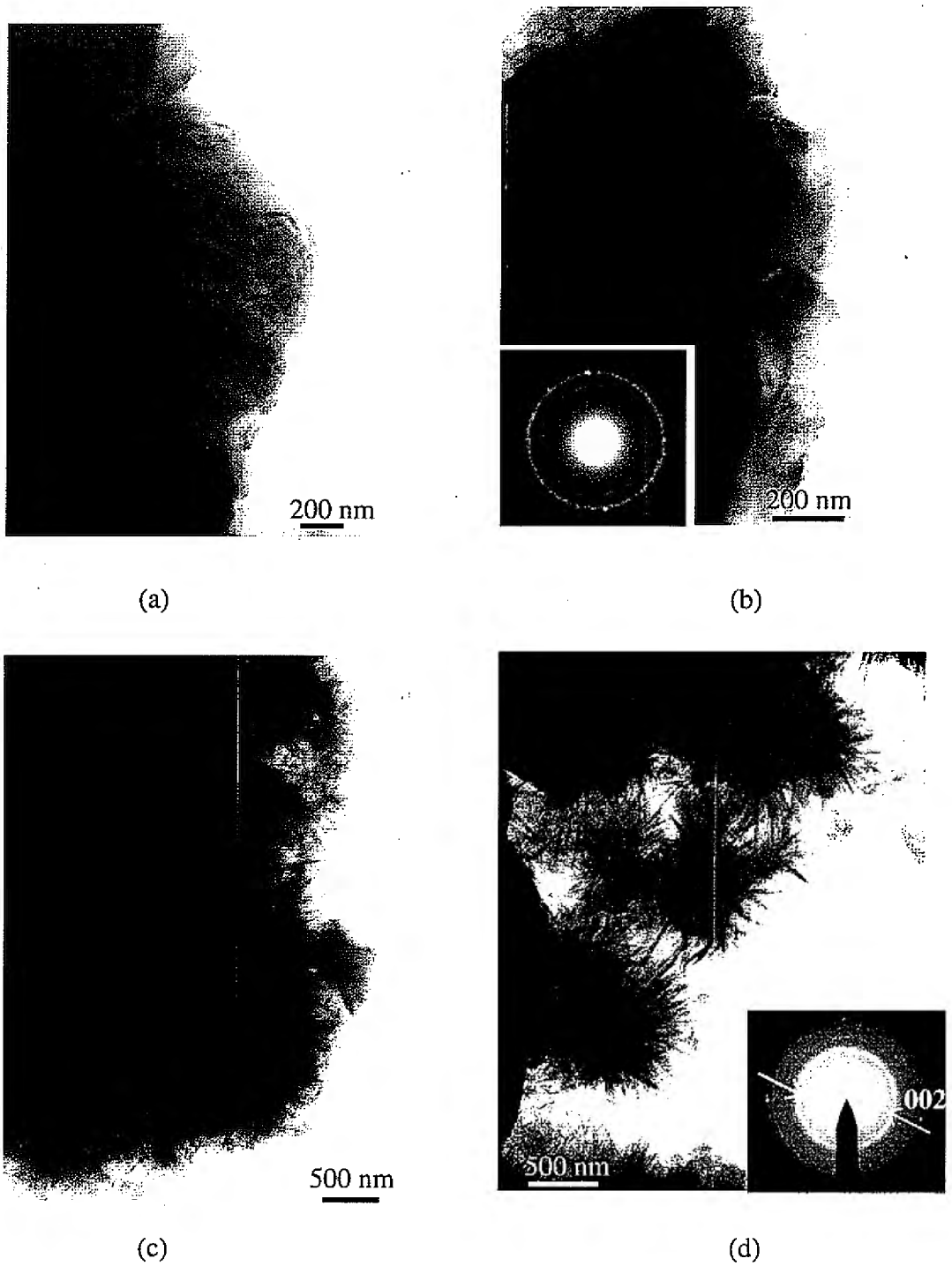

Figure 6 TEM micrographs of α-TCP hydrolysis products. (a) synthesized α-TCP; (b) in SBF 1 day inserted with SAD pattern from surface; (c) in SBF two weeks; (c) in SBF four weeks inserted with SAD pattern from needle-like crystals

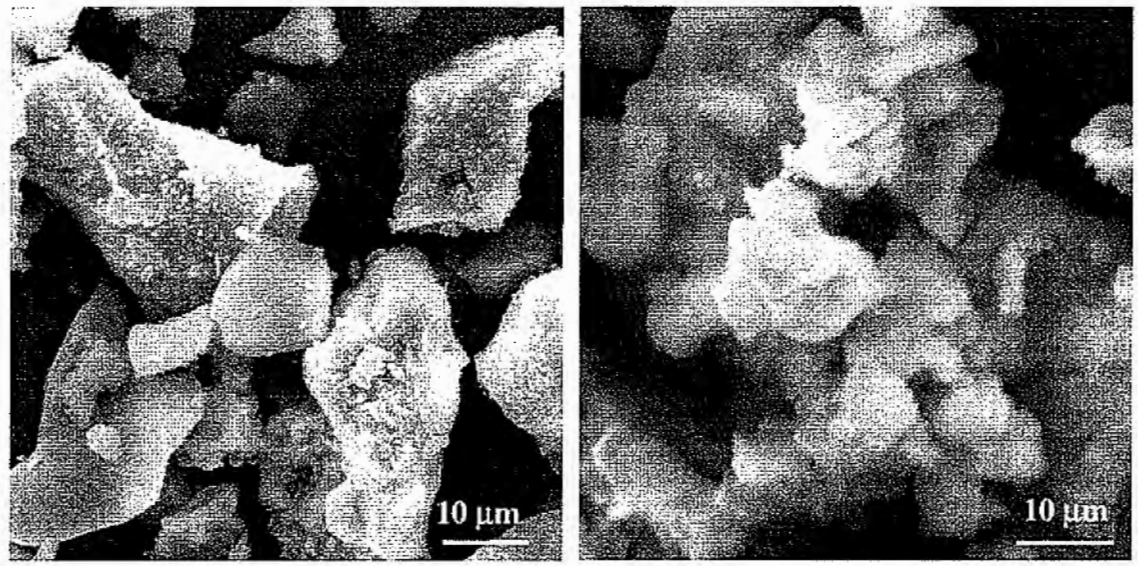

(a) (b)

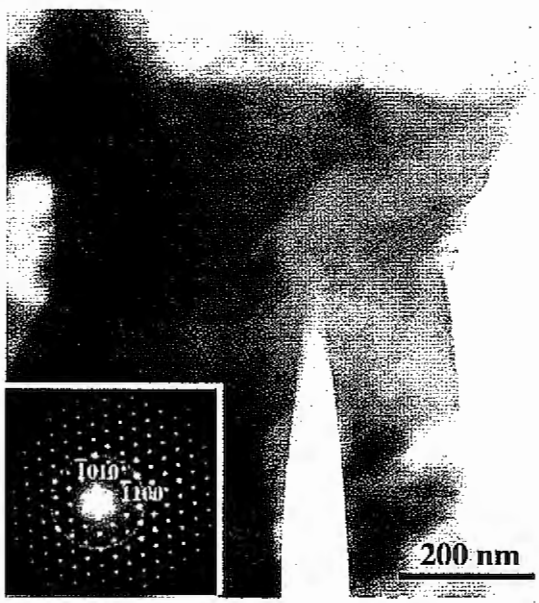

(c)

Figure 7 SEM and TEM micrographs of α-TCP hydrolysis products dried in the oven. (a) in SBF 1 week, (b) in SBF 4 weeks, (c) TEM micrograph of α-TCP aged in SBF two weeks. Inserted SAD pattern is along the [0001] direction.

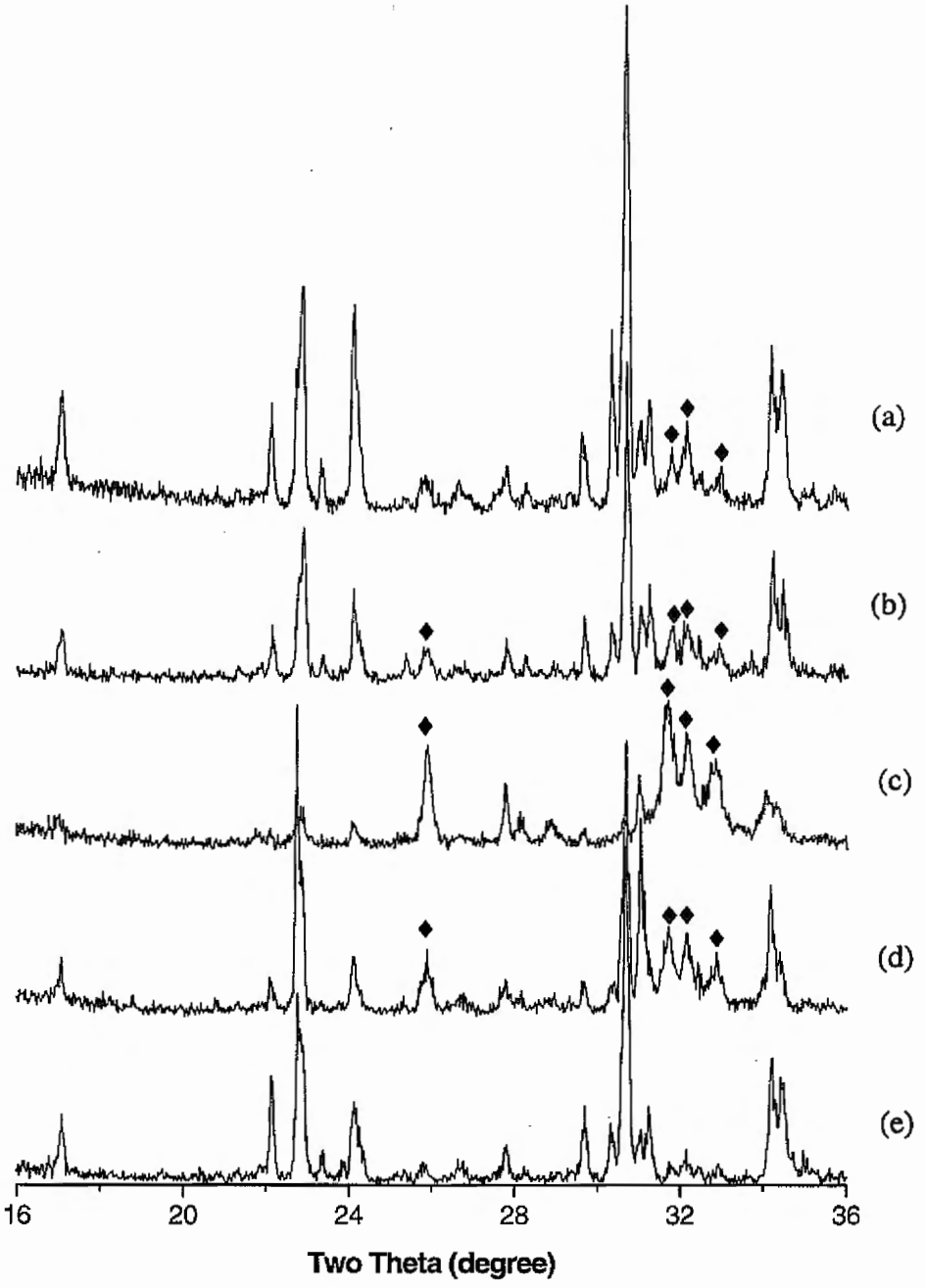

Figure 8 XRD patterns of α-TCP hydrolysis products dried in the oven. (a) synthesized α-TCP; (b) in SBF 1 week; (c) in SBF 2 weeks; (d) in SBF 3 weeks; (e) in SBF 4 weeks. ◆ HAp phase

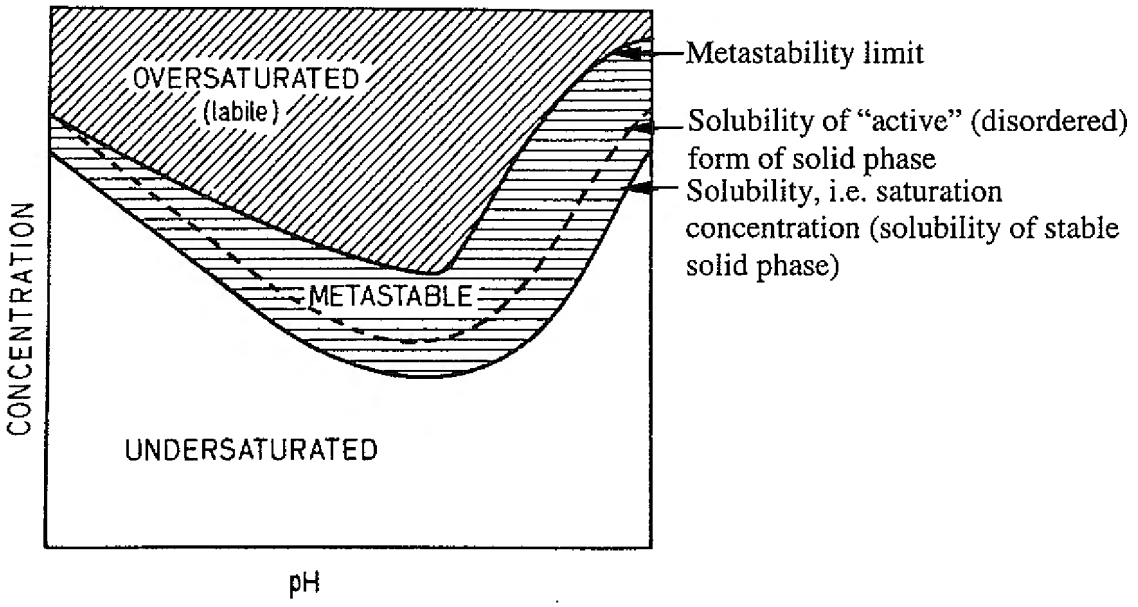

Figure 9 Solubility and saturation. A schematic solubility diagram showing concentration ranges versus pH for supersaturated, metastable, saturated, and undersaturated solution [20].

CHAPTER 7: GENERAL CONCLUSION

An ideal temporal bone implant material should: (1) mimic the bone in composition, size and shape; (2) have controlled resorption rate to match the new bone growth rate and maintain the necessary mechanical strength; (3) support and improve the activity of osteoblasts in the development of new bone. Within the scope of these constraints, silicon and zinc modified tricalcium phosphate (Si,Zn-TCP) was synthesized as a candidate for resorbable temporal bone implant. This research focuses on the effect of Si and Zn on the dissolution behavior, i.e. solution-drived resorption, of tricalcium phosphate. The phase composition and crystal structure were studied to understand the stability mechanism.

Si,Zn-TCP powders with different doping levels were prepared by high temperature sintering of reactants with designed composition. Depending on the level of Si and Zn addition, the synthetic products exhibit α-phase, β-phase, or mixture of the two phases. Zn addition effectively suppressed the phase transition from β- to α-TCP, while Si impels this phase transformation. When doped both Si and Zn at the same level, Zn effect dominates the phase composition. Analysis of XRD patterns revealed that α:β ratio decreases from about 9:1 to 2:3 as the concentration of additives increased from 1% to 5%. With the maximum 10% addition, there is only β phase observed in the XRD pattern.

For samples with 10% Si and Zn addition, analysis of neutron powder diffraction data shows that Zn^{2+} (R=0.74 Å) ions substitutes for Ca^{2+} (R=0.99 Å) at Ca(4) and Ca(5) sites, and Si^{4+} (R=0.26 Å) substitutes for the P^{5+} (R=0.17 Å) at P(1) site in β-TCP. Si,Zn-10 was confirmed to have the a rhombohedral structure (space group R3c, Z = 21), with the unit cell parameters $a = b$ =10.3958(1) Å, c = 37.3122(7) Å, $\alpha = \beta = 90°$, and $\gamma = 120°$ in the hexagonal setting. The unit cell volume decreases 35.7 $Å^3$ compared to pure β-TCP. The site Ca(4) was partially substituted by Zn and the Ca,Zn(4)···O(9) bond distance reduced 2.808(5) Å, much shorter than the original 3.041(1) Å in pure β-TCP structure. Ca(5) site was totally substituted by Zn and Zn(5)···O bond distance decreases about 0.1 Å compared to Ca(5)…O distance as the result of the smaller Zn^{2+} substitution. The new bond distances are close to the theoretical calculated one per the ionic radii, suggesting the elimination of the distortion and stabilization of the crystal structure. The total Zn substitution amount is 10.01% of total

Ca sites. However, neutron diffraction data indicates that Si only partially substitutes P(1) sites. The bond length of P,Si(1)···O(10) is 0.089 Å larger than P(1)···O(10) distance, showing the larger Si substitution effect along *c* axis. The increased P(2)···O distances are because Zn substitution reduces Ca,Zn(4)···O and Zn(5)···O distances. Si substitution induces a slight distortion of β- phase structure even though the effect is not remarkable. Hence, the substitution amount is only 3.86% of total P sites. The other 6.14% Si exists as amorphous nano-clusters of Si-rich phase.

With variant doping level, Si,Zn-TCP samples showed competitive effect of Si and Zn substitution. The substitution of Zn for Ca will lead to a contraction, while the substitution of Si for P will cause expansion of the structure. Zinc content has the dominant effect on the β phase, and silicon has a dominant effect on the α phase. As the level of doping increases, Zn dominates the structural changes brought about by the additives. These data are also consistent with the phase stability study.

The dissolution behavior of TCP could be modified by doping Si and Zn as these additives to stabilize the crystal structure, form the low solubility phases and chang the surface properties. In terms of the dissolution of calcium, the dissolution rate order is:

Si,Zn-10 < Zn-5 < β-TCP < Si,Zn-5 < Si,Zn-3 < α-/β-TCP < Si-5 < α-TCP

This order shows that both Si and Zn can inhibit TCP dissolution. As discussed in crystal structure study, Zn addition can decrease the distortion and stabilize less solubleβ-phase structure rather than the α-phase. Zn also behaves as sintering aid to produce dense and larger particles with lower surface area. According to Yin and Stott's *ab initio* density functional calculations [1], SiO_4^{4-} may substitute for a pair of PO_4^{3-} groups with an excess Ca^{2+} for charge compensation in α-TCP structure. Since there is a calcium vacancy in the anion–cation columns, this substitution is highly probable to stabilize the α-TCP structure.

When samples are aged in SBF, dissolution of TCP is not the only reaction in the solution. When the initial TCP dissolution leads to a supersaturated solution with respect to HAp, reprecipitation of HAp on TCP surface occurs since HAp is the most stable phase at pH>4.2. Amorphous apatite, the precursor of HAp is the first phase to nucleate on the TCP surface, appeared as spherical particles with about 20 nm in diameter. These spherical

particles aggregate together and finally grow to needle-shape hydroxyapatite crystal. The final precipitated phase is calcium-deficient carbonate-containing hydroxyapatite as evidenced by chemical analysis and FTIR spectra, along with Cl^-, Na^+, and Mg^{2+} impurities incorporated into the structure. It has similar composition to the bone mineral. The order of precipitation rate is:

Si,Zn-10 < Zn-5 < Si,Zn-5 < Si,Zn-3 < β-TCP < Si-5 < α-/β-TCP < α-TCP

Similar to the effect on dissolution, Zn appears to inhibit HAp precipitation too. On the contrary, Si can promote HAp reprecipitation by forming the highly porous structure. The quick formation of HAp on surface decreases the available TCP surface for dissolution, result in depression of TCP dissolution rate. With both Zn and Si addition, Zn has the dominating effect on the Si,Zn-TCP dissolution behavior.

The cytotoxicity test shows that Si and Zn addition has no cytotoxic behavior on the cell within the additive level employed in this study. The health cells were tightly bounded to the particle surface, suggesting the good biocompatibility of Si,Zn-TCP. In order to confirm Si and Zn effect on new bone growth, Si,Zn-TCP is recommended to be investigated in future by estimating the osteoconductivity in animal experiments (in vivo) and the expression of mRNA in type I collagen, phosphatase activity and osteocalcine in cell culture.

Reference:

1. Yin X, Stott MJ. Theoretical insights into bone grafting silicon-stabilized α-tricalcium phosphate. Journal of Chemical Physics 2005;122(2):024709.

ACKNOWLEDGEMENTS

This work was performed at Ames Laboratory under Contract No. W-7405-Eng-82 with the U.S. Department of Energy. The United States government has assigned the DOE Report number IS-T 2311 to this thesis.

Special thanks to my husband Zhe, my mom and my sister for their support and encouragement. It is sad that I cannot thank my father in person for his support. I hope he could share my achievement and enjoyment in the heaven. I love my family dearly.

I would also like to thank Dr. Andrew Thom and my other group members for their assistance throughout this work. I would like to thank Professor Vitalij Pecharsky for discussions on Rietveld refinement. I would like to thank Dr. James W. Richardson and Dr. Evan Maxey for neutron diffraction experiment and data analysis.

This work could not be completed without the instruction and criticisms from my major professor Dr. Mufit Akinc. His contribution to this work is greatly appreciated.

Finally, I would like to thank my graduate committee, Dr. Mufit Akinc, Dr. Matthew Kramer, Dr. Thomas D. McGee, Dr. Surya K. Mallapragada and Dr. Michael G. Conzemius.

APPENDIX A:
RESORPTION RATE TUNABLE BIOCERAMIC: SI&ZN-MODIFIED TRICACIUM PHOSPHATE

A Paper published in the Ceramic Engineering and Science Proceedings (the 29th International Conference on Advanced Ceramics and Composites - Advances in Bioceramics and Biocomposites) [1]

Xiang Wei[a] and Mufit Akinc[b]

Department of Materials Science and Engineering, Iowa State University, Ames, IA 50011, U.S.A

[a]xiangwei@iastate.edu, [b]makinc@iastate.edu

Abstract

An ideal bone implant material would support the activity of osteoblasts in the development of new bone, while simultaneously being resorbed by osteoclasts as part of the lifelong orderly process of bone remodeling. Silicon and Zinc modified tricalcium phosphate, a biphasic material, was synthesized as a candidate for resorbable temporal bone implant having a controlled solubility and pharmaceutical effect to promote bone formation. From XRD and ICP analyses, it was shown that up to 10mol% Si and Zn can be incorporated in tricalcium phosphate (TCP) without formation of a secondary phase. Changes in lattice parameters and unit volume of TCP as calculated by Rietveld analysis indicate that Si and Zn substitute for P and Ca respectively. The dissolution study was carried out in simulated body fluid. The chemical analysis and XRD results imply that the Si and Zn additives not only decrease the solubility of TCP, but also slow hydroxyapatite (HAp) precipitation, indicating that dissolution of temporary implant and formation of new bone may be tailored by the level of Si and Zn substitution.

I. Introduction

Among the calcium phosphate ceramics, tricalcium phosphate has been investigated most extensively as the primary resorbable bioceramics for bone replacements[1-3]. According to the CaO/P_2O_5 phase diagram, tricalcium phosphate (TCP) exists in three crystalline forms: the β-tricalcium phosphate (β-$Ca_3(PO_4)_2$, β-TCP) is stable below 1125°C, at which temperature it transforms to α-tricalcium phosphate (α-$Ca_3(PO_4)_2$, α-TCP), and α' (α'-TCP) is stable above 1430°C[4]. Dissolution rate of β-TCP was reported to be 3-12 times faster than stoichiometric hydroxyapatite ($Ca_5(OH)(PO_4)_3$, HAp)[5]. In vitro studies revealed that the α-TCP had a higher dissolution rate than β-TCP[3]. Ducheyne et al. compared the dissolution rates of six calcium phosphates in calcium and phosphate free solution at pH 7.3. The dissolution rate increased from HAp to tetra calcium phosphate (TTCP) in the following order[6]:

$$HAp < CDAp < \beta\text{-}TCP < \alpha\text{-}TCP < TTCP$$

Due to its higher solubility, TCP as an implant, is expected to degrade in the host and be gradually replaced by the regenerating bone. Based on different tissue and implant conditions, the biodegradability of TCP ceramics are vary widely[7, 8]. TCP was reported to be more bioresorbable than HAp that usually show minimal resorption. TCP behaves as a seed of bone and a supplier of the Ca and PO_4 ions. Furthermore, α-TCP can be handled as a paste and set in situ. However, higher solubility of TCP as bone implant results in loss of strength. Thus, the suitability of TCP for use in vivo is critically dependent on how the dissolution rate might be controlled by chemical modification. The biphasic α and β-TCP with controlled dissolution behavior will be a promising resorbable biomaterial for temporary implant.

It has been shown that the solubility of zinc or magnesium doped β-TCP decreases with Zn and Mg content[9, 10]. The decrease in solubility was attributed to the increased stability of the β-TCP structure caused by the addition of Zn or Mg ions. Langstaff et al found that Si-doped HAp formed modified HAp and α-TCP phases following sintering[11, 12]. This material was stabilized in biological media and could be resorbed when acted upon by osteoclasts[11-13]. In their studies, β-TCP, HAp and commercial HAp showed ~0.02% calcium

dissolution per day, whereas α-TCP and Si-HAp was ~0.03% and ~0.006% respectively. No report was found on the effect of these additives on α and β-TCP biphasic materials.

From a pharmaceutical point of view, Zn and Si are osteoconductive and could stimulate osteogenesis for bone growth. Zinc polycarboxylate cements have also been used in dentistry for many years[14]. Since zinc oxide (ZnO) was able to form salt-bridges between Zn and carboxylate ions, a simply blended mixture of ZnO/HAp was used to form the bone cement with polyacrylic acid aqueous solution. The effect of a silicon deficient diet on chicks indicated that silicon is an essential trace element for the normal growth and development of chicks[15]. An increase in dietary silicon has been directly linked to an increase in bone mineralization. Electron microprobe analysis and imaging ion microscopy showed that silicon is localized in sites of active bone formation in young rats and mice[16].

II. Materials and Method

Si,Zn-modified TCP and pure α-TCP was prepared by sintering $CaCO_3$, $NH_4H_2PO_4$, ZnO and fumed SiO_2 at certain mole ratio at 1300°C and quenching in dry air. The β-TCP was produced by sintering at 1000°C. More preparation details were described in another paper[17].

Chemical composition of the powders was determined by the ICP (Thermo Elemental, Franklin, MA). An X-ray powder diffractometer (Scintag Inc. CA) with Cu Kα radiation was used for crystal structure analysis and lattice parameter determinations. The Rietveld analysis of the diffraction patterns with different additive levels was performed by Rietica software. Initial crystal parameters for α and β-TCP were taken from the literature[18, 19].

Four different samples were investigated for dissolution behavior in synthetic body fluid: synthesized α-TCP, β-TCP, Si,Zn-TCP-5 and Si,Zn-TCP-10 (the number 10 refers to 10 mol% of P and Ca are replaced by Si and Zn respectively). The glass bottles were sealed and kept in a water bath shaker in order to preserve the temperature at 37°C. The pH of the solution was measured with an accuracy of ±0.02. Suspensions were centrifuged and Ca concentration of clear solution was measured by atomic absorption spectroscopy (Perkin-Elmer 5000). The standard solutions for AAS were prepared based on the same ion

concentration of SBF except Ca^{2+}. The solid was washed several times by de-ionized water and dried in vacuum for XRD and SEM.

III. Results

1. Composition and Structure

Table 1 lists the nominal and measured calcium, phosphorus, zinc and silicon contents for synthesized α-TCP and Si,Zn-TCP powders as determined by ICP. The accuracy of analysis was 3% with a reproducibility of 5%. The measured values are very close to the intended compositions indicating negligible composition change during synthesis. The ratio of (Zn+Ca):(Si+P) is round 1.5, same as the ration of stoichiometric TCP.

Table 1 Chemical analysis of the synthesized TCP samples

Samples	Si [wt%]		Zn [wt%]		Ca:P*	(Zn+Ca):(Si+P)*
	Nominal	Measured	Expected	Measured	Measured	Measured
α-TCP	0	0.008	0	0.099	1.53	N/A
Si,Zn-2+	0.36	0.35	1.25	1.27	1.487	1.457
Si,Zn-10	1.77	1.97	6.15	6.03	1.477	1.433

+Si,Zn-2: TCP modified by the addition of 2 mol% each of Si and Zn.
*Expressed as mole ratio

X-ray diffraction patterns of sintered Si,Zn-TCP show excellent agreement with the published JCPDS files for α-TCP (#29-395), β-TCP(#09-169), or mixture of the two depending on additives content (Fig. 1). No evidence for other crystalline phases, such as $CaSiO_3$ or other phosphates, was observed indicating that Zn and Si are dissolved completely in the TCP structure. Figure 1 also compares XRD patterns of Si,Zn-5, Si-5, and Zn-5 samples. Si,Zn-5 shows a mixture of α and β phases, while Zn-5 has only the β phase and Si-5 has α as the major phase implying that Zn addition favors formation of β phase, and will increase the phase transformation temperature ($T_{\beta\rightarrow\alpha}$); while Si addition favors α structure, which will decrease $T_{\beta\rightarrow\alpha}$. The phase distribution analysis calculated by the Rietveld refinement method show that α:β ratio decreases from about 9:1 to 2:3 as the concentration of additives increased from 1 to 5 mol%, indicating that Zn addition dominates the phase composition. In the phase diagrams of $Ca_3(PO_4)_2$-Ca_2SiO_4, the solubility limit of Si in TCP is

approximately at a molar ratio of 4 mol% expressed as $Si/(Si+P)$ [20]. In the Si-5 sample, silicocarnotite appears as the second phase. Si,Zn-TCP samples show that up to 10 mol% Si and Zn can be incorporated into the TCP lattice without formation of a second phase.

XRD patterns of Si,Zn-TCP show slight shift, indicating a change in the lattice parameters imposed by the additives. Based on ionic radii, the substitution of Zn for Ca will lead to a contraction, while the substitution of Si for P will cause expansion of the unit cell[21]. The lattice parameters and unit cell volumes (V_{uc}) are shown in Figure 2. The effect of Zn addition on the structure is demonstrated as parameters *a, c* and V_{uc} of Zn-TCP were all smaller than those of pure TCP. $V_{uc}(\alpha)$ of Zn-5 is 10 $Å^3$ smaller than α-TCP (4307.5 $Å^3$ vs 4317.6 $Å^3$). $V_{uc}(\beta)$ of Zn-5 and Zn-10 are 45 and 314 $Å^3$ smaller than that of β-TCP. $V_{uc}(\alpha)$ of Si-5 is 34$Å^3$ larger than that of α-TCP as expected from Si substitution. Compared to α-TCP, the lattice parameters of Si-TCP and Si,Zn-TCP expand both in *b* and *c* directions implying that Si substitutes primarily in sites promoting expansion along these directions. Si,Zn-TCP samples showed competitive effect of Si and Zn: $V_{uc}(\alpha)$ of Si,Zn-TCP samples are larger than that of the pure α-TCP, but decrease at higher doping level. $V_{uc}(\beta)$ of Si,Zn-TCP is smaller than pure β-TCP but larger than Zn-TCP. Hence zinc ion has the dominant effect on the β phase, and silicon has a dominant effect on the α phase. At higher doping levels, Zn dominates the structural changes brought by the additives.

2. Dissolution Behavior

Variation of $[Ca^{2+}]$ as a function of time in SBF in contact with TCP powders is given in Figure 3. For α-TCP, $[Ca^{2+}]$ shows an increase in the first couple of days then decreased at longer time with slightly increasing of pH. This behavior may be explained by an initial dissolution of Ca^{2+} followed by reprecipitated in the form of HAp (HAp is the least soluble of the phosphates). The β-TCP shows similar dissolution behavior as α-TCP, but the lower Ca^{2+} concentration indicates the lower solubility than α-TCP. In contrast, Ca^{2+} concentration of SBF containing Si,Zn-TCP-10 didn't change much with constant pH, indicating that the additives inhibited not only the dissolution of TCP, but also the precipitation of HAp. For

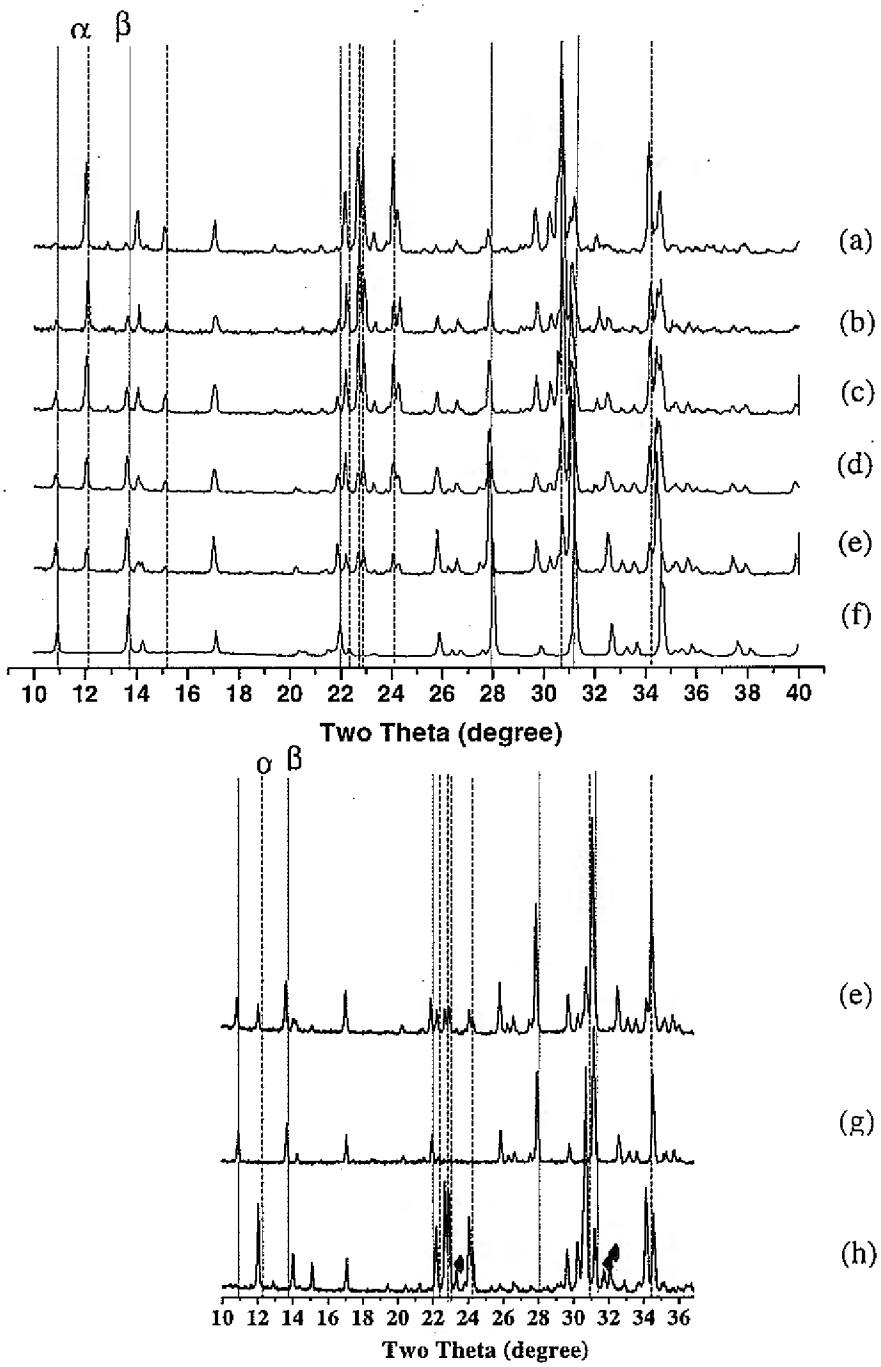

Fig. 1 XRD patterns of synthesized Si,Zn-TCP with different doping level. (a)Si,Zn-1 (b)Si,Zn-2 (c) Si,Zn-3 (d)Si,Zn-4 (e)Si,Zn-5 (f)Si,Zn-10 (g)Zn-5 (h)Si-5. The dot lines represent the distinct peaks of α-TCP, and the dash lines are β-TCP. ♦ is silicocarnotite phase.

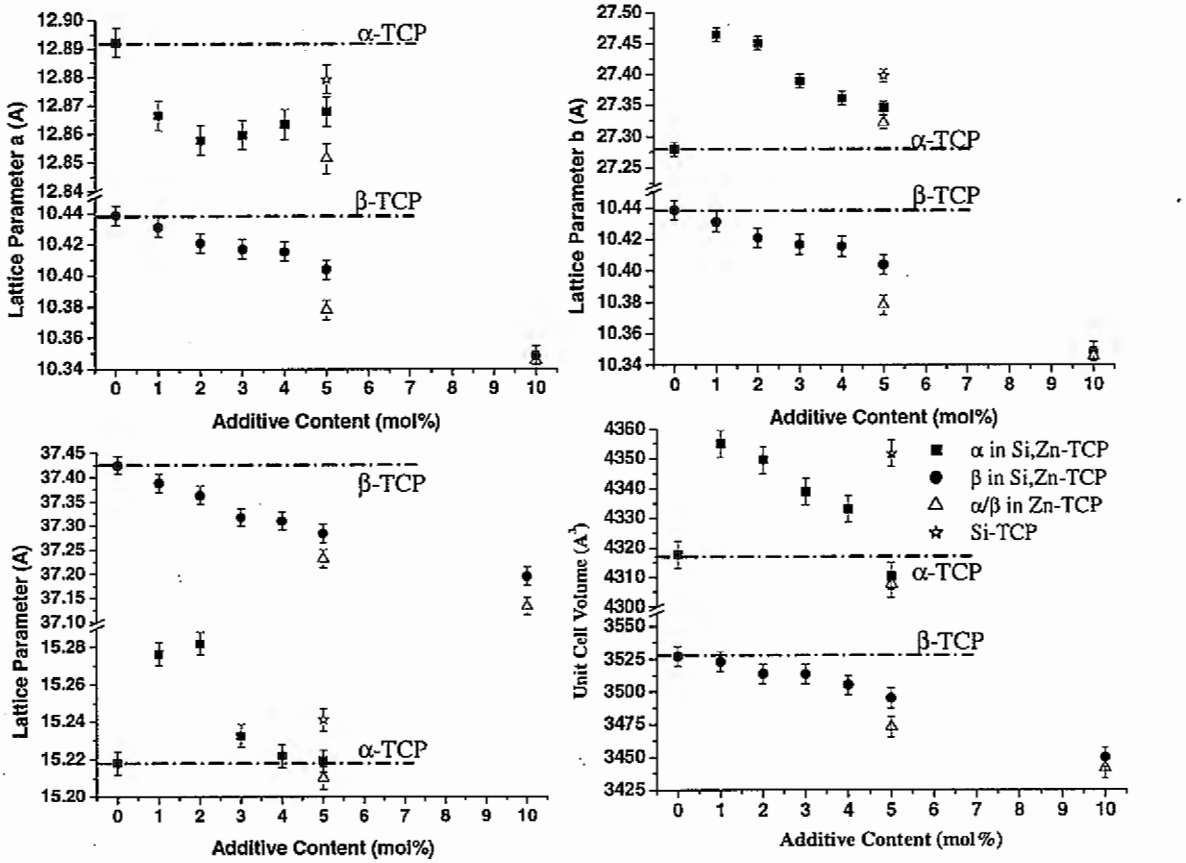

Fig. 2 Lattice parameters and unit cell volume of Si,Zn-TCP determined by Lebail refinement. The error bars are based on standard deviation of triplicate measurements.

Si,Zn-TCP-5, Ca^{2+} concentration increases slightly for the first several days then decreases, $[Ca^{2+}]$ is between TCP and Si,Zn-TCP-10. The decrease in solubility can be attributed to the increased stability of the TCP structure as a result of the addition of Zn and Si. XRD patterns of the samples after aging in SBF show that the solid phase of α-TCP sample was almost entirely converted to HAp, while no HAp phase was observed in Si,Zn-TCP samples (Fig. 4).

After immersion in SBF, the surface morphology of Si,Zn-TCP was significantly different from the α-TCP (Fig. 5). The surface of α-TCP after 4 weeks exposure to SBF shows characteristic solution-precipitated needle-like morphology of HAp. TEM micrograph shows thin fiber like features, radiating from the center out. The specific surface area of α-TCP increased from 0.47 to 51.47 m^2/g in 4 weeks due to the needle-like crystal morphology and smaller particle size. The XRD patterns and SEM micrographs of β-TCP also indicated the formation of small amount of HAp after soaking in SBF. However, there is no obvious morphology change in Si,Zn-TCP samples, which also prove that Si and Zn inhibited not only the dissolution but also the precipitation of HAp.

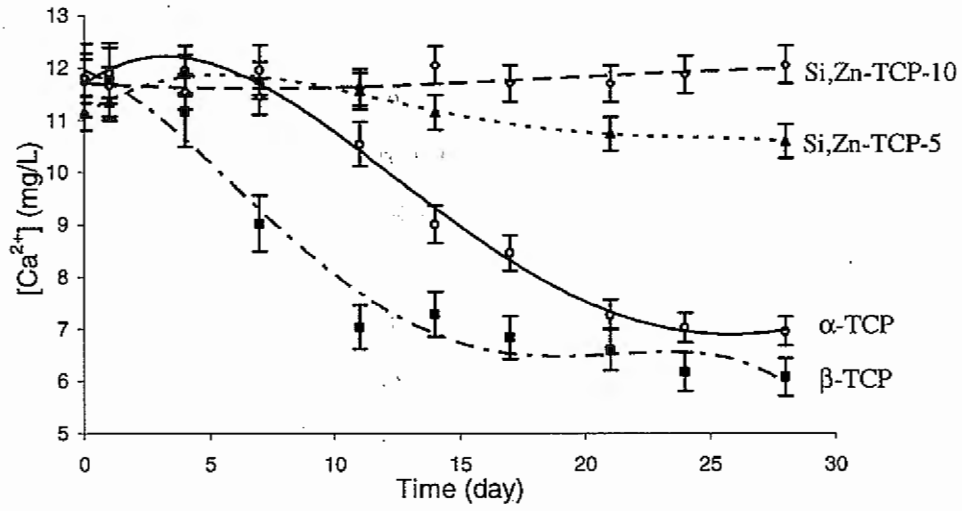

Fig. 3 Ca^{2+} concentration in SBF as a function of time

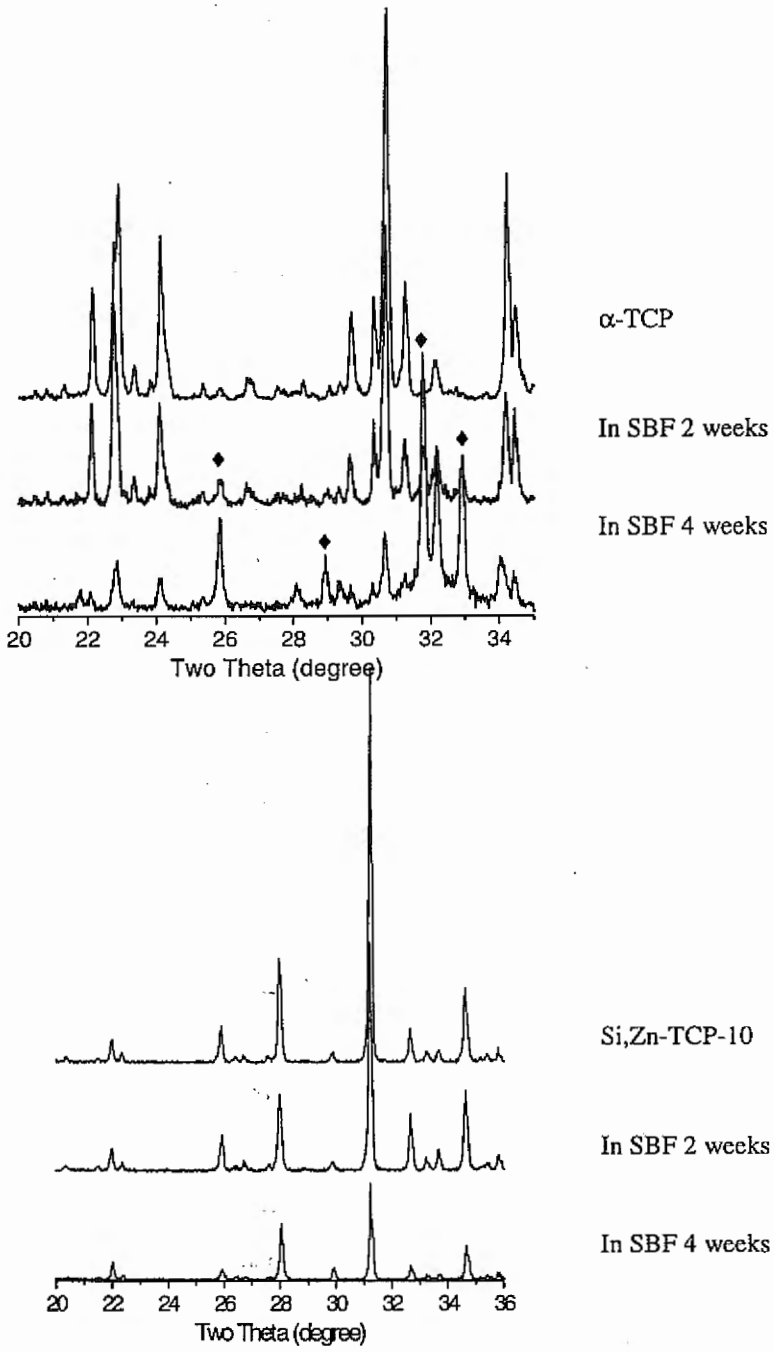

Fig. 4 XRD patterns of α-TCP and Si,Zn-TCP in SBF at different soaking time. ♦is HAp phase.

IV. Discussion

From the crystallographic point of view, the basic crystal structure of TCP can supply a suitable environment for Zn and Si substitution. In the β-TCP unit cell, Ca(4) and Ca(5) sites are unique compared to other three sites. Ca(4) is on the 3-fold axis and has an unusual coordination to the O(9), O(9'), O(9'') face of the $P(1)O_4$ group. Electrostatic repulsion between the cation and the phosphorus atom is expected to be significant and the Ca(4)···O(9) bonds are longer (3.041(1) Å) than normal Ca···O bond, which is about 2.4Å in agreement with the Pauling's rule[19, 22]. The Ca(5) site have six-fold octahedral coordination surrounded by oxygens, and all six Ca···O distances are relatively short, falling into the range 2.238-2.287Å. Therefore, these two sites are very suitable for the smaller cation, but are highly constrained for a Ca^{2+} ion. Substitution of smaller Zn^{2+} for Ca^{2+} results in more stable β-TCP structure than the undoped one by reducing the strain in the structure. In whitlockite, Mg^{2+} ions with ionic radius 0.57Å substituted Ca(4) and Ca(5) positions. The Mg(4)···O(9) bonds were 2.907Å, shorter than that of Ca(4)···O(9) bonds. The approach of O···Mg(5)···O angles toward 90° with increasing Mg content provides further confirmation of the trend toward a more ideal octahedral configuration[22]. Similarly, tetrahedral PO_4^{3-} ions in the TCP structure may be replaced by SiO_4^{4-} units, resulting in Si substituted TCP. According to the structure, each formula unit occupies 180 $Å^3$ in α-TCP compared with 168 $Å^3$ in the β form[23]. Since α-TCP has a more open structure than β-TCP, the larger Si^{4+} ions favor α over β structure.

The charge compensation due to Si^{4+} substitution for P^{5+} may be explained either by oxygen vacancies, or additional proton (H^+) incorporation into the structure. In contrast to expanded lattice parameter b and c, the contracted lattice parameter a of Si,Zn-TCP may result from the oxygen vacancies in this direction. A more detailed crystal structural analysis of Si-Zn-TCP is necessary to elucidate the mechanism of charge compensation.

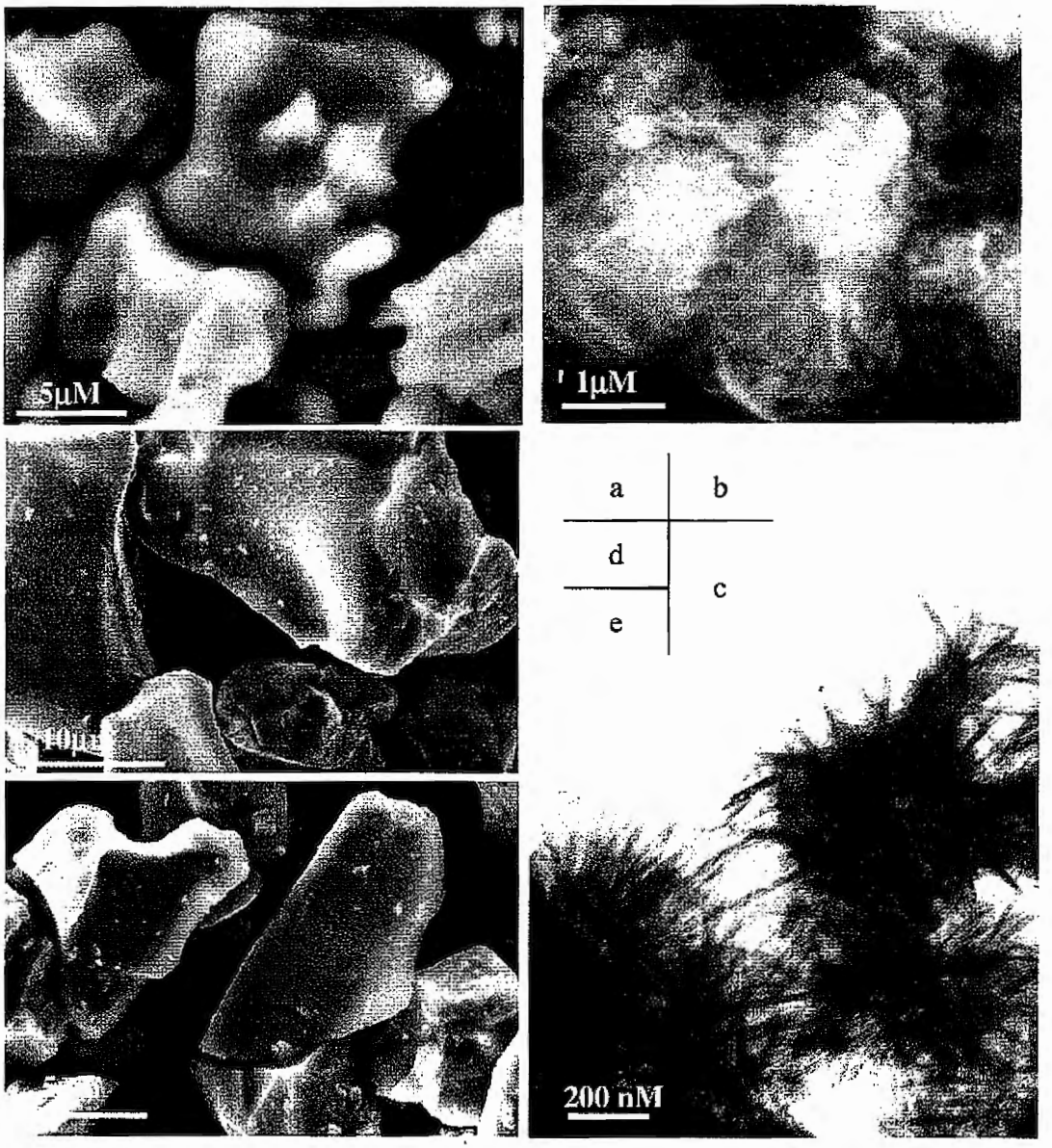

Fig. 5 Micrographs of α-TCP and Si,Zn-TCP in SBF. (a)synthesized α-TCP, (b)α-TCP in SBF after 4 weeks, (c) TEM micrograph of α-TCP in SBF 4 weeks (d)synthesized Si,Zn-TCP-10, (e) Si-Zn-TCP-10 in SBF after 4 weeks.

V. Conclusion

Si,Zn-modified TCP exhibits α-, β-TCP structure, or mixture of the two depending on the level of the additives. The changes in lattice parameters and unit cell volume clearly demonstrate that Si and Zn are structurally incorporated into TCP and stabilize the structure. Zn can substitute for the Ca and causes a contraction of the unit cell. Si can substitute for the P and results in expansion of the unit cell. 10 mol% addition of Si & Zn appears to prevent dissolution of TCP, and inhibit precipitation of HAp. By varying the Zn & Si additions, the dissolution behavior of TCP may be controlled.

Reference:

1. RZ L, JP L, G D, R. K. Encyclopedic Handbook of Biomaterials and Bioengineering. New York: Marcel Dekker, 1995.

2. Klein CPAT, Driessen AA, de Groot K. Relationship between the degradation behaviour of calcium phosphate ceramics and their physical-chemical characteristics and ultrastructural geometry. Biomaterials 1984;5(3):157-160.

3. Park JB, Lakes RS. Biomaterials: An Introduction 2nd ed. New York: Plenum Publishing, 1992.

4. Kreidler E, Hummel F. Phase relationships in the system SrO- P2O5 and the influence of water vapor on the formation of Sr4P2O9. Inorg Chem 1967;6:884-891.

5. Jarcho M. Calcium phosphate ceramics as hard tissue prosthetics. Clinical Orthopaedics and Related Research 1981;157:259-278.

6. Ducheyne P, Radin S. London: Butterworth-Heinemann, 1991.

7. Klein C, Driessen AA, de Groot K, A. VDH. Biodegradation behavior of various calcium phosphate materials in bone tissue. J Biomed Mater Res 1983;17:769-784.

8. Driessens F. Formation and stability of calcium phosphate in relation to the phase composition of the mineral in calcified tissues. Boca Raton: CRC Press, 1983.

9. Manjubala I. preparation of biphasic calcium phosphate doped with magnesium fluoride for osteoporotic applications. J Mater Sci letter 2001;20:1225-1227.

10. Ito A. Resorbability and solubility of zinc-containing tricalcium phosphate. J Biomed Mater Res 2002;60:224-231.

11. Langstaff S, Sayer M. Resorble bioceramics based on stailized calcium phosphates. Part I: rational design, sample preparation and materials characterization. Biomaterials 1999;20:1727-1741.

12. Langstaff S, Sayer M. Resorble bioceramics based on stabilized calcium phosphates. Part II: evaluation of biological response. Biomaterials 2001;22:135-150.

13. Gibson IR, Best SM, Bonfield W. Chemical characterization of silicon-substituted hydroxyapatite. J biomed Mater Res 1999;44:422-428.

14. Xie D, Feng D, Chung I-D, Eberhardt AW. A hybrid Zinc-calcium-silicate polyalkenoate bone cement. Biomaterials 2003;24:2794-2757.

15. Carlisle EM. Silicon: a requirement in bone formation independent of vitamin D. Calcif Tissue Int 1981;33(1):27-34.

16. Landis WJ, Lee DD, Brenna. JT, Chandra S, Morrison GH. Detection and localization of silicon and associated elements in vertebrate bone tissue by imaging ion microscopy. Calcif Tissue Int 1986;38(1):52-59.

17. Wei X, Akinc M. Si,Zn-modified tricalcium phosphates: A phase composition and crystal structure study. Key Engineering Materials 2005;284-286:83-86.

18. Mathew M, Schroeder L, Dickens B, Brown W. The crystal structure of α-Ca3(PO4)2. Acta Cryst 1977;B33:1325-1333.

19. Dickens B, Schroeder LW, Brown WE. Crystallographic Studies of the Role of Mg as a Stabilizing Impurity in β-tricalcium phosphate: I. The Crystal Structure of Pure β-tricalcium phosphate. J Solid state Chemistry 1974;10:232-248.

20. Nurse RW, Welch JH, Gutt W. High-temperature phase equilibria in the system dicalcium silicate-tricalcium phosphate. Journal of the chemical society 1959:1077-1083.

21. Lide DR. CRC Handbook of Chemistry and Physics 84th edition. Boca Roton: CRC Press LLC, 2003.

22. Schroeder LW, Dickensand B, Brown. WE. Crystallographic Studies of the Role of Mg as a Stabilizing Impurity in β-tricalcium phosphate: II. Refinement of Mg-containing β-tricalcium phosphate. J Solid State Chemistry 1977;22:253-262.

23. Elliott JC. Structure and Chemistry of the Apatites and other Calcium Orthophosphates. London: Elsevier, 1994.